Understanding supermassive black hole accretion and jet formation through extremely high angular resolution VLBI observations

Author: Teresa Toscano Domingo

Supervised by Dr. José Luis Gómez Fernández

Programa de Doctorado Física y Ciencias del Espacio

Universidad de Granada

July 2025

Editor: Universidad de Granada. Tesis Doctorales
Autor: Teresa Toscano Domingo
ISBN: 978-84-1195-972-8
URI: https://hdl.handle.net/10481/110576

...To the world

Neil Gaiman and Terry Pratchet
(Good Omens)

I've seen things you people
wouldn't believe... All those
moments will be lost in time, like
tears in rain.
Time to die.

Blade Runner

Abstract

This thesis investigates the structure, dynamics, and magnetic field properties of relativistic jets in active galactic nuclei (AGN) through high-resolution Very Long Baseline Interferometry (VLBI) observations and advanced imaging methods. To this end, it combines three complementary studies that collectively address the challenges of reconstructing and interpreting these objects from different perspectives.

First, pushing the limits of current black hole imaging towards the recovery of the first movies of these objects, we contribute to the development of dynamic imaging methods for black holes by validating a regularized maximum likelihood (RML) framework. This algorithm, as part of a joint effort in one of the most ambitious projects within the Event Horizon Telescope Collaboration (EHTC), is focused on a multi-modality approach via a Multi-objective Particle Swarm Optimization (`MO-PSO`) algorithm. This approach efficiently enables the exploration of the multimodal posterior distribution, and recovers dynamic, full Stokes reconstructions of variable sources, such as Sagittarius A* (Sgr A*), the supermassive black hole at the centre of our galaxy. We use simulated synthetic data that present the same properties as EHTC data from SgrA* in April 11 2017. These data are used to create different synthetic models varying in morphology and increasing dynamic complexity. This way, the ability to robustly reconstruct these models is carefully validated following different metrics. Moreover, we show that while many solutions can fit the sparse VLBI data, only a subset are physically plausible.

Second, we present a multi-frequency polarization study of the quasar 3C 273, using Very Long Baseline Array (VLBA) observations at six different frequencies (5, 8, 15, 22, 43 and 86 GHz) to produce total intensity, linear polarization, and rotation measure (RM) maps. The results reveal a robust transverse RM gradient across the jet. This provides strong evidence for an ordered helical magnetic field structure, likely playing a key role in jet collimation. A comparison with earlier epochs shows temporal variations in the RM, suggesting a dynamic evolution in the jet sheath's magnetized plasma environment.

Second, we revisit the parsec-scale magnetic field structure of the quasar 3C 273 through a new polarization study using the VLBA at six frequencies (5, 8, 15, 22, 43, and 86 GHz). Our study produces detailed maps of total intensity, linear polarization, and RM. We confirm the presence of a robust transverse RM gradient across the jet, supporting the existence of a large-scale helical magnetic field, likely playing a key role in jet collimation. By comparing with earlier epochs, we detect temporal variations in both the RM magnitude and gradient structure, indicating dynamical evolution in the jet's magnetized plasma environment. These findings provide new information on the evolution of the jet's magnetic field structure.

Lastly, we report space VLBI observations of the blazar 3C 279 at 22 GHz using the space radio telescope from the *RadioAstron* program, achieving an angular resolution of $\sim 26\mu$as with ground-space baselines up to 8 Gλ. The reconstructed image in total flux density and polarization shows electric vector position angles mostly aligned with the jet axis, consistent with the presence of a predominantly toroidal magnetic field. The fine-scale jet structure is traced up to ~ 180 parsec from the core, showing no signs of any filamentary structure previously observed in an earlier *RadioAstron* data study of the source, most likely due to the sparsity of the uv-coverage, and coinciding with a notable decrease in total jet intensity. The analysis of this follow-up work includes a synthetic data test and measuring the brightness temperature of the radio core, yielding an estimate of the intrinsic magnetic field strength of ~ 0.2 G, consistent with the jet being in equipartition.

Together, these studies provide new insights into the dynamics, magnetic field configurations, temporal and structure evolution, and imaging challenges of relativistic jets and supermassive black holes, contributing to the methodology and observational studies necessary to achieve a better understanding of these fascinating, yet still mysterious objects.

Resumen

Esta tesis estudia la estructura, dinámica y propiedades del campo magnético de los chorros relativistas en los núcleos activos de galaxias (AGN), utilizando observaciones de alta resolución con interferometría de muy larga base (VLBI) y algoritmos de reconstrucción de imagen. Para ello, se combinan tres estudios complementarios que abordan, en conjunto, los desafíos de reconstruir e interpretar estos objetos desde distintas perspectivas.

En primer lugar, desafiando los límites de la reconstrucción de imágenes de agujeros negros hacia la obtención de las primeras películas de estos objetos, presento el desarrollo y validación de un método de reconstrucción de imágenes basado en algoritmos de máxima verosimilitud regularizada (RML). Este algoritmo, integrado como parte de un esfuerzo conjunto dentro de uno de los proyectos más ambiciosos de la Colaboración del Telescopio del Horizonte de Sucesos (EHTC), incorpora la exploración de múltiples soluciones posibles mediante un algoritmo de optimización por enjambre de partículas multiobjetivo (`MO-PSO`). Esta técnica permite explorar de forma eficiente diferentes soluciones compatibles con los datos, lo que posibilita reconstrucciones dinámicas y en polarización de fuentes variables como Sagitario A* (Sgr A*), el agujero negro supermasivo en el centro de nuestra galaxia. Los datos utilizados fueron sintéticos, recreando las mismas características que los obtenidos por el EHTC de Sgr A*el 11 de abril de 2017, y se usaron para simular distintos modelos con variaciones en su morfología y complejidad dinámica. De este modo, se valida la capacidad del método para reconstruir estos modelos de forma robusta. Además, como resultado de la exploración multimodal, se obtiene un amplio conjunto de posibles soluciones que se ajustan a los datos, demostrando también que no todas ellas son físicamente plausibles.

En segundo lugar, presento un estudio de polarización en distintas frecuencias del cuásar 3C 273, utilizando observaciones con el Very Long Baseline Array (VLBA) a seis frecuencias distintas (5, 8, 15, 22, 43 y 86 GHz) para obtener mapas de intensidad total, polarización lineal y medida de rotación (RM). Los resultados muestran un claro gradiente transversal de RM a lo largo del chorro, lo que es indicador de la presencia de un campo magnético ordenado y helicoidal, que prob-

ablemente contribuye a la colimación del chorro. Al comparar con observaciones anteriores, se observan variaciones en la medida de rotación a lo largo del tiempo, lo que apunta a cambios dinámicos en el entorno magnetizado del recubrimiento del chorro.

Por último, pero no por ello menos importante, presento observaciones espaciales de VLBI del blázar 3C 279 a 22 GHz, realizadas con el radiotelescopio espacial del programa *RadioAstron*, alcanzando una resolución angular de aproximadamente 26 microsegundos de arco gracias a la presencia de líneas de base tierra-espacio de hasta 8 Gλ. La imagen reconstruida en intensidad total y polarización muestra ángulos del vector eléctrico (EVPA) alineados en su mayoría con el eje del chorro, lo que concuerda con la presencia de un campo magnético predominantemente toroidal. La estructura del chorro se puede seguir hasta unos 180 parsecs desde el núcleo, sin indicios de la estructura compuesta por filamentos observada en un estudio previo con datos también de *RadioAstron*, y coincide con una disminución notable en la intensidad total del chorro. El análisis incluye pruebas con datos sintéticos y la medición de la temperatura de brillo del núcleo, lo que permite estimar una intensidad del campo magnético intrínseco de alrededor de 0.2 gauss, de acuerdo con un chorro en equilibrio energético.

En conjunto, estos estudios ofrecen nuevos conocimientos sobre la dinámica, configuración del campo magnético, evolución temporal y estructural, y los retos en la reconstrucción de imágenes de chorros relativistas y agujeros negros supermasivos. Contribuyen así a mejorar tanto la metodología como los estudios observacionales necesarios para comprender mejor estos objetos tan fascinantes como enigmáticos.

Acknowledgements

Tantas cosas por decir y tan poco tiempo. Estos últimos meses han sido todo un desafío (para sorpresa de nadie) y una experiencia inolvidable en el sentido más completo de la palabra; y estos 4 años de doctorado, una vida entera. Y como no podía ser de otra manera, todo lo vivido no tendría ningún sentido sin la gente que me ha acompañado en el día a día, y por la cual merece la pena recordar cada segundo y momento de mi paso por el IAA.

En un alarde de originalidad me gustaría empezar dando las gracias a mi familia, que siempre ha estado apoyándome, escuchando y consolando, aún en ocasiones sin entender absolutamente nada. A mi pareja y amor de mi vida David, que durante años ha estado dando viajes entre ciudades para verme e incluso vivir conmigo, ha aguantado mis mejores y peores momentos, y sin ninguna duda ha sido, es y será todo lo que necesito.

Debo agradecer a mi director José Luis su gran labor en mi independencia como científica y su contribución durante la tesis, y al gran equipo con el que he tenido el placer de trabajar : Rocco, Ilje, Thalia, Antonio, Rohan, Marianna, Ailing, Kotaro, Jan y Maciek y en particular, me gustaría mandar un agradecimiento especial para Guang-Yao, por su paciencia y tiempo. Además, he tenido la suerte de poder relacionarme con científicos excepcionales con los que no solo he aprendido, sino también he entablado una relación de amistad, mil gracias Iván M.V, Tuomas S., Eduardo R. Por supuesto, en este grupo no podría olvidarme de Venky, a quién le sigo debiendo un abrazo, un chocolate caliente y una ruta donde no estemos a punto de morir congelados, de Alejandro Mus, con quién he acabado forjando una gran amistad y colaboración que ninguno nos esperábamos y que guardo con celo y alta estima (gracias por estar ahí, sobre todo en Slack, haciendo mis días y fines de semana más llevaderos), y de Hendrik Müller, un gran personaje y muy buen científico, colaborador y amigo.

Por supuesto, mi trabajo en el IAA-CSIC ha sido en parte financiado por el

Ministerio de Economía y competitividad español (PID2019-108995GB-C21), así que gracias por la oportunidad.

A santo de absolutamente nada salvo que puedo y quiero, voy a mencionar a mis mejores amigas del pueblo: Blanca, María y Sara, a las que quiero con locura y que han estado siempre en la distancia apoyándome y dejándome que me desahogase con todas mis tonterías, y a mi mejor amiga de la Universidad, Marina, a quién esperaré y nos sentaremos juntas frente al mar, y que se merece mi amor a pesar de dejarme en visto durante semanas porque siempre está cuando se la necesita, mi vida sería peor sin ella y nada más hay que decir.

Y ahora sí, que empiece el recorrido por el IAA como se merece (confirmo que se me caerán lágrimas durante los próximos minutos).

Me voy a permitir el capricho de empezar por la gente de portería, administración, limpiadoras y recursos humanos, que tienen el cielo ganado, y a quienes les he cogido mucho cariño. En especial, un gran beso y abrazo a mis porteros favoritos que siempre me saludan y me dicen lo guapa que voy y lo contenta que entro por las mañanas con mi música. Y por supuestísimo que otro beso y abrazo enormes se llevan Cristina, Maribel, Susana, Elisa, Francis, Alonso y Eva, que han estado ayudándome con los trámites y la burocracia y haciendo mis mañanas mucho más divertidas. En las sombras, mantenéis el centro a flote. Antxón e Isabel, el alma del IAA sin ningún tipo de dudas, gracias por vuestra dedicación y esfuerzo, por vuestras palabras de aliento cuando las he necesitado, por vuestra presencia a pesar de todas vuestras obligaciones. Gracias Severo Ochoa.

También tengo que agradecer a esa gente inesperada con la que he creado un vínculo de amistad, y que tanto me ha escuchado sin tener por qué: Pepe Vílchez, mi vecino favorito, Sara Cazzoli, una amiga y divulgadora fantástica, Manu García, un torbellino de energía positiva, Aurélien, mi francés favorito. Laura Hermosa, mi amiga y confidente, y representante de los predocs hasta que me pasó el relevo. He echado de menos nuestras charlas y tu presencia calmada; ha sido un honor haber tenido la oportunidad de llevar mi caos a ese grupo de personitas predocs que me han robado el corazón.

Que calienten que salen mis compis de despacho, desde el zulo hasta mi despacho final, todos y cada uno de ellos, que no hay espacio suficiente en este universo vacío para escribir lo mucho que les tengo que agradecer. Álvaro, Julio, Miguel, qué habría hecho yo sin vosotros (no respondáis, lo sabemos todos). Los abrazos, las sesiones de psicología barata, los dramas, los cotilleos, las conversaciones absurdas,

los dibujos en la pizarra, las sesiones de música improvisadas, los memes, las frases épicas ... Si es que os tengo que querer, gracias por haber sido los mejores compañeros de despacho que cualquiera podría desear, tenéis un lugar especial en mi corazón y jamás olvidaré lo feliz que he sido en vuestra compañía. Bet, Ailing, y durante un periodo pequeño pero no despreciable, Verónica, my sexy girls, sois lo mejor, nos hemos reído tanto juntas; no cambiéis jamás. Entre todos hebéis hecho del despacho un segundo hogar.

Y ahora ya sí, mis predocs, desde los que he visto marcharse hasta los que me verán marcharme. Es ejercicio trivial y no se moleste el lector en comprobarlo, que os adoro a todos y todas con locura, que muchos días habéis sido razón y excusa de ir a trabajar, que estos cuatro años a vuestro lado, conociéndoos, riéndonos y llorando juntos han sido el mejor resultado y conclusión que jamás podrá existir en esta tesis.

Laura H., Feli, Doran, Antonio F., el primer despacho que me hizo entender que de la tesis se puede salir, y con amigos de por vida. Antonio A., Anthony, Borja M. Juan, Julio, Guille, los grandes. La gente de mi año, Ana y Belén, mis dos mellizas, Luis, Borja, Miguel, Gerardo, Bet, Rohan y Marianna, mis compañeros de penas y alegrías desde el primer momento hasta el último. Si empiezo a contar todas las cosas que me habéis aportado me quedo sin espacio para la tesis, espero que sepáis cuánto os quiero (no suelo ser muy sutil) y que jamás olvidaré todos lo que hemos pasado juntos. Marta, nuestros momentos de piscina que me han dado la vida, Florín y Pol, con su flow inigualable, Ixaka, tan callado y simpático, pero con una vena dramaturga que ha sido precioso descubrir, Clara, con su personalidad cómica y arrasadora, Roberto, el escalador más pro que ha visto el IAA. Mil gracias por estar ahí y participar en todas las movidas, os adoro. Y no pueden faltar Sergio, mi ingeniero infiltrado favorito y que es uno más del grupo, Celia y Amanda, la razón de que cierto rap navideño épico (spoiler sí, he aquí el enlace para que jamás se pueda perder: https://www.youtube.com/watch?v=xBOJoI2XsYM) viera la luz en la mejor Fiesta de los Quesos que se ha hecho hasta ahora.

Y para terminar, los que para mí siempre serán "los de primero". Mis nuevos especímenes favoritos, un grupo de personajes a los que he cogido un cariño absurdo y que no cambiaría por nada. El trío de las supernenas: Alberto, Antonio y Javi, tenéis algo especial (y ruidoso). Sois descaradamente auténticos y simplemente os tengo que querer. Habéis sido un soplo de aire fresco con vuestra intensidad y dinámica aplastantes. Gracias por hacerme reír tanto y hacerme sentir parte del grupo, os habéis ganado un lugar en mi corazón. Irene, mi fuente de drama y cotilleo favorita, y compañera a deshoras en las tardes infinitas del IAA. Que nunca desaparezcan los planes improvisados ni la alegría que gen-

erais a vuestro alrededor. Gracias por todos los momentos compartidos. Querido despacho de la pecera (incluyendo a Carmen y Lucía), desafía todas las leyes lo poco que os conozco y lo mucho que os quiero. Gracias por vuestra amistad, confianza y compañía. Entre todos habéis hecho mucho más ameno este último año.

Mis queridos predocs, gracias a todos por ser tal y como sois, por soportarme y ser los mejores amigos, por las horas de descansos del café y las comidas, por las casas rurales, por las fiestas, rutas y quedadas, por responder siempre con una sonrisa cuando más lo necesitaba. Sois la verdadera alegría y energía que siempre me acusáis de tener. He aprendido las cosas realmente importantes a vuestro lado y solo me queda esperar que me recordéis con tanto cariño como yo a vosotros. Todo lo bonito que os diga es poco: sois unos científicos ridículos, maravillosos, divertidos, raros. Sois exactamente como debéis, y el sueño de cualquiera (y quién diga lo contrario, me mandáis nombre y ubicación y lo reviento). Sospecho que pasará un tiempo antes de que deje de esperar vuestras voces, saludos y abrazos todas las mañanas; os echaré de menos.

Y como se puede ser un poco más malvada y cursi todavía, me voy a tomar la libertad de darme a mí misma un pequeño gracias, por quererme y ser tal y como soy, así que por eso mismo también voy a plasmar el sentimiento que me genera esta despedida, este fin de una era, en un poema.

Me marcho,
y mis historias se vendrán conmigo,
navegando entre las lágrimas compartidas
con la gente a quien mis días dedico.

Rellenaré el vacío con anécdotas,
compararé el futuro con lo que ya ha sido,
contemplaré con hastío la lejanía,
y la nostalgia invadirá mis noches
y retará al olvido.

Con alivio y dolor me retiro,
rozaré el descanso
de haberlo conseguido,
y sin tener sentido
no querré irme,
aún cuando ya me habré ido.

Prometeré tantas cosas
que nunca he cumplido,
miraré hacia atrás
y transcurrirá un latido,
y me ataré naúfrago del mundo
y esperaré que la marea
me traiga consigo.

Volveré, y seguirá el cohete
en la entrada,
las banderas despintadas,
las hojas secas
por el suelo en desbandada,
como mis recuerdos que amenazan
con desbordar la realidad.

Habrán pasado demasiados años,
pero seguiré viendo las mismas caras,
las conversaciones seguirán intactas,
los pasillos abrazarán mis pisadas
y mis pies repetirán un camino
forjado en años, en esfuerzo,
en sonrisas y entre pantallas.

No dejaré que se vaya,
esto no,
este pedacito de todo y de nada
quedará grabado por siempre
al menos en estas pocas palabras.

Quizá no vuelva a ver
las mesas llenas de comida,
de ruido, de sueños,
de esperanzas y penas,
de comienzos y despedidas.
Quizá haya amistades que
la distancia y el tiempo pierdan,
quizá la ciencia no encuentre
nunca nuestras respuestas.

Pero a pesar de todo,
pude haber sido cualquiera,
vivido de cualquier forma,
trabajado en cualquier lugar,
conocido a gente de otras tierras,
deseado cualquier cosa,
esperado de la vida un poco más.

Y sin embargo he mirado
a mi alrededor
y he podido decir:
aquí estoy yo, con vosotros,
en este momento,
y creo que nunca quise nada más.

List of Tables

List of Figures

Table of Contents

Chapter 1

Introduction

Astrophysics is a wide and fascinating realm to explore, but you simply cannot go wrong with one of the most well-studied objects: Active Galactic Nuclei (AGN).

As we shall see, these objects have been continuously observed and analyzed throughout time, gifting us with a myriad of both answers and questions. In particular, scientists have been captivated with one of the most exotic relationships of our universe: the connection between the supermassive black hole (SMBH) at the center of the AGN and the relativistic jet being launched from it.

This thesis is devoted to the study of this connection. In order to do so, it encompasses three different approaches, each focusing on a particular aspect that will help widen the understanding of their relationship.

First things first, to facilitate the reading of this work, we start with an introductory section reviewing basic concepts regarding AGN, jets and black holes, setting a theoretical foundation. Complementary, we will briefly present an overview of radio interferometry and the diverse imaging strategies used to overcome the current observational limitations. This will mainly constitute the methodology employed throughout this work.

From there, the journey begins at the very heart of the mystery: the supermassive black hole. We will entertain the possibility of finding and recovering dynamics in these objects using multimodality algorithms, and show how this will impact future science and the understanding of black hole physics as we know it.

Secondly, moving away from the black hole and focusing on the jet, this work will also present a rotation measure analysis using VLBA multifrequency

observations of the quasar 3C 273. By doing so, the structure of the magnetic field within the jet can be determined, motivating a better understanding of the physical processes taking place in relativistic jets.

Last but not least, we will finish the journey by further exploring the jet, but at unprecedented high resolution ($\sim 26\mu$as) thanks to the space-VLBI mission *RadioAstron*, thus acquiring a privileged look at the innermost region of the quasar 3C 279. While earlier RadioAstron studies have reported a filamentary jet structure in this source, those results were based on a previous epoch with different uv-coverage and jet brightness conditions. In our new observations, taken during a fainter state of the jet, we detect no such filamentary substructure, suggesting that these features may be transient or sensitive to the observing conditions. We perform synthetic data tests to assess whether the lack of filaments and analyze the brightness temperature of the core and estimate the intrinsic magnetic field strength, finding values consistent with near-equipartition. This way, we highlight the advantages of including an orbiting space radio telescope in VLBI observations, as well as emphasize the variability and complexity of the jet morphology in this blazar.

In the hopes that the reader managed to survive such a perilous quest, they will find the conclusions from this thesis summarized in a final section that may as well be a sour ending as much as a sweet beginning. The game is afoot, let us begin.

1.1 Active Galactic Nuclei

The concept of Active Galactic Nuclei (AGN) dates back to 1943, when Carl Seyfert discovered a class of galaxies with bright central regions and broad emission lines. Following observations revealed sources of intense radio emission with compact optical counterparts, which came to be known as quasi-stellar radio sources, or quasars. The first quasar, 3C 273, was identified by Maarten Schmidt in 1963, marking a turning point in AGN research (see also Section 1.1.1). The point-like structure of these objects indicated that their emission outshone the surrounding gas and stars, suggesting that the dominant energy source was concentrated in the galaxy's nucleus. These galaxies were then collectively named Active Galactic Nuclei, currently recognized as some of the most powerful and extensively studied objects in astrophysics.

AGNs are characterized by compact central regions that emit enormous amounts of energy, often surpassing the luminosity of an entire galaxy by a factor of 10 to 100 (Krolik 1999). They exhibit high variability and intense emis-

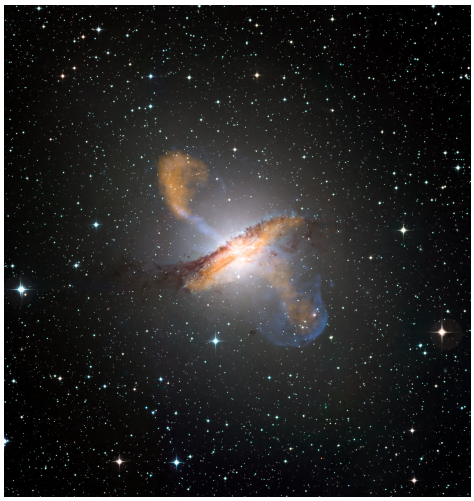

Figure 1.1: Colour composite image of the AGN Centaurus A, revealing the lobes and jets emanating from its central black hole. The 870-micron submillimetre data, from LABOCA on APEX, are shown in orange. X-ray data from the Chandra X-ray Observatory are shown in blue. Visible light data from the Wide Field Imager (WFI) on the MPG/ESO 2.2 m telescope located at La Silla, Chile, show the background stars and the galaxy's characteristic dust lane in close to "true colour". Credit: ESO/WFI (Optical); MPIfR/ESO/APEX/A.Weiss et al. (Submillimetre); NASA/CXC/CfA/R.Kraft et al. (X-ray)

sion across the electromagnetic spectrum. Such extreme energy output must originate from gravitational processes, specifically from the accretion of matter onto a supermassive black hole (SMBH) at the galaxy's core.

Observational evidence for SMBHs in AGNs comes from multiple fronts. Stellar dynamics have provided some of the strongest confirmations, particularly in the case of the Milky Way's central black hole, Sgr A*, whose mass was measured by tracking the orbits of nearby stars (Ghez et al. 2008; Gillessen et al. 2009; Genzel et al. 2010)-a discovery that earned Reinhard Genzel and Andrea Ghez the 2020 Nobel Prize in Physics. Similarly, Very Long Baseline Interfometry (VLBI) observations of M87* in 2017 by the Event Horizon Telescope (EHT) produced the first direct image of a black hole's event horizon (Event Horizon Telescope Collaboration et al. 2019a,b,c,d,e,f), further confirming the SMBH paradigm. Additionally, broad and narrow emission line studies also support the presence of massive, compact objects at the centers of AGNs.

In some AGNs, such as Centaurus A in Figure 1.1, a fraction of the infalling material is ejected perpendicularly to the accretion disk, forming relativistic, highly collimated plasma flows known as *jets*. These dramatic outflows were first observed more than a century ago by (Curtis 1918), who noted a "curious straight ray" extending from the nucleus of M87, an observation now understood as one of the earliest records of a relativistic jet. The formation and collimation of these jets are believed to be driven by strong magnetic fields threading the accretion disk. These jets are known to extend up to megaparsec (Mpc) scales (Oei et al. 2024), transporting energy and matter far beyond the host galaxy. Details regarding the launching mechanisms, physics and properties of radio jets can be found in Section 1.2.

A major breakthrough in the study of quasars, a subclass of AGNs (see also Section 1.1.1 for more detail on AGN classification), came with the development of VLBI aperture synthesis. This technique combines signals from multiple radio telescopes to achieve an angular resolution equivalent to that of a telescope spanning the entire distance between them (Ryle 1952; Jennison 1958; Kraus & Tiuri 1966; Burke & Graham-Smith 2010). The advancement of this technique was crucial in modern radio astronomy, also contributing to Martin Ryle's Nobel Prize in Physics in 1974. Nowadays, VLBI remains fundamental to high-resolution observations at radio wavelengths. Further discussion of this technique is presented in Section 1.4.2.

1.1.1 Classification and Unified model

The number of discovered AGNs increased exponentially in the late 20^{th} century, making a classification system necessary. Initially, the classification was based on factors such as luminosity, variability, and spectral morphology. However, the overlap of characteristics across different categories made it difficult to establish clearly distinct groups.

Beyond traditional classifications, in literature AGNs are still classified in two categories based on their ratio of radio to optical emission, typically quantified by the parameter $R = L_{radio}/L_{optical}$ (e.g., Kellermann et al. 1989):

- **Radio-Loud objects:** Theu have $R > 10$, meaning they have strong radio emission relative to their optical emission, and usually produce large-scale radio jets and lobes. The kinetic power of the jets is a significant fraction of the total bolometric luminosity. Also, they are generally associated with elliptical galaxies with recent mergers. They comprise around 10–15% of all AGN (Blandford et al. 2019).

- **Radio-Quiet objects:** They have $R < 10$, that is, they exhibit weak radio emission for the same optical luminosity and often lack the presence of large-scale jets. They can be generally found in spiral galaxies.

This classification also correlates with differences in their spectral energy distributions (SEDs). In radio-loud AGN, specially blazars, the SED typically shows two broad peaks: a low-frequency peak from synchrotron radiation and a high-frequency peak attributed to inverse Compton scattering. These non-thermal components dominate the broadband emission and reflect the presence and orientation of relativistic jets. In contrast, radio-quiet AGN often display SEDs dominated by thermal emission from the accretion disk and dust, with little to no jet contribution.

Historically, the first distinct class of AGN identified was Seyfert galaxies (Seyfert 1943), which exhibited great luminosity and stellar-like nuclei with prominent broad optical emission lines. Later, in the 1950s, the emergence of radio astronomy gave rise to the discovery of radio galaxies (e.g., Bolton et al. 1949; Baade & Minkowski 1954), characterized by having extended radio-emitting, large-scale, energetic outflows from galactic nuclei.

In 1963, Schmidt (1963) analyzed the bright radio source 3C 273 and discovered that it exhibited a substantial redshift, indicating cosmological distances and extreme luminosities. This breakthrough led to the identification of quasi-stellar radio sources (QSOs or quasars), which were characterized by strong radio emission (radio-loud) and broad optical emission lines. Following surveys (Sandage 1965; Schmidt & Green 1983) uncovered a population of radio-quiet quasars, broadening the existing classification to include sources without strong radio emission.

In the 1970s, objects exhibiting rapid variability, high polarization, and nearly featureless optical spectra were identified as BL Lacertae objects (e.g., Strittmatter et al. 1972), which, together with optically violent variable quasars (OVVs), were later clustered into the category of blazars (e.g., Angel & Stockman 1980), unified by their orientation along relativistic jets pointing close to the observer's line of sight. At the same time, Fanaroff & Riley (1974) introduced a morphological classification of radio galaxies based on the radio luminosity and the spatial distribution of radio brightness within their lobes. This way, they distinguished between FR I and FR II sources, which display edge-darkened and edge-brightened morphologies, respectively. In 1980, Heckman (1980) proposed the class of Low-Ionization Nuclear Emission-line Regions (LINERs), defined by optical spectra dominated by low-ionization forbidden lines, representing a lower-luminosity form of nuclear activity.

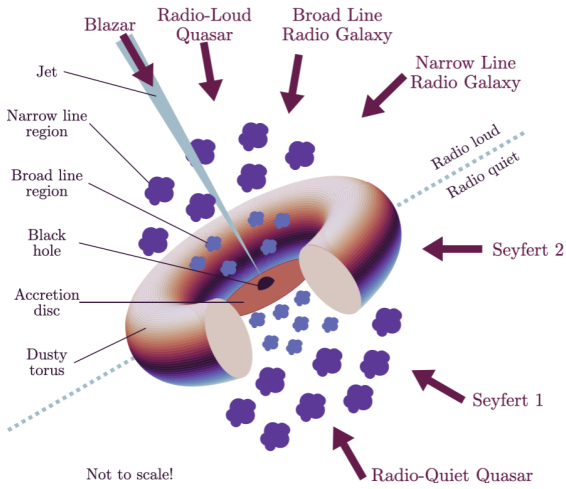

Figure 1.2: Artistic representation of the unified model for AGNs. Credit: Emma L. Alexander, taken from https://commons.wikimedia.org/wiki/File:Emmaalexander_unified_agn.png.

By the 1990s, Antonucci (1993) and Urry & Padovani (1995) used the accumulated evidence to unify the previous classification (Seyfert galaxies, quasars, radio galaxies, and blazars) under the broader term active galactic nuclei, and established the unified model of AGN.

In this model (represented in Figure 1.2), these different types are interpreted as similar systems. The unified model contemplates a central supermassive black hole (SMBH) at the center of the AGN, surrounded by an accretion disk that generates the observed luminosity. Some of the accreting material in this disk is funneled into the launching of relativistic jets at relativistic speeds, in accordance with the conical jet model (Blandford & Konigl 1979) (see Section 1.2.5).

In addition to the SMBH and accretion disk, the model incorporates two further spectroscopic regions:

The Broad Line Region (BLR): Located at 0.01–1 pc from the central black hole, it consists of clouds moving at velocities up to 10,000 km/s. These clouds produce broad emission lines, observable in direct spectra when AGNs are viewed face-on, or in polarized light when they are viewed edge-on.

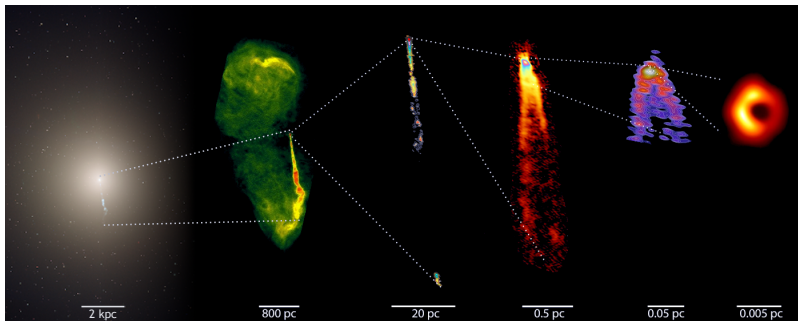

Figure 1.3: M87 multi-frequency images. Credit: Gurvits et al. (2022)

The Narrow Line Region (NLR): Found at 1–100 pc, the NLR consists of lower-velocity clouds ($\sim$ 1,000 km/s) responsible for narrow emission lines.

Surrounding the central region is a dusty torus, with a size larger than the accretion disk and located several parsecs from the SMBH. This toroidal structure absorbs UV radiation from the accretion disk and re-emits it in the infrared. The torus also determines the classification of AGNs based on viewing angle:

- **Type 1 AGNs:** Observed at smaller angles relative to the jet direction, allowing a clear view of the BLR.
- **Type 2 AGNs:** Observed at larger angles, where the torus obscures the BLR, leaving only narrow emission lines visible.

The observing differences among Seyfert galaxies, quasars, radio galaxies, and blazars can be then explained in terms of orientation-dependent obscuration and relativistic beaming effects, as well as intrinsic differences in luminosity and accretion rates. Although the unified model is widely accepted nowadays, it remains incomplete.

Despite the many advances regarding our understanding of AGNs, there are still several major and unresolved questions involving these sources, their evolution and their jet formation. Before diving into the strategies and studies that try to shed some light into these questions, we will first need to approach the very core of AGNs: supermassive black holes.

1.1.2 Supermassive black holes

Supermassive black holes (SMBH) are generally defined as black holes with masses of the order of 10^6 to 10^{10} $M_\odot$. Despite their great mass, the average density of a SMBH within its event horizon (calculated as its mass divided by the volume enclosed by the Schwarzschild radius) can be lower than that of water. This arises because the Schwarzschild radius scales linearly with mass, while the volume does with the cube of the radius. Therefore, the density of a black hole is inversely proportional to the square of the mass, and thus higher-mass black holes have lower average density (Celotti et al. 1999; Baaquie & Willeboordse 2015).

The story of black holes begins with the idea of a theoretical object with an escape velocity exceeding the speed of light, proposed by Michell (1784)and Laplace (1796) within the framework of Newtonian mechanics. Later on, a more formal mathematical foundation on the subject took place in 1916 when Karl Schwarzschild derived his metric as a solution to Einstein's field equations of general relativity (Schwarzschild 1916). This solution described the curved space-time around a spherically symmetric, non-rotating mass and introduced the concept of the Schwarzschild radius, which defines the event horizon—the boundary beyond which nothing, not even light, can escape.

The true nature of black holes remained uncertain for decades, until in 1939, Robert Oppenheimer and Hartland Snyder demonstrated that gravitational collapse of a sufficiently massive object would inevitably lead to a singularity hidden within an event horizon (Oppenheimer & Snyder 1939). Roger Penrose later formalized this understanding by introducing the concept of a trapped surface, proving that once such a surface forms, collapse into a singularity is inevitable (Penrose 1965), a result that earned him the Nobel Prize in Physics in 2020 for his contributions to the theory of black hole formation. With this, black holes were finally established as a fundamental prediction of general relativity.

The detection of quasars in the late 1950s marked the first observational hint of SMBHs. These extremely luminous, compact radio sources were initially puzzling until Maarten Schmidt identified the source 3C 273 as an extragalactic object with an immense energy output (Schmidt 1963). The energy required to sustain such luminosities ruled out conventional stellar processes, leading to the hypothesis that quasars were powered by accretion onto SMBHs. Donald Lynden-Bell further developed this idea, suggesting that most galaxies, including the Milky Way, harbor SMBHs at their centers (Lynden-Bell 1969).

In 1977, Roger Blandford and Roman Znajek built a model by which a rotating black hole, interacting with magnetic fields, could extract energy to

power relativistic jets (Blandford & Znajek 1977), acting like a huge dynamo. This mechanism remains one of the most studied regarding jet formation in AGN (see also Section 1.2.1). Complementarily, in 1982, Blandford and Payne demonstrated that energy and angular momentum could also be extracted from the accretion disk if the magnetic field lines are inclined at less than 60° to the disk surface (Blandford & Payne 1982), enabling the launching of magnetocentrifugally driven winds.

Moving on to the early 1990s, the achievable spatial angular resolution in astronomical observations was not enough to detect supermassive black holes. Instead, astronomers focused on determining the masses of compact objects at galactic centers by tracking stellar motion. For instance, the Hubble Space Telescope (HST) results were early evidence for the presence of a supermassive black hole at the center of the elliptical galaxy M87 (see at different scales in Figure 1.3), even though alternative explanations such as dense stellar clusters were also possible.

The most definitive evidence for the existence of a SMBH finally came from our own Galactic Center. Reinhard Genzel and Andrea Ghez led two independent teams that monitored for nearly three decades the orbits of individual stars around the source Sagittarius A* (Sgr A*), located about 25,000 light-years from Earth (Schödel et al. 2002; Ghez et al. 2003). The star S2 (also known as S02) was the one to originate the breakthrough, completing a full orbit around Sgr A*in just 16 years. The Keplerian motion found was consistent with a central point mass of about four million solar masses, ruled out other explanations such as a dense cluster of stellar remnants, therefore robustly supporting this object to be a SMBH. These findings earned Genzel and Ghez the 2020 Nobel Prize in Physics.

The strongest evidence of the existence of SMBHs came with the technological advance of VLBI at milimeter wavelengths. In 2019, the Event Horizon Telescope Collaboration (EHTC) released the first-ever image of the black hole in the galaxy M87 (Event Horizon Telescope Collaboration et al. 2019a,b,c,d,e,f), showing an asymmetric ring of emission surrounding a dark central shadow. The observed structure (see Figure 1.4, left panel) was consistent with general relativistic predictions of light bending around a Kerr black hole. The impact of this release, both scientifically and among the public, was extraordinary and felt around the globe. In fact, according to the European Southern Observatory (ESO), about half of the world's population has seen this image, making it one of the most iconic images in astronomy, alongside the famous Earthrise photo taken by Apollo astronaut William Anders on December 24, 1968.

Building on this groundbreaking discovery, in 2022 the EHTC released the

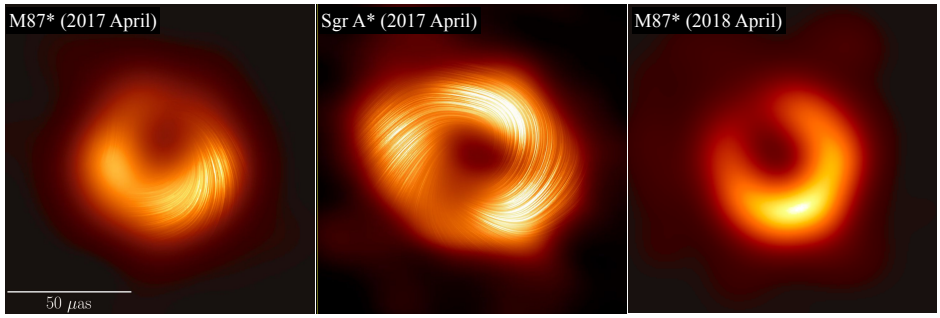

Figure 1.4: First images of black holes by the EHTC, observing M87* and the galactic center, SgrA*. The images show a bright ring of emission produced by the strong light bending near the event horizon of the black hole. Left and middle images also show polarization field lines plotted atop an underlying total intensity image (Event Horizon Telescope Collaboration et al. 2021, 2024a). These long-sought images provide the strongest evidence to date for the existence of supermassive black holes. Credit: EHT Collaboration.

second image of a black hole, Sgr A*(Event Horizon Telescope Collaboration et al. 2022a,b,c,d,e,f, 2024a), providing for the first time direct evidence of the SMBH at the center of our galaxy (see Figure 1.4, central panel). Unlike M87, which exhibits a more stable jet and accretion structure, Sgr A*presented considerable observational and theoretical challenges. For instance, its mass is much smaller (about 4 million solar masses compared to M87's 6.5 billion), which translates into dynamical timescales of just a few minutes. That is, the source is fastly evolving during the observations, which usually take a few hours. This variability, combined with interstellar scattering effects along the line of sight, made it necessary to develop and employ advanced imaging frameworks, including dynamic modeling techniques, to recover the underlying structure.

Despite these difficulties, the EHTC reconstructed a ring-like structure with a diameter consistent with predictions for a Kerr black hole for both M87 and Sgr A*, further supporting general relativity in the strong-field regime. By comparing the data to GRMHD simulations (such as the one shown in Figure 1.5), the inclination angle of the black hole was constrained to be low to moderate, with a preference for spin vectors roughly aligned with the Galactic plane. Nevertheless, spin magnitude remained largely unconstrained. Moreover, while the average structure was consistent with a gravitationally lensed photon ring, the EHTC data suggested variability in the brightness distribution around the ring, likely due to turbulent accretion dynamics and hot spot motion near the event horizon (Event

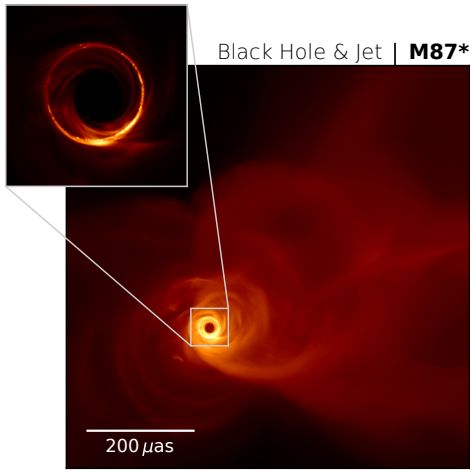

Figure 1.5: GRMHD simulation of the supermassive black hole M87 and its jet, including a zoom-in into the photon ring. Credit: EHT Collaboration.

Horizon Telescope Collaboration et al. 2019c). Importantly, the comparison to GRMHD models favored scenarios involving magnetically arrested disks (MADs) in the case of M87, as seen in Figure 1.5). These MADs are characterized by having a strong magnetic flux accumulation near the black hole. These configurations favor the launching relativistic jets via the Blandford–Znajek mechanism.

In addition, the EHTC also conducted polarization studies of both M87 and Sgr A*(Event Horizon Telescope Collaboration et al. 2021, 2022f). For M87, the polarization fraction measured by the EHTC was around 5–10%, with electric vector position angles (EVPAs) primarily tangential to the ring, consistent with ordered, toroidal magnetic fields near the black hole. While M87 exhibits a more ordered field structure and prominent jet activity, the environment of Sgr A* appears to be more variable and less polarized, with lower net polarization fractions and a preference for Standard And Normal Evolution (SANE) models with weaker, less coherent magnetic fields. Complimentary, the EHT also tested their capabilities by probing the connection between SMBH and their relativistic jets, through the observation of quasars like 3C 279 and 3C 273 (Kim et al. 2020a; Okino et al. 2022).

Both results provided strong constraints regarding SMBHs, confirming general relativity's predictions to within a few percent. These studies also demonstrated that for the first time, SMBHs can finally be studied directly, turning the event horizon from a purely theoretical concept to a physical observable.

Nevertheless, there are still many open questions regarding the study of black hole accretion such as the influence of magnetic fields in jet formation, their role in galaxy evolution, or deviations from general relativity. Future observations with next-generation EHT (ngEHT) (Doeleman et al. 2019) and space-bsed interferometry (projects such as *RadioAstron* (Kardashev et al. 2013) and, in the future, BHEX (Johnson et al. 2024)) will hopefully improve our knowledge on the mysteries of black holes and their relativistic jets.

1.2 Relativistic jets in AGN

1.2.1 Jet formation

Jets are defined as relativistic plasma flows ejected from the AGN central engine. Their origin (also referred as formation and launching) is thought to come from the interaction between a SMBH and an accretion disk. The inner regions of the disk experience a stronger gravitational effect, resulting in differential rotation. This rotation, combined with a magnetic field anchored in the disk, generates a helical field structure that extracts and collimates material from the disk (see Figure 1.6). In this way, the toroidal component of the magnetic field would play a crucial role in shaping and collimating the jet. As particles travel along the jet, their magnetic pressure is reduced, hence leading to acceleration.

The main models describing jet launching mechanisms are: the *Blandford-Znajek* process (Blandford & Znajek 1977), in which rotational energy is extracted from a spinning black hole via magnetic fields, and the *Blandford-Payne* mechanism (Blandford & Payne 1982), where magnetically driven winds from the accretion disk accelerate material outward. These processes allow AGNs to power jets that not only carry energy at relativistic speeds but also interact with their environment on galactic and extragalactic scales.

Since jets are composed of relativistic plasma they can be treated as fluid events, since the interplay between plasma motion and magnetic fields enables a coherent, structured outflow. That is to say, their properties on parsec and kiloparsec scales can be interpreted rather accurately by implementing relativistic hydrodynamics laws (Ferrari 1998). Nevertheless, the details on their launching, acceleration and collimation mechanisms are still a mistery to us all, which is the reason why observational monitoring of jet properties and evolution are so important to improve the current models.

From the numerous studies about the formation of jets, as mentioned before, a widely accepted scenario is that there is a certain correlation between the formation of the jets and the accretion. The general belief is that jets are launched

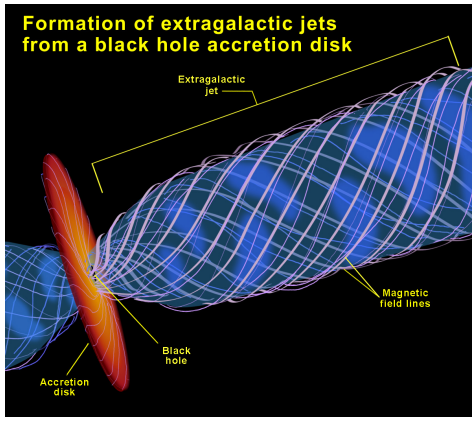

Figure 1.6: Artistic impression of the formation of M87 jet. Credit: NASA/ESA and Ann Feild.

by relativistic magneto-hydrodynamic (RMHD) processes, being the energy source of the jets given by the accreted matter (Blandford & Znajek 1977a; Blandford & Payne 1982; Meier et al. 2001).

Once the plasma is channeled into a jet, the flow energy is essentially dominated by the magnetic field, which has to be turned into kinetic energy (Blandford & Znajek 1977b; Komissarov & Barkov 2007). In addition, some mechanism must collimate the flow that yields the observed small opening angles. The conversion mechanish of Poynting flux, through which the jet is accelerated and collimated, is another tricky and strongly debated topic (Lyubarsky 2009). The most popular theory is the magnetic launching theory, which implies that the field is initially mostly poloidal, while the field structure is subject to change as the jet expands (McKinney 2006; Gómez et al. 2000).

For instance, Marscher et al. (2002) were the first to establish the disk–jet connection by using time-dependent multi-frequency polarimetric monitoring. They found a link between activity in the accretion disk and the subsequent emergence of polarized emission in the jet. Their work demonstrated that disturbances originating near the black hole (likely associated with magnetic reconnection or injection events in the disk or corona) propagate downstream and evolve into shocks within the jet.

The flow acceleration is thought to be governed by different mechanisms (Meier 2012). The two main variables are the speed of the flow and the magnetic field structure. The former is associated to the existence of critical surfaces, related

with each magnetic wave, registering the location where the flow becomes as fast as the wave. Since the information carried by a certain type of wave is unable to cross its own critical surface, we can identify different regimes in the acceleration region. In fact, at the launching point, close to the surface of the accretion disk, the flow speed is low enough so that hydrodynamic processes can take place (Ferreira 1997).

Over the slow magnetosonic limit, there is only magnetic acceleration. If we assume a cool disk, the magnetic pressure dominates over the gas pressure and the field can be considered force-free (Camenzind 1986; Vlahakis & Königl 2004). Under these conditions, the description of the acceleration mechanism in the force-free region depends on the reference frame. For example, if the process is observed in an inertial frame (point of view of the observer), the magnetic field appears with an azimuthal component and the acceleration, driven by the magnetic pressure gradient. This description is valid up to the Alfvén radius, i.e until the flow speed is lower than the Alfvén speed. From that point on, the field has a considerable toroidal component (also in the frame of the central object) and acquires a helical geometry. This magnetic pressure gradient keeps governing the flow until the fast magnetosonic critical surface (the last speed barrier) (Vlahakis & Königl 2004; Komissarov & Barkov 2007). Regardless, the speeds measured in jets normally exceed their fast magnetosonic limit (e.g., Lister et al. 2016).

1.2.2 The role of magnetic fields

Beyond their role in launching, magnetic fields are also essential in the accretion process itself, providing the mechanism by which angular momentum is transported outward, allowing matter in the disk to spiral inward rather than remaining in Keplerian orbits. This is typically attributed to magnetohydrodynamic turbulence driven by the magnetorotational instability (MRI; Balbus & Hawley 1991), commonly accepted as the cause of this angular momentum dissipation. Moreover, the geometry and order of these fields help determine the jet's physical conditions. A sufficient ammount of magnetic flux in the inner disk is also necessary for launching magnetically dominated jets, as stated in the concept of a magnetically arrested disk (MAD; Narayan et al. 2003; Tchekhovskoy et al. 2011). Additionally, the magnetic field configuration contributes significantly to jet collimation, helping maintain narrow structures across kiloparsec scales (Begelman et al. 1984; Lyubarsky 2009).

A direct observational feature to the magnetic field structure is the jet's polarization, through the electric vector position angle (EVPA). At radio wavelengths, jets predominantly emit synchrotron radiation (see Section 1.2.5 for more details), which is intrinsically polarized. In optically thin regions (see Section 1.3.2), the

theoretical maximum linear polarization can reach $\sim 75\%$, but in practice, it is reduced due to Faraday depolarization, turbulence, and beam depolarization (Burn 1966; Gardner & Whiteoak 1966). Polarization maps from VLBI observations and monitoring programs, for instance, show that in many cases, these jets present a more dominating toroidal magnetic field, which is consistent with the hypothesis that they are threaded by a helical magnetic field.

1.2.3 Instabilities

In addition to the jet launching and formation, there is also the question of jet stability. The jet flow can potentially be disrupted and lead to turbulence by what is known as plasma instabilities (Hardee 2008; Perucho et al. 2012). The two main classes of instabilities affecting jets are:

Current-Driven (CD) Instabilities: They arise in magnetically dominated jets due to the presence of strong toroidal or helical magnetic fields (Mizuno et al. 2007, 2011). They can lead to the internal reconfiguration of magnetic structures, even affecting jet propagation, or even fully disrupting the jet.

Shear-Driven Instabilities: Velocity shear at the jet boundary can trigger instabilities that cause mixing with the surrounding medium, potentially affecting collimation (Hardee 2000, 2007).

Both instabilities are expected to affect jet dynamics and, in principle, could lead to jet disruption on observable scales (see Hardee 2008; Perucho et al. 2012). Surprisingly, the perseverance of observed well-collimated jets over long distances suggests the presence of stabilizing mechanisms that counteract the instabilities effect and avoid full jet disruption (Oei et al. 2024).

The jet stability depends on the system's response to small perturbations. A stable state is able to return to its initial or almost initial state (e.g., Hardee 2008). On the other hand, an unstable system will let perturbations change the fluid structure either towards turbulence or a new flow configuration. These disturbances can operate on small scales (microdisturbances), modifying the velocity distribution and plasma properties but not really changing the large-scale jet morphology. Alternatively, they can also occur at larger scales (macrodisturbances), which in turn can be classified into:

Rayleigh-Taylor (RT) instability occurs when two fluids of different densities coexist, resultingin the penetration of the denser fluid into the less dense medium (Matsumoto & Masada 2013). These kind of instability is usually not very relevant in relativistic jets, but it can have a role where a heavy jet interacts with a lighter

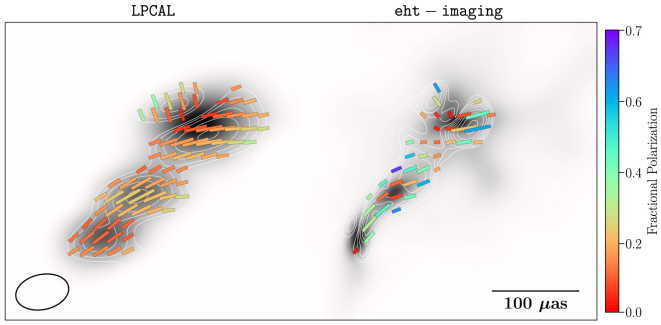

Figure 1.7: Polarized image of the candidate binary black hole system OJ 287 with the first GMVA + ALMA observations. Credit: Zhao et al. (2022).

external medium in a non-inertial frame.

Kelvin-Helmholtz (KH) instabilities, on the other hand, take place at shear interfaces where two fluids move at different velocities (Blake 1972; Hardee 2000). They can also grow into nonlinear structures that mix jet material with the external medium and can lead to shock formation.

Observational evidence of these instabilities comes in the form of helical patterns, limb brightening or filaments in VLBI observations (Lobanov & Zensus 2001; Perucho et al. 2014; Fuentes et al. 2023).

1.2.4 Observational aspect of AGN jets

AGN jets emit across the entire electromagnetic spectrum, though this thesis focuses on radio wavelengths. Their internal structure can be resolved using VLBI, a technique that is able to achieve extreme angular resolution (see Section 1.4.2). Large-scale jets extend over kiloparsec scales, showing changes in their structure both in frequency and time. For instance, jets FRII AGN show bright terminal hotspots due to interactions with the intergalactic medium, while FRI AGN display more diffuse, curved jets (Fanaroff & Riley 1974).

At smaller scales, though, jets are seen as a compact core and one or more bright regions known as components. The core is usually attributed as the brightest feature at one of the ends of the jet, while the components often appear as moving spots at superluminal speeds due to relativistic effects (e.g., Rees 1966; Cohen et al. 1971; Blandford & Konigl 1979; Gómez et al. 2000, 2001), and are mostly interpreted as shock waves propagating through the plasma (Marscher & Gear 1985; Gomez et al. 1995; Gómez et al. 1997; Jorstad et al. 2005a). The presence of

these components is attributed to the instabilities in the accretion disk, leading to injections in the jet (shocks).

Recent studies with high-resolution VLBI observations have revealed the innermost region of AGN jets on a finer scale (Gómez et al. 2000; Gómez et al. 2016, 2022; Event Horizon Telescope Collaboration et al. 2022a; Okino et al. 2022; Zhao et al. 2022; Lu et al. 2023; Fuentes et al. 2023; Cho et al. 2024, , and references therein), which combined with the increasing technical capabilities of future upcoming observations, seem to harbor promising advancements regarding our understanding of jet processes.

In order to physically describe the challenging environment in the surroundings of supermassive black holes and accretion disks where jets are observed, it is required a full General Relativistic Magneto-HydroDynamic (GRMHD) formalism (Koide et al. 1999; McKinney 2006). Apart from that, numerical simulation have advanced and increased its complexity to test the different theories and try to reproduce the observed properties of jets on various scales (Mizuno et al. 2007, 2011, 2012; Fuentes et al. 2018, 2021).

1.2.5 Conical jet model

The most accepted model is the *conical jet model* or accretion-ejection model, originally formulated by Blandford and Königl (Blandford & Konigl 1979) as a synchrotron emission model for compact radio cores, and further expanded by Blandford and Payne (Blandford & Payne 1982) as an accretion-driven jet launching mechanism. While the model assumes a conical geometry for simplicity, high-resolution observations of sources such as M87 reveal that jets typically exhibit a parabolic expansion near the base, transitioning to a conical shape on larger scales (Asada & Nakamura 2012). A representation can be found in Figure 1.8.

This model involves large-scale magnetic fields threading the accretion disk surrounding a central compact object, from which a conical or parabolic jet is launched. The magnetic field, anchored to the accretion disk, can wrap itself in a helical configuration as a result of differential rotation (see also Section 1.2.2). Angular momentum and energy are transferred from the disk along the field lines, channeling and accelerating plasma away from the disk surface. The inertia of the plasma, in turn, induces the magnetic field lines to curve, thus generating a toroidal component that helps collimate the plasma flow.

In this context, and given that jets are powered by the accreted material from the disk, there must be a relation between the disk emission and the jet. The first

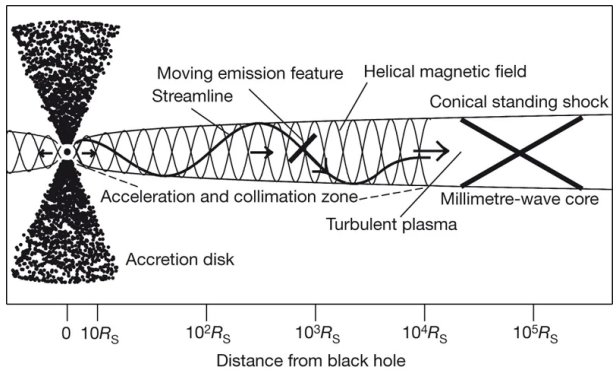

Figure 1.8: Conical jet model representation where a shock propagates down the jet along a spiral streamline and cycles through the orientations of the helical magnetic field. The distance from the black hole is in logarithmic scale, shown in terms of the Schwarzschild radius (R_S). Credit: (Marscher et al. 2008).

observational evidence supporting this model was obtained by Marscher (Marscher et al. 2002) studying the radiogalaxy 3C 120 in X-rays and radio. Their results implicate that not all the material in the inner region of the disk falls into the black hole, but instead a part of it is injected into the jet, thus confirming the hypothesis that the observed jets are generated as a consequence of the accreted material surrounding the black hole.

Although this conical jet model is useful in terms of explaining flat radio spectra, it oversimplifies the true jet structure. For instance, observations of M87 jet reveal a parabolic geometry near the base, transitioning to conical only at larger scales (Asada & Nakamura 2012). This model also forsakes any time-dependent processes such as shocks and variability (Marscher et al. 2008) and does not account for the dynamics of jet launching and acceleration close to the black hole, which require MHD or GRMHD approaches (Mizuno et al. 2015).

1.3 Jet physics

After exploring the different aspects of jets, it is time to dive into the physics involved. In particular, relativistic effects and radiative processes that are inherent to the way we understand AGN jets.

1.3.1 Relativistic effects

The theory of special relativity states that all inertial observers measure the same speed of light in vacuum, regardless of their relative motion. As a consequence, there are two outcomes regarding the relative motion between two objects. Let us consider an inertial system moving with the object (primed), thus seeing it at rest, and another system watching it move (unprimed). Both systems are related by Lorentz transformation, described by the Lorentz factor:

$$\Gamma = \frac{1}{\sqrt{1 - \frac{v^2}{c^2}}} = \frac{1}{\sqrt{1 - \beta^2}}, \text{where } \beta = v/c \tag{1.1}$$

In this scenario, a moving object's length (measuring Δx in the rest frame) appears to be shorter along the direction of motion. This effect is called length contraction: $\Delta x = \Delta x'/\Gamma$ On the other side, there is time dilation, which refers to the slowing of time for an object moving relative to an observer. This implies that a moving clock is perceived to tick slower as seen by a stationary observer ($\Delta t = \Gamma \Delta t'$).

1.3.1.1 Aberration of light

Let us now see how this is of importance to AGNs. As a natural consequence of this relativistic effect, there exists an apparent shift in the direction of observed light due to the motion of the observer relative to the light source. This geometric effect is called *light aberration*. The transformation between both inertial systems are given by (Rybicki & Lightman 1979; Ghisellini 2013):

$$\sin\theta = \frac{\sin\theta'}{\Gamma(1 + \beta\cos\theta')}, \quad \cos\theta = \frac{\cos\theta' + \beta}{1 + \beta\cos\theta'}. \tag{1.2}$$

In the case of relativistic electrons, almost half of the emitted radiation is concentrated in a cone of semi aperture $1/\Gamma$, as shown previously.

1.3.1.2 Doppler boosting

Doppler boosting is a relativistic effect describing how emission from a moving source is enhanced or dimmed to the observer due to relativistic motion. The frequency of the emitted radiation is ν', which due to relativistic time dilation, will be redshifted by a factor of $1/\Gamma$. In addition, the Doppler effect will cause a shift in frequency by a factor of $(1 - \beta\cos\theta)^{-1}$. This means that the observed

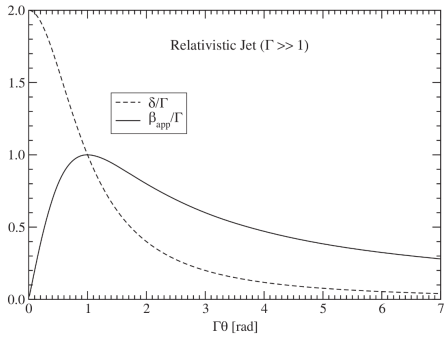

Figure 1.9: Dependence of the apparent transverse speed and the Doppler factor on the viewing angle θ for highly relativistic motion ($\Gamma >> 1$).

frequency ν is higher (blue-shifted) when the source moves toward the observer and lower (red-shifted) when moving away.

By applying both effects, the frequency in the observer's reference frame is:

$$\nu = \nu' \frac{1}{\Gamma} \frac{1}{1 - \beta \cos\theta} = \delta\nu' \tag{1.3}$$

where δ is the Doppler factor, a quantity that relates the rest frame of the source and the observer's frame, taking into account both special relativistic effects and the direction of the source's motion relative to the observer (Contopoulos et al. 2015).

In this context, the observed intensity can be derived from the transformation of the specific intensity between the rest frame of the source and the observer's frame. The specific intensity I_ν (energy per unit time, area A, solid angle Ω, and frequency):

$$I_\nu = \frac{dE}{dt\, d\nu\, dA\, d\Omega} = \frac{h\nu dN}{dt\, d\nu\, dA\, d\Omega} \tag{1.4}$$

Applying the Lorentz transformations:

$$I_\nu = \frac{h(\delta\nu')dN'}{(dt'/\delta)(\delta d\nu')(dA')(d\Omega'/\delta^2)} \tag{1.5}$$

where dN and dA are Lorentz invariant, and $d\Omega = d\Omega'/\delta^2$. This expression can be simplified to:

$$I_\nu = \delta^3 I'_{\nu'} \tag{1.6}$$

This effect is the reason why blazars, with a relativistic jet nearly aligned with our line-of-sight ($\theta \sim 0°$, $\beta \sim 1$), appear much brighter to the observer. Here, $\beta \sim 1$ reflects the fact that jets in radio-loud AGN typically reach relativistic speeds, with bulk Lorentz factors (Γ) ranging from a few up to 10-20, as inferred from apparent superluminal motions and variability studies. This effect is also the same principle explaining why counter-jets, pointing away from the observer, are often undetectable in VLBI images.

For highly relativistic motion ($\Gamma >> 1$), the apparent transverse speed $\beta_{\perp,\mathrm{app}}$ and the Doppler factor δ depend essentially only on the combination $\Gamma\,\theta$. This is illustrated in Fig. 1.9, which shows that the maximum apparent speed occurs at $\Gamma\,\theta = 1$, and the maximum Doppler factor (for $\theta = 0$) is 2Γ.

1.3.1.3 Superluminal motion

In 1969, an apparently faster-than-light motion (projected on the plane of the sky) was first observed at the blazar 3C 273 (Gubbay et al. 1969) using VLBI observations, the only technique able to achieve the necessary angular resolution. This peculiar phenomenon, already predicted in 1966 by Martin Rees (Rees 1966), not only proved not to contradict special relativity, but was also often found in blazar and bright regions of jets usually known as *components* (see for example Gómez et al. 2000).

A schematic description is shown in Figure 1.10. Let us consider a jet oriented an angle θ with respect to the observer's line-of-sight and a component traveling within the jet at a relativistic speed v. The distance travelled by the jet component between two times t1 and t2 (Δt_e) is $v\Delta t_e$. During this distance, the component emits a pulse of light in t1, covering a distance $c\Delta t_e$. At the time the second light pulse is emitted (t2), the component has travelled the projected distance in the observer direction: $v\Delta t_e cos\theta$. That is to say, the pulse emitted in t2 travels a shorter distance to reach the observer. As a result, the time interval measured by the observer is shorter than the real time interval between the pulses as measured in the observer's frame: $\Delta t_e(1 - \beta cos\theta)$

Thus, the apparent velocity of the component projected in the plane of the sky is:

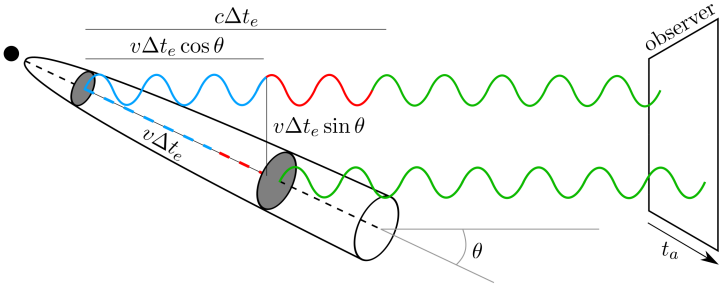

Figure 1.10: Schematic figure of a superluminal component traveling down the jet. The component emits a photon and then travels a distance $v\Delta t_e$ before emitting another photon. A jet oriented close to the line of sight will measure a time interval between the two pulses significantly smaller than the real interval $v\Delta t_a < v\Delta t_e$. This effect can lead to apparent superluminal motions. Credit: A. Fuentes (Fernández 2023).

$$v_{app} = \frac{v\Delta t_e \sin\theta}{\Delta t_e(1 - \beta\cos\theta)} \tag{1.7}$$

Also expressed as:

$$\beta_{app} = \frac{\beta \sin\theta}{1 - \beta\cos\theta} \tag{1.8}$$

Along these lines, the projected velocity measured in the sky plane can be greater than the light speed, i.e. superluminal, depending on the β and θ values. In AGNs, observations have revealed measurements of jets with extreme velocities, such as $40c$ (e.g., Jorstad et al. 2005b), or more moderate and typical of $10c$ (Gómez et al. 2001; Marscher et al. 2008; Agudo et al. 2011).

1.3.2 Radiative processes

This section is based on the content of (Pacholczyk 1970; Rybicki & Lightman 1979; Ghisellini 2013), aiming to review the main mechanisms responsible for the observed emission of AGN jets: Synchrotron and Inverse Compton processes.

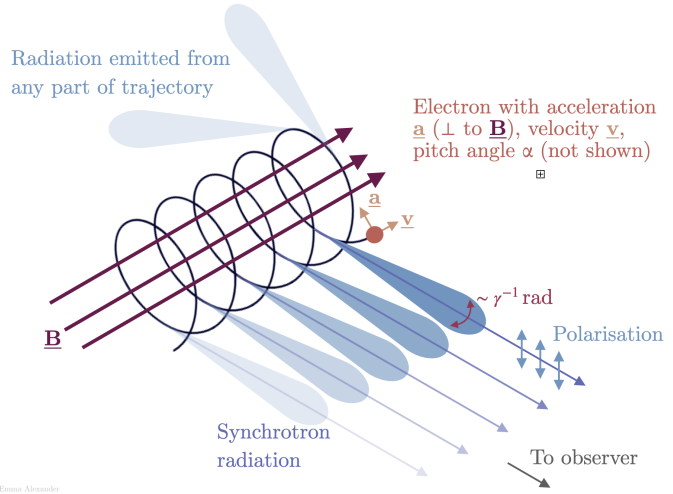

Figure 1.11: Schematic of synchrotron radiation emitted by an electron gyrating in a magnetic field. Credit: Emma L. Alexander, taken from https://emmaalexander.github.io/images/synchrotron.png.

1.3.2.1 Synchrotron Radiation

Relativistic jets emit across the entire electromagnetic spectrum, from radio waves to X-rays and γ-rays. The presence of magnetic fields causes the acceleration (a) of charged particles (q) in the jet, therefore emitting radiation with a power specified by the Larmor's formula:

$$P = \frac{2}{3}\frac{q^2 a^2}{c^3} \tag{1.9}$$

Electrons (e), being the lightest particles, are accelerated more than any other massive ones and so they account roughly for all the radiation observed. This radiation can be classified depending on the speed of the electrons into gyro radiation (from electrons whose velocities are much smaller than the speed of light), cyclotron radiation (from mildly relativistic electrons) and *synchrotron radiation* (relativistic electrons). The latter conforms the main emission for radio AGN jets, making them synchrotron sources. The relativistic electrons have power-law distributions, so they are not in local thermodynamic equilibrium (LTE), and are often called nonthermal sources. Synchrotron radiation is then electromagnetic radiation emitted when charged particles, mostly electrons, travel at relativistic

speeds through magnetic fields (see Figure 1.11). As they move through the magnetic field, these charged particles follow helical paths due to the Lorentz force, causing them to accelerate, and thus to emit radiation (Pacholczyk 1970).

Using primed coordinates describing the inertial frame in which the moving electron is at rest and unprimed for an observer at rest. Larmor's equation gives the radiated power in the electron rest frame as

$$P' = \frac{2(e')^2(a'_\perp)^2}{3c^3} = \frac{2e^2(a_\perp)^2\Gamma^4}{3c^3} = P, \tag{1.10}$$

where $e = e'$ is a relativistic invariant and the magnetic acceleration in the frame of the observer can be derived as $a_\perp = (a_y^2 + a_z^2)^{1/2}$ and $a_i = a'_i/\Gamma^2$ for $i = y, z$. And since the power is also an invariant $P = dE/dt = P'$. An electron moving in a magnetic field is only affected by the Lorentz force:

$$F_L = \frac{d}{dt}(\Gamma m_e \vec{v}) = \frac{e}{c}\vec{v} \times \vec{B} = \frac{e}{c} v B sin\alpha \tag{1.11}$$

where α is called the pitch angle, between the electron velocity (v) and magnetic field (B). From the vectorial product, we can infer than both the acting force and its acceleration are perpendicular to the magnetic field lines:

$$a_\perp = \frac{eBvsin\alpha}{\Gamma m_e c} \tag{1.12}$$

Substituting in Equation 1.2, and considering $v \sim c$, we have the power radiated by a single electron subject to the Lorentz force moving with a pitch angle α:

$$P = \frac{2e^2}{3c^3}\Gamma^2 \left(\frac{eBvsin\alpha}{m_e c}\right)^2, \tag{1.13}$$

which can be simplified by using the Thomson scattering cross section (σ_T) and magnetic energy density ($U_B = B^2/8\pi$):

$$P = 2\, c\, \sigma_T\, U_B\, (\beta\, \Gamma\, \sin\alpha)^2 \tag{1.14}$$

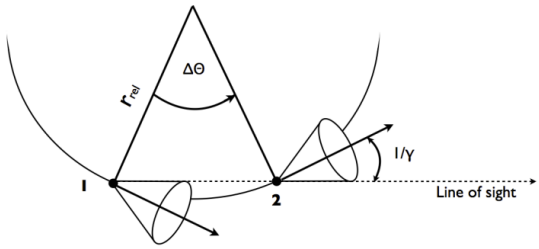

Figure 1.12: Schematic representation of beaming.

Due to the electron's relativistic speeds, their emitted radiation is not isotropic in the observer's frame. Instead, due to relativistic beaming (or light aberration, see previous section), the radiation is confined within a narrow cone of half-opening angle $\theta \sim 1/\Gamma$. This effect arises because, even though in the electron's rest frame the radiation is symmetric, in the observer's frame the relativistic Doppler effect compresses the electron emission into pulses, enhancing the observed intensity along the observer's line of sight (see Figure 1.12 for a schematic representation). This means that the observer only sees the emission within the aperture of a cone $\Delta\theta = 2/\Gamma$, during which the electron travels from point 1 to point 2 a distance $\Delta l \sim \Delta\theta\, r$ and taking a time $\tau = \Delta t_2 - \Delta t_1 = \Delta\theta\, r \left(\frac{1}{v} - \frac{1}{c}\right)$. In any source, a vast number of electrons will be involved, and thus this discrete time will not affect the continuity of the observed emission. Moreover, the spectral distribution of the radiation is mainly distributed around a critical frequency ($\upsilon_c \sim 1/\tau$).

On the same line, in any emitting plasma the propagation of radiation is governed by the radiative transfer equation:

$$\frac{dI_\nu}{ds} = j_\nu - \rho_\nu I_\nu, \tag{1.15}$$

where dI_ν is the specific intensity at frequency ν, j_ν is the emission coefficient (energy emitted per unit volume, frequency, and solid angle), and ρ_ν is the absorption coefficient. The optical depth is defined as:

$$\tau_\nu = \int \rho_\nu ds. \tag{1.16}$$

Until now, we have only considered one single electron. If we contemplate a

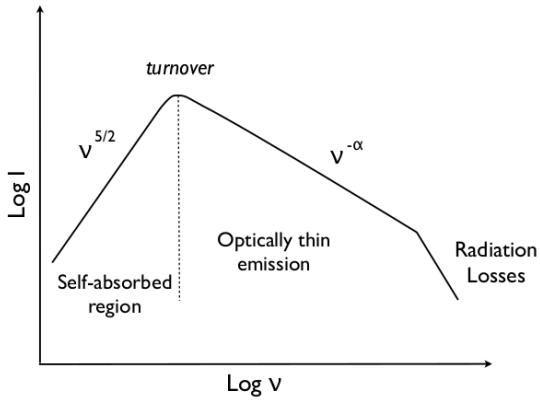

Figure 1.13: Plot representing a partially self-absorbed source.

group of electrons, then based on observed spectra we can assume the energy distribution to follow a power law:

$$N(E)dE \propto E^{-p}dE \qquad (E_{min} \leq E \leq E_{max}) \tag{1.17}$$

where $N(E)dE$ is the number of particles per unit of volume with energies between E and $E + dE$, and p is the exponent of the power law.

Since the population of relativistic electrons follows a power-law energy distribution, the resulting synchrotron emission in the optically thin regime also follows a power-law in frequency.

$$S_\nu \propto \nu^{-\alpha}, \tag{1.18}$$

where α is the spectral index.

Depending on the optical depth, two different regimes arise:

- **Optically thin regime**: In this case, most of the emitted radiation escapes without being absorbed. The specific intensity follows:

$$I_\nu \approx j_\nu s. \tag{1.19}$$

- **Optically thick regime:** When the medium becomes optically thick due to synchrotron self-absorption, radiation is absorbed and re-emitted multiple times, leading to thermalization at lower frequencies. The intensity approaches the source function:

$$I_\nu \approx \frac{j_\nu}{\alpha_\nu} \left(1 - e^{-\tau_\nu}\right). \tag{1.20}$$

  For large optical depths ($\tau_\nu > 1$), this simplifies to:

$$S_\nu \propto \nu^{5/2}. \tag{1.21}$$

This leads to a spectral turnover (see Figure 1.13), where the emission transitions from the optically thick ($S_\nu \propto \nu^{5/2}$) to the optically thin ($S_\nu \propto \nu^{-\alpha}$) regime at a characteristic frequency known as the synchrotron self-absorption frequency $\nu_{\rm SSA}$.

In the case of an homogeneous, optically thin source, and assuming the emission to be isotropic and not absorbed within the source, by integrating $N(E)dE$ times the power emitted by a single electron (Equation 1.14):

$$j_\nu \, d\nu = \int P_s(\nu, E) \, N(E) \, dE \tag{1.22}$$

which represents the synchrotron emissivity of an ensemble of electrons, with j_ν being the specific emissivity (power per unit volume, frequency and steradian). By considering $E_{min} = 0$ and $E_{max} = \infty$, this equation simplifies to (Gomez et al. 1993):

$$j_\nu \propto B^{(p+1)/2} \nu^{(1-p)/2} \tag{1.23}$$

Thus, the spectrum of optically thin synchrotron radiation from a power-law distribution of electrons is also a power law, and the spectral index of synchrotron radiation $\alpha = -d \ln S_\nu / d \ln \nu$ depends only on p:

$$\alpha = \frac{p-1}{2} \tag{1.24}$$

However, if instead of considering an optically thin homogeneous source ($\tau_\nu < 1$), we also consider some absorption, then according to Equation 1.15, the radiation will be partially absorbed in the source, and the specific intensity is reduced by $\rho_\nu I_\nu$. In particular, for an optically thick source ($\tau_\nu > 1$), Equation 1.21 becomes:

$$I_\nu(\tau_\nu) \sim S_\nu \sim j_\nu/\rho_\nu \tag{1.25}$$

In a similar manner as the previous case, it is possible to obtain the value of ρ_ν, finally arriving to the dependence:

$$I_\nu(\tau_\nu) \propto \nu^{5/2} \tag{1.26}$$

Unlike an optically thin source ($I_\nu(\tau_\nu) \propto \nu^{(1-p)/2}$), the specific intensity follows a power law independent of p. A representation of the synchrotron spectrum of a homogeneous partially absorbed source and its frequency dependency for optically thick and optically thin regimes can be found in Figure 1.13. The frequency at which the regime changes is called the *turnover frequency*.

1.3.2.2 Inverse Compton

In addition to synchrotron radiation, the other relevant emission mechanism is the inverse Compton (IC) scattering. In this process, low-energy photons gain energy from the collision with a relativistic electron. During this collision, the photon (radio photon) is upscattered to high energy photon (X-ray or γ-ray photon). This mechanism is the inverse of the classical Compton scattering, in which high-energy photons lose energy upon interacting with electrons.

The inverse Compton process can be described by considering a population of electrons with Lorentz factor $\Gamma \gg 1$ interacting with a photon field of energy E_{photon}. In the electron rest frame, the incident photon is blueshifted due to the Doppler effect, and after scattering, it is re-emitted with a higher energy. When transformed back to the observer frame, the photon energy can be boosted by a factor of approximately $\sim \Gamma^2$ resulting in the aforementioned significant upscattering of soft photons into X-ray or gamma-ray energies.

The power radiated by a single electron undergoing inverse Compton scattering is given by:

$$P_{\text{IC}} = \frac{4}{3}\sigma_T c \Gamma^2 \beta^2 U_{photon} \tag{1.27}$$

where U_{photon} is the energy density of the target photon field. The efficiency of the IC process depends strongly on the energy of the seed photons and the energy distribution of the electron population. Two primary regimes characterize inverse Compton scattering: the Thomson regime, in which the photon energy in the electron rest frame is much smaller than the electron rest mass energy ($E'_{photon} \ll m_e c^2$), and the Klein-Nishina regime, in which this condition is violated and quantum effects become significant. In the Klein-Nishina regime, the cross-section decreases with increasing photon energy, which leads to a suppression of high-energy IC scattering.

In many astrophysical environments, the inverse Compton process occurs in conjunction with synchrotron radiation, as both are driven by the same population of relativistic electrons. This leads to the so-called synchrotron self-Compton (SSC) scenario, where the seed photons for IC scattering are the synchrotron photons produced locally by the electrons themselves.

An important consequence of the inverse Compton effect in radio astronomy is the theoretical upper limit it imposes on the brightness temperature T_b of synchrotron-emitting sources. This is known as the inverse Compton limit, typically around $T_b \sim 10^{12}$ K. In this regime, the energy transfer to the photon field and upscattering the synchrotron photons to higher energies results in substantial radiative cooling of the electron population. This process limits the maximum sustainable brightness temperature, since further increases in T_b would lead to catastrophic energy losses via IC scattering. Observations of brightness temperatures exceeding this limit are often derived from VLBI observations and typically interpreted as evidence for relativistic beaming, where Doppler boosting artificially enhances the observed brightness temperature while its intrinsic value remains below the IC limit.

1.4 Radio Interferometry: A peek into the innermost region of AGN jets

The radio sky began to unfold before scientists' eyes in the 1930s with Carl Jansky's discovery of extraterrestrial radio emission. Since then, the universe has continued to reveal an astonishing diversity of objects and phenomena through radio observations.

The reason why radio emission is so crucial in astronomy is that, like optical waves, radio waves can penetrate Earth's atmosphere, making ground-based observations possible. The scientific demands of radio astronomy, coupled with technological advancements, have continuously pushed the boundaries of resolution

and sensitivity. For instance, achieving high resolution is quite a challenge, and requires the development of new techniques.

In the following sections, we will introduce the fundamental concepts of radio interferometry, together with the explanation on the currently most successful techniques that are able to achieve high-resolution imaging, and the process by which the radio telescopes' signal turns into images.

1.4.1 General concepts

Let us begin with some general notions and terms commonly used in radio interferometry.

We can define interferometry as a family of techniques in which electromagnetic waves from multiple telescopes are combined to produce interference patterns. In this way, each individual telescope (also referred to as antenna or station from now on) acts as an interferometer that creates interference patterns when signals from different telescopes are combined, similarly to Young's slit experiment. This allows astronomers to extract spatial information about celestial sources that would otherwise be unresolvable with a single dish.

The angular resolution (θ) of a telescope determines its ability to distinguish fine details and is given by the expression:

$$\theta = \frac{1.22\lambda}{\mathrm{D}} \tag{1.28}$$

where λ is the observed wavelength and D is the telescope's diameter. From this, it is easy to derive that higher spatial resolution requires a larger sized telescope for a given wavelength. For example, achieving an angular resolution of 1 arcsecond at a wavelength of 22 cm would require a telescope with a diameter of approximately 45.4 km, which is impractical.

The solution to this technical limitation came with the development of aperture synthesis, a technique pioneered by Martin Ryle and colleagues (Ryle & Vonberg 1946; Ryle & Hewish 1960), which earned the first Nobel Prize in astronomy in 1974. Aperture synthesis allows astronomers to reconstruct high-resolution images by combining signals from multiple telescopes at different locations and times. Very Long Baseline Interferometry (VLBI) represents the most extreme application of this technique, as we will see in Section 1.4.2. This way, if we define baseline as the distance between two telescopes, in Equation 1.28, D becomes the largest baseline length. Therefore, a number of telescopes separated by thousands

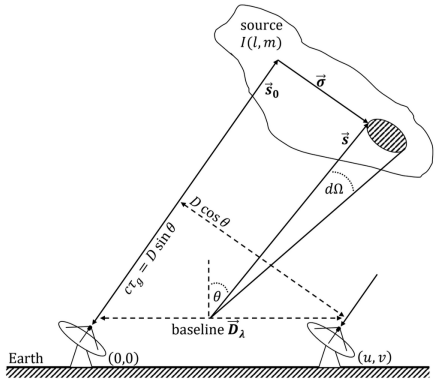

Figure 1.14: Example of a two-array interferometer. Credit: Jan Röder, taken from urn:nbn:de:hbz:38-736755

.

of kilometers all over the globe can achieve a combined resolution superior to any single instrument, synthesizing a virtual Earth-sized telescope.

Each pair of telescopes provides data points in what we call the uv-plane, which is a Fourier space where each point represents a baseline. In practice, the u and v coordinates are the baseline lengths, projected in a perpendicular plane to the line of sight and in units of the observed wavelength. That is to say, they define a tangential plane to the Earth's surface, u and v representing the directions East-West and North-South, respectively.

The measurements taken by any pair of radio stations (interferometer) are called visibilities, and the principle that enables us to translate these data into images is the Van-Cittert-Zernike theorem (Van Cittert 1934; Zernike 1938), which states that these visibilities correspond to the Fourier transform of the sky brightness distribution. Mathematically, this can be expressed as:

$$V(u,v) = \int\int I(l,m) e^{-2\pi i(ul+vm)}\, dl\, dm \tag{1.29}$$

where $V(u,v)$ is the visibility function (taken measurements), $I(l,m)$ is the brightness distribution of the sky (the actual image), and l and m are the direction cosines of the source relative to the center of the image.

As a result, in theory it is possible to recover an image from the observed object by performing an inverse Fourier transform of the measurements from our telescope array. Of course, this would require a perfect sampling of the Fourier space (uv-plane).

However, every pair of antennas can only sample a spatial frequency (uv-point) at a given time, growing in number as $n(n-1)/2$, being n the number of telescopes. That is to say, we only end up with a finite number of data points, and therefore numerous different plausible images that could fit them. This ill-posed problem is especially challenging for sparse arrays, since the robustness of the final image is dependent on a good coverage of the uv-plane. A way to maximize the information is to let the Earth rotate (Earth aperture synthesis) during the observation, thus sampling additional visibilities and filling the (u,v) plane. This strategy assumes the source remains stationary during the observations.

For a more detailed view on interferometry and synthesis, we direct the readers to one of the bibles on the field: Thompson et al. (2017).

1.4.2 Very Long Baseline Interferometry technique

Radio interferometry rather assumes that the telescopes conforming the interferometer are physically connected. This can be the case of facilities such as the Very Large Array (VLA) or the Atacama Large Millimeter/submillimeter Array (ALMA), where antennas are linked by fiber-optic cables. However, achieving higher angular resolution requires a different approach.

The development of the technique Very Long Baseline Interferometry (VLBI), consists of having radio telescopes separated (and disconnected) by thousands of kilometers, operating as a single, Earth-sized instrument. These VLBI stations do not share signals in real time, but rather independently save their own timestamps with extremely precise hydrogen maser atomic clocks.

For some space-based VLBI missions, communication and data relay rely on satellite relay systems like the Tracking and Data Relay Satellite System (TDRSS), which NASA uses to maintain near-continuous telemetry links with orbiting instruments, enabling efficient data transmission and coordination between Earth and space telescopes.

The recorded signals are later brought together at a central facility, known as the correlator, which cross-multiplies signals from different telescopes to produce interference fringes, encoding both complex visibilities and phase information.

Nowadays, there are several operating global VLBI networks. Among them, we highlight the most relevant to this work:

- **The Very Long Baseline Array (VLBA)**, with 10 identical radio telescopes spread across the United States.
- **The European VLBI Network (EVN) and the East Asian VLBI Network (EAVN)**, with 22 and 21 antennas, respectively, across Europe and Asia.
- **The Global Millimeter VLBI Array (GMVA)**, with 15 radio telescopes across Europe and the United States, designed for high-frequency (86 GHz) VLBI.
- **The Event Horizon Telescope (EHT)**, of currently 11 stations, which achieves an angular resolution of ∼20 microarseconds at millimeter and sub-millimeter wavelengths and is able to provide the first images of supermassive black holes.

Beyond Earth-based VLBI, even longer baselines can be achieved using space-based telescopes. The *VLBI Space Observatory Programme (VSOP)* (1997-2005) was the first to launch an antenna, known as HALCA (Highly Advanced Laboratory for Communications and Astronomy), in Earth's orbit, and work alongside ground-based antennas (Hirabayashi et al. 1998).

More recently, the *RadioAstron* mision (Kardashev et al. 2013) (2011-2019) extended baselines up to 350,000 km, allowing for radio observations with resolutions on the order of tens of microarcseconds at centimeter wavelengths (Lobanov et al. 2015; Gómez et al. 2016; Giovannini et al. 2018; Vega-García et al. 2020; Kovalev et al. 2016; Bruni et al. 2021; Gómez et al. 2022; Savolainen et al. 2023). This program and its results will discussed more in depth in Chapter 4.

In the future, more space missions like *BHEX* (Johnson et al. 2024) will embody the new generation of radio interferometry. *BHEX*, for example, will incorporate a 3.5-meter aperture antenna and be designed to operate at millimeter and sub-millimeter wavelengths. The ambitious aim of this mission is to constrain the spin of black holes and other properties by detecting their photon ring, a narrow, bright ring made of photons that undergo multiple orbits around the black hole before escaping its pull.

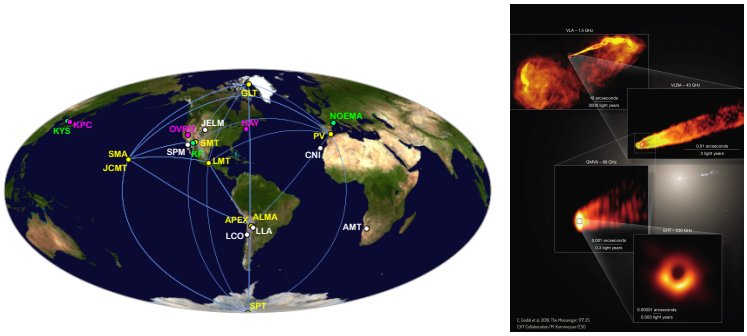

Figure 1.15: EHT array. EHT Collaboration; ALMA (ESO/NAOJ/NRAO), (Goddi et al. 2019); NASA, ESA and the Hubble Heritage Team (STScI/AURA); VLBA (NRAO).

1.4.2.1 From the radiotelescopes to an image

As previously stated, the final goal of VLBI is to combine data from multiple radio telescopes to achieve higher resolution. While this is made possible by the correlator, the output data from this process is raw and requires several steps and extensive processing before it can be ready for imaging. This is because the recorded signals are affected by various instrumental and environmental effects such as system temperature variations, antenna gain uncertainties, atmospheric opacity that introduce errors in both amplitude and phase. Therefore, calibrating the data carefuly is necessary to correct for these effects before the data can be reliably interpreted.

A Priori Amplitude Calibration The complex process of calibrating the data starts with what it is usually called *a priori amplitude calibration*. Here, the *calibrated* visibility amplitude, $|V_{ij}^{\mathrm{cal}}|$, in Janskys (Jy), is related to the observed amplitude $|V_{ij}^{\mathrm{obs}}|$ by:

$$|V_{ij}^{\mathrm{cal}}| = |g_i|^{-1}|g_j|^{-1}|V_{ij}^{\mathrm{obs}}| \tag{1.30}$$

which, in terms of telescope parameters, can be rewritten as:

$$|V_{ij}^{\mathrm{cal}}| = \sqrt{\frac{T_{\mathrm{sys},i}}{\mathrm{DPFU}_i \cdot \eta_{\mathrm{el},i}}} \cdot \sqrt{\frac{T_{\mathrm{sys},j}}{\mathrm{DPFU}_j \cdot \eta_{\mathrm{el},j}}} |V_{ij}^{\mathrm{obs}}| \tag{1.31}$$

where $T_{\rm sys}$ is the system temperature (corrected for atmospheric opacity), DPFU (Degrees Per Flux Unit) converts antenna temperature (K) to flux density (Jy), and $\eta_{\rm el}$ is the elevation-dependent gain curve.

These values are typically provided by the VLBI telescopes. However, a wide range of factors can introduce errors in the observed signals, including both instrumental effects (e.g., receiver noise, digitization errors, clock instabilities, antenna pointing errors) and environmental influences (e.g., atmospheric turbulence or opacity). These effects impact both the amplitude and the phase of the visibilities. As a consequence, the antenna-based gain terms (gigi and gjgj) are, in general, complex quantities that correct for amplitude and phase changes. Nonetheless, some imaging methods, such as *Regularized Maximum Likelihood (RML) algorithms*, incorporate strategies to mitigate the impact of calibration uncertainties, for example by relying on closure quantities that are free of station-based errors (see Section 1.4.3 for more detail).

In VLBI, the data collected from each station has very precise timestamps, but frequency offsets can remain due to instrumental and geometric factors. The Earth's rotation model used in the correlator is not perfect, so residual errors in delay and fringe rate (frequency) still remain after initial correlation. These cause the fringes to drift over time. To correct for these effects, a two-dimensional search over delay and fringe frequency (or delay rate) is performed to maximize the correlation function; a process known as fringe fitting (Schwab & Cotton 1983).

This method references all visibility phases to a common station (typically the most sensitive one) assuming its delay, rate, and phase are zero. Initially, a simple point-source model is assumed, which has been shown to be sufficiently accurate for correcting phase errors, even when the true source structure is more complex. The most commonly used AIPS task for fringe fitting is `FRING`, which performs a least-mean-square fit to optimize the unknown parameters.

In particular, for VLBI observations including a space station, this fringe-fitting process usually takes two steps: a first ground-only fringe fitting, obtaining solutions only for the ground-based stations, and then using the calibrated ground array to determine the delay, rate, and phase for the space radio telescope through baseline stacking (further details in Chapter 4).

However, despite this correction, residual amplitude and phase errors often remain due to imperfections in the array model. Because of these errors, techniques like time and frequency averaging, which could improve the signal-to-noise ratio or direct image reconstruction, are not recommended at this stage.

Instead, after correlation, the measured visibility on a baseline between antennas i and j, denoted as V_{ij}, is expressed as:

$$V_{ij} = g_i g_j^* V_{ij}^{\text{true}} + \varepsilon_{ij} = |g_i||g_j^*|e^{(\phi_i - \phi_j)} V_{ij}^{\text{true}} + \varepsilon_{i,j} \tag{1.32}$$

where g_i and g_j are the complex gains, representing the gain amplitude and phase of each station, ϕ_i and ϕ_j are the station-based phase errors, and ε_{ij} accounts for thermal noise. The measured and true visibility phases of a baseline i, j are related by:

$$\phi_{ij}^{\text{measured}} = \phi_{ij}^{\text{true}} + \phi_i - \phi_j \tag{1.33}$$

These errors vary with time and frequency, leading to additional parameters, such as the fringe rate (r_{ij}) and delay (τ_{ij}):

$$r_{ij} = \frac{\delta \phi_{ij}^{\text{measured}}}{\delta t}, \quad \tau_{ij} = \frac{\delta \phi_{ij}^{\text{measured}}}{\delta \nu} \tag{1.34}$$

Since both amplitude and phase errors can significantly affect the observed visibilities, it is useful to consider observables that are inherently robust to these calibration errors, such as closure quantities, and in particular, closure phases and closure amplitudes. These quantities are particularly valuable in the imaging process because they are unaffected by station-based complex gain errors.

A closure phase is defined as the sum of the visibility phases along a closed triangle of baselines formed by three antennas i, j, and k, and by using Equation 1.33:

$$\begin{aligned}
\phi_{c,ijk} &= \phi_{ij}^{\text{measured}} + \phi_{jk}^{\text{measured}} + \phi_{ki}^{\text{measured}} && (1.35)\\
&= \phi_{ij}^{\text{true}} + \phi_i - \phi_j + \phi_{jk}^{\text{true}} + \phi_j - \phi_k + \phi_{ki}^{\text{true}} + \phi_k - \phi_i && (1.36)\\
&= \phi_{ij}^{\text{true}} + \phi_{jk}^{\text{true}} + \phi_{ki}^{\text{true}}. && (1.37)
\end{aligned}$$

where ϕ_{ij}^{true} is the true visibility phase. Since the station-based gain phases cancel out, closure phases are independent of station-based errors and provide direct information about the intrinsic source structure. The total number of independent closure phases for an array with N antennas is given by: $\frac{(N-1)(N-2)}{2}$

Analogously, the same occurs with closure amplitudes, except forming a quadrangle (i,j,k,l) of baselines, and thus defined as:

$$|V_{\mathrm{c},ijkl}| = \frac{|V_{ij}V_{kl}|}{|V_{ik}V_{jl}|}, \tag{1.38}$$

which using the same strategy as for closure phases, using Equation 1.32 it yields:

$$|V_{\mathrm{c},ijkl}| = \left| \frac{V_{ij}^{\mathrm{true}} V_{kl}^{\mathrm{true}}}{V_{ik}^{\mathrm{true}} V_{jl}^{\mathrm{true}}} \right|. \tag{1.39}$$

Again, all station-based gain terms cancel out, ensuring that closure amplitudes are only sensitive to the intrinsic source structure. The number of independent closure amplitudes for an array with N antennas is: $\frac{N(N-3)}{2}$.

The post-correlation calibration process then involves solving for the station gain amplitudes, phases, fringe rates, and delays to refine the observed visibilities. The standard VLBI calibration procedure is designed to correct these instrumental effects and reconstruct the most accurate representation of the true sky visibility.

VLBI Calibration Software Several software packages are widely used in the VLBI community for data calibration:

- **AIPS** (*Astronomical Image Processing System*) (Greisen 2003) is the most widely used software for centimeter-wavelength VLBI. Developed at the National Radio Astronomy Observatory (NRAO), it provides a suite of tasks designed for VLBI data calibration, imaging, and analysis. AIPS includes tasks such as `FRING` for fringe fitting and `APCAL` for amplitude calibration.
- **CASA** (*Common Astronomy Software Applications*) (McMullin et al. 2007) is a more modern package developed primarily for ALMA and the Very Large Array (VLA). While not originally designed for VLBI, CASA has increasingly been adapted for VLBI data processing.
- **HOPS** (*Haystack Observatory Postprocessing System*) (Blackburn et al. 2019) is specialized software used for processing millimeter-VLBI data, including observations from the Event Horizon Telescope Collaboration.

- **PIMA** (Petrov 2011) is a software package designed for VLBI data calibration, oriented on batch processing of VLBI experiments for absolute astronomy and geodesy applications.

1.4.3 Imaging process

Once the data is calibrated and ready for imaging, there are several strategies to address image reconstruction. As it was previously mentioned, the visibility Fourier domain is not fully sampled by the interferometer, and therefore, the reconstructed images are in need of constraints or assumptions beyond these measurements. For example, some strong constraints are the image positivity or a limited field of view. Moreover, some imaging algorithms can impose or enhance some physically motivated image properties, such as smoothness. This way, imaging algorithms classification can be twofold: *inverse modeling* (e.g. CLEAN) and *forward modeling* (e.g. RML methods).

1.4.3.1 CLEAN

Commonly used for VLBI, it uses an image reconstruction approach implemented in software packages like DIFMAP (Shepherd 1997) and CASA. The algorithm works by applying an inverse Fourier transform to the visibilities, producing a "dirty image", that is, a preliminary representation of the source that includes distortions due to the telescope array's sampling function (dirty beam).

The CLEAN algorithm approximates the true sky brightness distribution by iteratively subtracting point-source components from the dirty image. In each iteration, it identifies the brightest peak, subtracts a scaled version of the dirty beam from that location, and stores it as a CLEAN component. The process is repeated until the residuals reach a pre-defined noise threshold. The final CLEAN components are then convolved with an idealized Gaussian beam and added back to the residuals to produce the reconstructed image.

While CLEAN was traditionally considered a semi-manual process—especially in the context of model-fitting and interactive CLEAN windows—it can be fully automated, and automated pipelines are now routinely used in VLBI surveys and large imaging campaigns.

Moreover, CLEAN is often used in combination with self-calibration, what is known as hybrid imaging. Self-calibration refines the instrumental and atmospheric phase and amplitude gains using the evolving source model, improving consistency between the visibilities and the reconstructed image. Typically, phase self-calibration is applied first, followed by amplitude self-calibration once the

model becomes more constrained. The iterative loop between CLEAN and self-calibration enhances image fidelity and dynamic range, making hybrid imaging a powerful and standard approach in VLBI data reduction.

Despite its limitations, such as its implicit assumption of point-like source structures and potential bias in low-SNR regimes, CLEAN remains the most common imaging method in VLBI, especially at centimeter wavelengths.

1.4.3.2 Regularized Maximum Likelihood Methods

RML methods take a different approach rather than the more classical one in CLEAN. Instead of directly transforming visibilities into an image, they frame the reconstruction as an optimization problem, where an objective function is minimized. The function is expressed as:

$$J(I) = \sum_{\text{data terms}} \alpha_D \chi^2_D(I) - \sum_{\text{regularization terms}} \beta_R S_R(I) \tag{1.40}$$

The first term measures how well the reconstructed image I matches the observed visibilities while the second imposes prior constraints on the image based on predefined assumptions (regularization). That is, by controlling the hyperparameters α_D and β_R, it is possible to control the relative weighting of both the data and regularization terms, respectively. For instance, assigning too much weight on the regularization side may result in an image reconstruction not compatible with the data (i.e. not achieving $\chi^2_D \sim 1$ for all data terms).

Standard regularizers used in VLBI include image entropy, smoothness or sparsity of the image (Narayan & Nityananda 1986; Chael et al. 2016a; Akiyama et al. 2017a), among others. For the remaining of this thesis, the RML method use will be the software package `eht-imaging`, which has been developed and tested within the EHT Collaboration. It is important to note that even when the choice of regularizers is a substantial factor, other aspects such as data preparation or the selected field of view can be also just as important in the final image reconstruction. A further discussion on the imaging process with `eht-imaging` and RML methods can be found in Chapter 4.

One of the main advantages of the RML methods is that, unlike CLEAN, they can naturally incorporate both full complex visibilities and closure quantities. The latter are a data product derived from the interferometric visibilities.

This makes RML particularly useful when dealing with data affected by phase

corruption, avoiding the need for self-calibration that CLEAN requires. However, it is also possible to perform self-calibration, and particularly, iteratively together with imaging steps, until reaching convergence and best minimizing Equation 1.40.

In `eht-imaging`, the minimization in imaging takes place via gradient descent algorithms, which risks falling into local minima. The standard way to avoid this and better sample the solution space is to initialize each iteration with a blurred version of the last image reconstruction from the previous cycle. Alternatively, a good way to ensure the consistency of the final image is to perform a parameter survey, sampling a subspace of different data and regularizers weights. These methods can often achieve some degree of super resolution (i.e. finer than the nominal diffraction limit, $\theta \sim |(u,v)|_{max}$).

Since RML approaches can work directly with closure quantities, self-calibration is less critical compared to CLEAN. In this context, self-calibration refers to updating the antenna-based complex gains based on the current image model. These updated gains are used to refine the data and are then usually followed by another imaging step. While RML methods can be used with only closure quantities, combining them with self-calibration loops can significantly improve image fidelity. This iterative process is particularly useful in hybrid pipelines that begin with closure-only reconstructions to avoid station-based errors and later incorporate complex calibrated visibilities once a reliable model has been established.

So far, the imaging process from Earth rotation synthesis observations is based on the assumption that the observed object's brightness distribution is static and does not change during said observation. This fact, while mostly true for the majority of VLBI targets, is not always the case. For example, sources like Sagittarius A* (Sgr A*) challenge this assumption by showing variability on minute timescales (Event Horizon Telescope Collaboration et al. 2022a). The addition of this intrinsic variability to the imaging process poses a great difficulty; the two main approaches to deal with this are: either the inflation of the data's error budget to take into account the fluctuations, and thus producing a mean static image, or the reconstruction of a movie with multiple frames that capture the source's changing brightness (Event Horizon Telescope Collaboration et al. 2022c).

Recent developments in imaging reconstruction, also driven by the need to capture the black hole dynamic environment (BDE), have led to the emergence of novel approaches such as open-source Bayesian-based algorithms -like Comrade.jl (Tiede 2022) or resolve (Junklewitz, H. et al. 2016)-, and neural networks like Kine (Foschi et al., submitted). These new tools have the potential to offer new

insights in black hole physics.

Chapter 2

Dynamic imaging of supermassive black holes using Multimodality Algorithms

In this chapter, we start by exploring the very core of the AGN: the supermassive black hole. Using the imaging background described in the previous section, we can now introduce a multimodality algorithm, whose strategy aims to capture the dynamics of the black hole both in total intensity and polarization. The results of this study will be presented in an upcoming publication.

2.1 Introduction

Supermassive black holes are found at the centre of most galaxies, where accretion drives regularly observed periods of activity that influence both their host galaxies and surrounding environments. SMBHs also serve as laboratories for studying gravity. However, only M87* and Sgr A*, at the centre of our galaxy, have been resolved on event-horizon scales. Understanding Sgr A*has been a major focus, with long-term monitoring campaigns (Do et al. 2019; GRAVITY Collaboration et al. 2019; Reid & Brunthaler 2020) and high-resolution radio studies (e.g. Falcke et al. 1998; Krichbaum et al. 1998; Bower et al. 2004; Doeleman et al. 2008; Lu et al. 2018). As introduced in the previous chapter, the EHT is a VLBI international collaboration mainly focused on observing the event horizons of supermassive black holes. Among its many achievements, this collaboration managed to successfully image the innermost region our own Galaxy in both total intensity (Event Horizon Telescope Collaboration et al. 2022a,b,c,d,e,f) and polarization (Event Horizon Telescope Collaboration et al. 2024b,d), revealing

a ring-like structure consistent with the predicted shadow of a black hole. The accompanying theoretical interpretation of these observations, consistent with a magnetically arrested disk model (Event Horizon Telescope Collaboration et al. 2022e,f, 2024d), have had a major impact on the study of the physical properties of this source.

While the EHT's static images offer crucial insights on supermassive black hole physics and their extreme environments, Sgr A*is likely to be a highly dynamic and turbulent system. Recent studies have started to explore variability, for example in M87, which shows changes on annual timescales (Wielgus et al. 2020; Event Horizon Telescope Collaboration et al. 2024e) and Sgr A*, varying over minutes to hours (Bower et al. 2015; GRAVITY Collaboration et al. 2018; Event Horizon Telescope Collaboration et al. 2022c; Wielgus et al. 2022; Farah et al. 2022) due to the smaller mass than M87*. For Sgr A*, the innermost stable circular orbit (ISCO) is estimated to complete a cycle in about 30 minutes (GRAVITY Collaboration et al. 2018), making it possible to capture its dynamics within a day. Combining such dynamic imaging with observations of flaring activity across different wavelengths, like those recorded during the observations on April 11 in 2017 of Sgr A*, has the potential to become a new scientific milestone as well as significantly advance our understanding of these systems (Johnson et al. 2017).

Capturing a time-resolved reconstruction, or movie, of the dynamic behavior of a supermassive black hole using the EHT is a complex challenge. Sparse sampling of VLBI arrays in the Fourier domain complicates the reconstruction of images, while short phase-coherence times at 230 GHz result in phase loss. Traditional VLBI imaging assumes a static source, but the rapid variability of Sgr A*demands the development of novel algorithms and imaging techniques that integrate time-domain information. This variability also complicates the separation of calibration errors from intrinsic dynamics, making it essential to rely on closure properties to reconstruct the time-evolving image. The process introduces complex multimodal posteriors, as demonstrated by Mus et al. (2024b). Thus, creating a time-resolved movie requires addressing sparse data, gain uncertainties, rapid variability, scattering, and polarimetric reconstruction, making it currently one of the most intricate problems in VLBI imaging.

The EHT has developed a wide variety of techniques for dynamic imaging to overcome these issues, i.e. time-dynamic reconstructions (Bouman et al. 2017; Müller & Lobanov 2023; Mus & Martí-Vidal 2024; Mus et al. 2024b,a; Foschi et al. 2025), (polarimetric) reconstructions from calibration independent closure quantities (Chael et al. 2018b; Blackburn et al. 2020; Müller & Lobanov 2022; Müller et al. 2023; Albentosa-Ruiz & Marti-Vidal 2023; Müller 2024), or the simultaneous reconstruction of the scattering screen (Mus et al. 2025). To ensure

robustness on the results, the EHT follows a rigorous validation strategy, analyzing data with multiple algorithms, each with distinct assumptions and approximations, and validating against extensive synthetic data sets, in a similar way as previously done for the static imaging of M87 (Event Horizon Telescope Collaboration et al. 2019a) and Sgr A*(Event Horizon Telescope Collaboration et al. 2022a).

Currently, five algorithms can handle Sgr A*data in full polarization and account for its dynamics: the compressive sensing method `Dog-Hit` (Müller & Lobanov 2022), the Regularized Maximum Likelihood (RML) algorithms `eht-imaging` (Chael et al. 2016b, 2018b), `MOEA/D` and its variant `MO-PSO` (Müller et al. 2023; Mus et al. 2024b,a), the neural network `kine` (Fuentes et al. 2025), and the Bayesian tool `resolve` (Junklewitz et al. 2016; Arras et al. 2021). All five were equally tested and validated in this project to achieve an unbiased, robust result for Sgr A*.

RML techniques have been used in all major black hole imaging campaigns performed by the EHT (Event Horizon Telescope Collaboration et al. 2019d; Kim et al. 2020b; Event Horizon Telescope Collaboration et al. 2021; Issaoun et al. 2022; Event Horizon Telescope Collaboration et al. 2022c, 2023; Jorstad et al. 2023; Event Horizon Telescope Collaboration et al. 2024e,b). They are as well widely studied outside of this collaboration, essentially already dating decades back to the maximum entropy algorithm (Cornwell & Evans 1985; Narayan & Nityananda 1986; Briggs 1995; Chael et al. 2016b; Akiyama et al. 2017c,b; Chael et al. 2018b; Moriyama et al. 2022; Müller et al. 2024). To avoid traditional parameter surveys used in previous EHT works (e.g. Event Horizon Telescope Collaboration et al. 2019d, 2022c), `MOEA/D` applies a data-driven, multi-objective optimization inspired by game theory to find optimal hyperparameters without relying on synthetic tests (Müller et al. 2023; Mus et al. 2024b). `MO-PSO` is a faster numerical alternative working in the same framework, trading numerical speed for a more global exploration (Mus et al. 2024a).

Within the ongoing EHT dynamic imaging project, time correlation is modeled via an entropy functional (ngMEM) (Mus & Martí-Vidal 2024) and multiresolution support inspired by multiscalar spectral imaging pipelines, which was already found effective for time-dynamic reconstructions (Müller & Lobanov 2023). `MOEA/D` searches for the ideal parameter combination for every single data set (defined by some heuristics), finding the ideal balancing between time correlation and data fidelity. Therefore, it technically settles an upper bound for RML-based reconstructions of Sgr A*with simple, straightforward expressions for the correlation in time. Higher abstraction methods like `kine` and `resolve` (discussed in companion papers Foschi (2025); Knollmüller (2025)) aim to surpass RML limitations by inferring time correlations more flexibly from the data.

2.2 The strategy of multimodality

The RML methods are among the most frequently employed imaging techniques in EHT analyses (Event Horizon Telescope Collaboration et al. 2019d, 2021, 2022c, 2023, 2024e,b). They minimize a weighted sum of multiple data fidelity terms and regularization terms, thus optimizing the agreement with observational data and prior regularization constraints. Data fidelity terms, typically χ^2 metrics, ensure a proposed solution is consistent with the observed data products such as visibilities or closure quantities. Regularization terms like total variation (encouraging piecewise smoothness), l^1-norm (fostering sparsity), or entropy-based functionals, however, impose constraints to ensure plausible reconstructions.

This chapter focuses on dynamic, full-polarization movie reconstructions, extending the objective functionals to include polarimetric regularizers such as the polarimetric entropy and total variation (Holdaway & Wardle 1988; Chael et al. 2016b; Mus et al. 2024b). This extension also accounts for time variability by including time-domain entropy (Mus & Martí-Vidal 2024) using the multiresolution support of specially designed wavelets as described in Müller & Lobanov (2022, 2023), similar to approaches to wide-band and spectral imaging for dynamic VLBI data sets (Rau & Cornwell 2011; Offringa & Smirnov 2017).

The correct relative weighting of terms is crucial for the success of RML methods. Traditionally, the EHT has explored a wide range of parameters to achieve this balance. Here, we adopt an alternative approach that reframes the problem based on multi-objective optimization. In this framework, the optimality of a single weighted sum of objectives is replaced by the concept of Pareto optimality (for instance Pardalos et al. 2017). A solution is considered Pareto optimal if improving one objective (e.g., the data fidelity term) necessarily results in the degradation of another objective (e.g., a regularization term). The set of solutions obtained from this process is referred to as the Pareto Front, representing all possible compromises between the objectives.

The multi-objective evolutionary algorithm based on decomposition (`MOEA/D`) (Zhang & Li 2007; Li & Zhang 2009) is designed to approximate the Pareto front in multi-objective optimization problems (Zhang & Li 2007; Li & Zhang 2009). Adapted for VLBI imaging by Müller et al. (2023) and Mus et al. (2024b), it revealed the Pareto Front to be composed of disjoint clusters. These clusters are interpreted as locally optimal modes of the potentially multimodal imaging problem. Notably, the cluster containing the best solution is typically the one nearest to the ideal point, as detailed in Müller et al. (2023). This algorithm has been applied to reconstruct the polarization structure from closure traces (Müller 2024), a potentially dynamic scattering screen simultaneously with the

image (Mus et al. 2025), and solar flare images with the STIX instrument (Müller et al. 2024). Its ability to navigate complex, multimodal landscapes makes it particularly valuable in these challenging contexts.

Multi-objective particle swarm optimization (`MO-PSO`), a faster variant (Mus et al. 2024a) of `MOEA/D`, replaces evolutionary optimization with particle swarm optimization to efficiently navigate the Pareto front. L-BFGS-B* minimization (see for instance Bonnans et al. 2006) then solves the scaled optimization problems, focusing directly on minimizing the distance between a Pareto-optimal solution and the ideal point on the Pareto front. Instead of recovering the entire Pareto front like `MOEA/D`, `MO-PSO` targets the final best image reconstruction, significantly reducing the computational time and resources required. This technique makes it particularly suitable for scenarios demanding both speed and precision in image reconstruction.

It is important to note that `MOEA/D` and `MO-PSO`, rather than rely on classical regularization to model temporal correlations, extending traditional entropy-based functionals in the time domain and transferring concepts from the imaging of spectral channels into the time domain. Thus, they effectively survey hyperparameter combinations to adapt to the data, but remain limited by the prior assumptions encoded in traditional regularizers.

2.2.1 Multiobjective optimization

Both `MOEA/D` and `MO-PSO` are therefore RML-based techniques that use the potential of multi-objective optimization techniques to solve the VLBI imaging problem. That is, given a functional F and a vector x, the multi-objective problem (MOP) seeks to independently minimize the components of F in the way:

Problem 1 (MOP)**.**

$$\begin{aligned} &\textit{min} && F(x) := \left(f_1(x), \ldots, f_n(x)\right), \\ &\textit{subject to} && x \in \mathbf{F} \subseteq \mathbb{R}^{(N+4)P}, \end{aligned} \tag{MOP}$$

where $\mathbf{F}$ is a feasible subset of x. The possible conflicting objectives generate a set of optimal solutions (or Pareto Front).

One common approach to solving Prob. (MOP) is scalarization, which expresses the vector-valued function F as a weighted sum of its components f_i. This yields the following unconstrained minimization problem:

*Limited-memory Broyden–Fletcher–Goldfarb–Shanno algorithm

Data	Type	Obj.	Description	Reference
I	Data	χ^2_{cph}	fit quality to closure phases	1
		χ^2_{lca}	fit log. of closure amplitudes	1
		χ^2_{amp}	fit amplitudes	1
	Reg.	R_{entr}	fit entropy	1
		R_{tv}	fit total variation	1
		R_{tv2}	fit total squared variation	1
		R_{l1}	fit l^1-norm	1
		R_{flux}	fit total flux constraint, extended to lightcurve	1,2
Dynamics	Reg.	$\mathbf{1}_{ms}$	fit constrained to static wavelets	3
		R_{ngMEM}	fit time-entropy	4
Linear polarization (LP)	Data	χ^2_{pvis}	fit quality to LP visibility $\mathcal{P}$	5
		χ^2_{m}	visibility polarimetric ratio $\mathcal{P}/\mathcal{I}$	5
	Reg.	R_{ptv}	total variation of $P = Q + iU$	5
		R_{ms}	entropy of $P = Q + iU$	5
		R_{hw+cp}	HW-entropy of total pol. fraction $m + v$	this work
Circular polarization (CP)	Data	χ^2_{cvis}	fit quality to CP visibility $\mathcal{V}$	6
	Reg.	R_{hw+cp}	HW-entropy of total pol. fraction linear and circular $(m + v)$	this work
Scattering	Reg.	R_{scat}	l^2-norm of scattering screen	7

Table 2.1: Data and Regularization terms used for `MOEA/D` and `MO-PSO`. **References.** 1: Event Horizon Telescope Collaboration et al. (2019d), 2: Event Horizon Telescope Collaboration et al. (2022c), 3: Müller & Lobanov (2023), 4: Mus & Martí-Vidal (2024), 5: (Chael et al. 2016b), 6: Event Horizon Telescope Collaboration et al. (2024a), 7: Mus et al. (2025).

Problem 2 (MOP scalarized)**.**

$$\underset{x\in\mathbf{F}\subseteq\mathbb{R}^{(N+4)P}}{min} \quad F(x) := \sum_i^n \alpha_i f_i(x), \quad \alpha_i \geq 0, \forall i = 1, \ldots, n. \qquad \text{(MOP Scalar)}$$

Prob. (MOP Scalar) is equivalent to standard RML methods. However, the hyperparameter α_i are found during the optimization process, and thus, a survey is no longer needed.

For the expressions of the individual f_i we refer Tab. 2.1. Almost all of the data terms and regularization terms have been reported and applied to real data in previous works. As a notable exception, the HW-entropy has been extended to incorporate circular polarization, representing a key update to the method. In fact, we use:

$$R_{hw}(I, \hat{m}, M) = \sum_i^P I_i \left(\ln(\frac{I_i}{M_i}) + \frac{1+\hat{m}_i}{2} \ln\left(\frac{1+\hat{m}_i}{2}\right) + \frac{1-\hat{m}_i}{2} \ln\left(\frac{1-\hat{m}_i}{2}\right)\right), \qquad (2.1)$$

where the subindex i corresponds to the ith-element of the associated vector, M is a model image, and $\hat{m}$ is total polarization fraction, i.e. $\hat{m} = \frac{\sqrt{I^2m^2+V^2}}{I}$ with linear polarization fraction m and the Stokes parameter V. In total, in this work, we balance the terms described in Table 2.1: χ^2_{cph}, χ^2_{lca}, χ^2_{amp}, R_{entr}, R_{tv}, R_{tv2}, R_{l1}, R_{flux}, $\mathbf{1}_{ms}$, R_{ngMEM}, χ^2_{pvis}, χ^2_m, R_{ptv}, R_{ms}, R_{hw+cp}, χ^2_{cvis}.

Mus et al. (2025) extended `MOEA/D` and `MO-PSO` to simultaneously reconstruct the scattering screen and image structure, validated for static sources with a moving screen. In this chapter, we do not attempt to recover the screen velocity, reserving this for future work. Nonetheless, beyond validation, this study also documents developments, such as a dynamic source evolution pipeline, that pave the way toward this goal. For completeness, we include the scattering regularizer in Tab. 2.1, although it is not used in this study. Additionally, circular polarization is reconstructed in the upcoming analysis, but we do not validate it here as it was not one of the parameters to evaluate in the study.

`MOEA/D` and `MO-PSO` are both multiobjective optimization algorithms built upon the concept of Pareto optimality and designed to find solutions that balance a common set of objectives. However, they solve different problems. On one hand, `MOEA/D` explores the Pareto front using a genetic algorithm approach, that is, finding solutions (images) that are compromises between the data terms and regularizers. This strategy makes it easy to identify a broad range of valid solutions, but at the cost of a high computational effort and the loss of information about the marginal impact of each regularizer.

On the other hand, `MO-PSO` searches the Pareto front globally, but operates in a continuous search space where the weights are not fixed. This way, instead of computing the entire Pareto front, it uses a swarm-based strategy to rapidly converge toward a single, optimal reconstruction that best balances the objectives, that is, searching for the minimal distance to the ideal point. This faster approach instead computes the marginal contribution of each regularizer, yielding a unique solution. The efficiency of `MO-PSO` also resides in the different evolutionary strategy, using swarm intelligence instead of the genetic operations in `MOEA/D`, and solving the single-objective minimization problems MOP Scalar by fast gradient-based convex optimization algorithms rather the slower genetic evolution.

Formally, this also translates to a difference in the objectives functions form. For `MOEA/D`, using Müller et al. (2023), for example in Stokes I:

$$
\begin{aligned}
f_1 &:= \beta S_{\text{amp}} + \gamma S_{\text{cph}} + \delta S_{\text{lca}} + \zeta R_{l1},\\
f_2 &:= \beta S_{\text{amp}} + \gamma S_{\text{cph}} + \delta S_{\text{lca}} + \theta R_{\text{tv}},\\
f_3 &:= \beta S_{\text{amp}} + \gamma S_{\text{cph}} + \delta S_{\text{lca}} + \tau R_{\text{tv2}},\\
f_4 &:= \beta S_{\text{amp}} + \gamma S_{\text{cph}} + \delta S_{\text{lca}} + \eta R_{l2},\\
f_5 &:= \beta S_{\text{amp}} + \gamma S_{\text{cph}} + \delta S_{\text{lca}} + \epsilon R_{\text{flux}},\\
f_6 &:= \beta S_{\text{amp}} + \gamma S_{\text{cph}} + \delta S_{\text{lca}} + \kappa R_{\text{entr}},\\
f_7 &:= \beta S_{\text{amp}} + \gamma S_{\text{cph}} + \delta S_{\text{lca}}.
\end{aligned}
$$

For `MO-PSO`, using Mus et al. (2024a) notation:

$$
\begin{aligned}
f_1 &:= \zeta R_{l1},\\
f_2 &:= \theta R_{\text{tv}},\\
f_3 &:= \tau R_{\text{tv2}},\\
f_4 &:= \eta R_{l2},\\
f_5 &:= \epsilon R_{\text{flux}},\\
f_6 &:= \kappa R_{\text{entr}},\\
f_7 &:= \beta S_{\text{amp}} + \gamma S_{\text{cph}} + \delta S_{\text{lca}}.
\end{aligned}
$$

2.2.2 ngMEM

To incorporate the recovery of dynamics in the MOP, it is necessary to include the ngMEM functional Mus & Martí-Vidal (2024), which expresses the correlation between multiple frames over time. It is defined as the weighted Shannon entropy between frames:

$$
R_{\text{ngMEM}}(p) := \sum_{n,l\neq m} T_n^{lm}, \quad \text{where}
$$

$$
T_n^{lm} := e^{-\dfrac{|t^l - t^m|^2}{2\tau^2}} \left(|p_n^l - p_n^m| + C\right) \log\left(|p_n^l - p_n^m| + C\right).
$$

Therefore, for every pixel p_n appearing in a pair of frames l, m defined at times t^l and t^n, respectively, the ngMEM entropy can be decomposed into two main parts: a Gaussian frame-correlation regularizer which relates neighbor frames (also called "time memory") and the time entropy (which transmits the evolution through the broadness of the pixel p_n between frames). In a fast evolving source, correlations between neighbor frames need to be properly set (see Sect. 2.4.1).

2.2.3 Wavelets and description of a movie

To address the sparsity of the array, we compose the functionals f_i with a wavelet dictionary Ψ, describing the image in total intensity via the coefficients ω_I^j in every frame j. Therefore, if a movie is represented by a sequence of single, individual images I^j, the problem description MOP x is the vector:

$$x = \left[\omega_I^1, \omega_I^2, \omega_I^3 ...\right], \tag{2.2}$$

Every single frame image is related to the respective wavelet coefficient array through convolution with the dictionary, i.e. $I^j = \Psi\omega_I^j$.

In this framework, Prob.(MOP Scalar) can be rewritten as

Problem 3 (MOP scalarized with wavelets)**.**

$$\underset{x\in\mathbf{F}\subseteq\mathbb{R}^{(N+4)p}}{min} \quad \sum_{i}^{n}\sum_{j=1}^{N}\alpha_i f_i\left(\Psi w_I^j\right), \quad \alpha_i \geq 0, \forall i = 1, \ldots, n. \tag{MOP-S-W}$$

For the full description of the different f_i we defer to Mus et al. (2025). The extension to polarimetry is straightforward by replacing the Stokes I coefficients in every frame ω_I^j with the coefficients in Stokes Q, U, and V: $\omega_Q^j, \omega_U^j, \omega_V^j$. The novelty of this work is the inclusion of time-evolving wavelet-dependent polarimetric functionals.

2.3 Validating the pipeline using synthetic data of SgrA*

In this section, we present the main algorithmic development for this work, the construction of a robust pipeline to recover a dynamically evolving source.

Given the sparse data coverage, a multi-modality approach accounts for different morphologies and dynamic correlations that fit well the data. Applying `MOEA/D` and `MO-PSO` to dynamic reconstruction is not a novel dynamic regularization but an efficient hyperparameter search using standard terms.

The procedure (pseudocode in Algorithm 1) proceeds as follows: First, we use `MO-PSO` to reconstruct the Stokes I movie using a field of view of 128 $\times$ 128 mas, 16 pixels and 49 frames. This step requires a initialization point (fron now on, prior, though not in the Bayesian sense) and the multiscale dictionary. The priors is constructed solely from closure amplitudes and closure phases. Two priors are considered: one from a maximally correlated (i.e. static) and one

minimally correlated (i.e. snapshot imaging); the latter is selected (details in Subsection 2.4.2).

The number of frames was optimized to balance temporal resolution and sufficient visibility coverage per frame: too many frames dilute visibility data, while too few suppress dynamic features. A multiresolution representation could in principle be obtained via a hard thresholding step in the `Dog-Hit` algorithm, as studied independently in (Müller 2025). Although we also use a wavelet dictionary here, significant differences exist: in (Müller 2025), the multiresolution support served as the only temporal regularization, tightly aligning emission across frames with a large sparsity weight.

In contrast, we relax this assumption, allowing for greater frame-to-frame variability and relying instead on balancing data fidelity and regularization terms. We construct the multiscale prior by copying an unconstrained static reconstruction into each wavelet scale instead, exploiting the property that the sum of all scales recovers a delta source. Thus, although both approaches use multiscale priors, the assumptions and behavior differ substantially. As discussed in Sec. 2.2.3, wavelets are not necessary to recover dynamics but help achieve cleaner reconstructions.

Once the prior is selected, we run `MO-PSO` using amplitudes and closure phases for each initialization, identifying the best solution (global minimum) as the optimal weight combination in the convex optimization problem. Simultaneously, we use `MOEA/D` to explore different local minima, accounting for the sparsity of the coverage. This parallel exploration confirms that the `MO-PSO`-recovered movie is included in the broader solution space and allows visualization of alternative reconstructions, as detailed in Subsection 2.4.3.

After obtaining the Stokes I reconstruction from `MO-PSO`, we self-calibrate the data by fitting phases only, then proceed to polarization. `MO-PSO` is then run independently on each frame for polarization, using the Stokes I reconstruction as the updated starting point. The final full-Stokes movie is regridded, rescaled, and interpolated to allow uniform comparison with results from other pipelines participating in this collaborative effort. In summary, the final movie represents a balanced solution incorporating standard EHT regularizers (including polarization), wavelet sparsity terms from `Dog-Hit`, and the ngMEM time-entropy regularizer.

Robust validation of the dynamic strategy and its limitations requires a structured process: a validation ladder. This ladder uses synthetic models[†] of Sgr A*with simulated corruptions based on April 11 observations, featuring varying

[†]Throughout this paper, the terms model and ground truth are used as synonyms.

Algorithm 1 Dynamic Strategy for Movie Reconstruction

Require: Synthetic visibility data $\mathcal{V}$, prior, regularization terms $\mathcal{R}$
Ensure: Final full Stokes movie $\mathcal{M}$
  Set initialization prior as maximally correlated static movie $P_{\rm init}$
  Initialize `MO-PSO` with prior $P_{\rm init}$ and parameters
  Run `MO-PSO` using amplitudes & closure phases
  Store best-found Stokes I movie $\mathcal{M}_I^{\rm PSO}$
  Simultaneously, run `MOEA/D` to sample multiple local minima:
    Define subproblems reflecting coverage sparsity
    Optimize each with shared information
    Collect candidate set $\mathcal{S}_{\rm MOEAD}$
  Assert $\mathcal{M}_I^{\rm PSO} \in \mathcal{S}_{\rm MOEAD}$
  Self-calibrate phases only, using $\mathcal{M}_I^{\rm PSO}$
  for $f = 1, \ldots, n_{\rm frames}$ **do**
    Initialize `MO-PSO` for frame f with start $\mathcal{M}_I^{\rm PSO}[f]$
    Run `MO-PSO` to recover full Stokes on frame f
  end for
  Regrid, rescale, and interpolate frames to uniform grid
  return Final movie $\mathcal{M}$

morphologies and increasingly complex dynamics. We first describe the synthetic data properties, then present results for all models, and finally discuss the outcomes and limitations of the mathematical formulation and regularizers used.

2.3.1 Synthetic data

The data for all models presented in the validation ladder were synthetically generated using the April 11, 2017 u-v coverage and the best time window (Farah et al. 2022). Data include thermal noise and gain corruptions randomly varying between scans, with amplitude gains for each scan drawn from uncertainties based on 1924–2914 (PKS 1921–293, OV–236) April 11 complex gain uncertainties (Issaoun et al. 2022). We perform a time-dependent variant of the network calibration (Event Horizon Telescope Collaboration et al. 2019c), as described in Event Horizon Telescope Collaboration et al. (2022b), applied according to the ALMA lightcurve corresponing to April 11 Wielgus et al. (2022); Mus et al. (2022) light curve. Before generating the data, each model was blurred with the diffractive scattering kernel described in Event Horizon Telescope Collaboration et al. (2022c), and then added a refractive scattering screen. Final data were averaged over 60 s intervals. For further details, see Event Horizon Telescope Collaboration et al. (2025) and Dahale (2025).

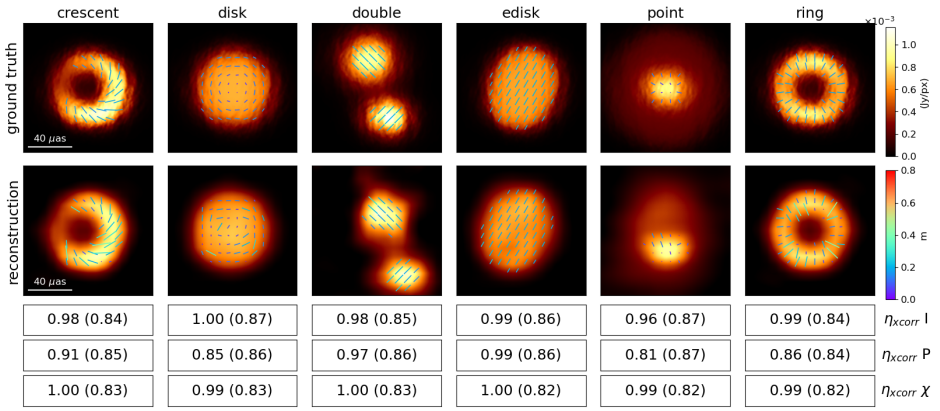

Figure 2.1: Static model reconstructions. Top row depicts the average movie of the models and bottom row, the same but of PSO reconstructions. Values in parenthesis indicate the passing threshold, while the ones outside are those found.

2.3.2 Models

Models fall into three categories. Static models (no dynamics) feature six morphologies: crescent, disk, elliptical disk (e-disk), double, point source, and ring.

Dynamic geometric models simulate dynamic features on m-ring structures (Johnson et al. 2020), blurred with a circular Gaussian (Event Horizon Telescope Collaboration et al. 2022c). Variants include: `mring+hsCW` (clockwise orbiting hotspot, 80 min period), `mring+hsCCW` (counter-clockwise), `mring+hs-cross` (hotspot crossing ring), `mring+hs-not-center` (off-centered orbit), `mring+hs-pol` (polarization-changing hotspot), `mring+hs-incoh` (incoherent motion), and finally the `mring-varbeta2` (beta2 counter-clockwise variation; β_2 as defined in Palumbo & Wong 2022).

Finally, GRMHD models were taken from the KHARMA ("Illinois v3") library, displaying a range of physical parameters, including black hole spin (a_*), ion-to-electron temperature ratio in high density region (R_{high}), and inclination angle (i). The selected models are `grmhd1` (MAD, $a_* = +0.94$, $R_h = 160$, $i = 30°$), `grmhd2` (MAD, $a_* = +0.5$, $R_h = 160$, $i = 150°$), `grmhd2+hs` (a variant of `grmhd2` with an added hotspot) and `grmhd8` (MAD, $a_* = +0.94$, $R_h = 40$, $i = 170°$). Full model descriptions are provided in Event Horizon Telescope Collaboration et al. (2025).

In order to evaluate these models, we focus on answering a set of questions for each type. Some of them are common for all models, such as do we fit the

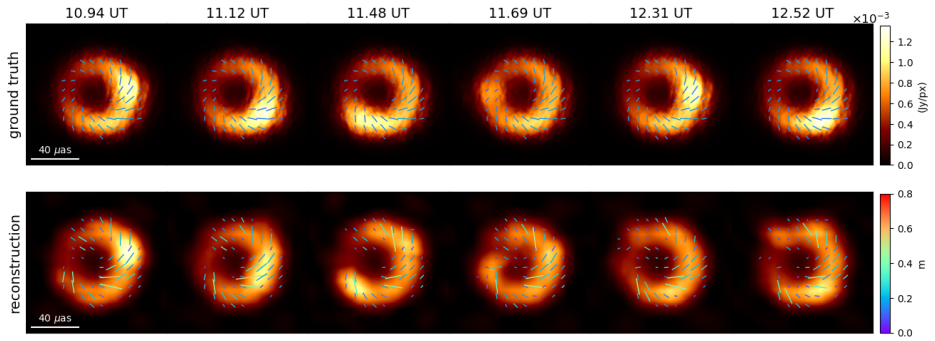

Figure 2.2: Geometric model mring+hsCW. Top row depicts the models at different timestamps and the bottom row, the ones on PSO reconstructions.

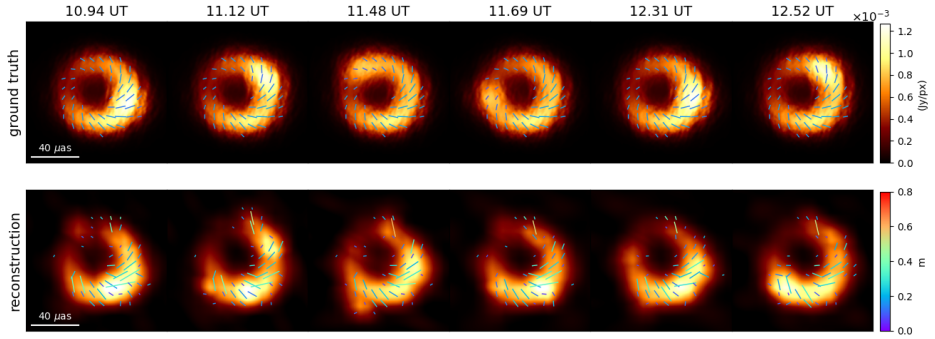

Figure 2.3: Geometric model mring+hsCCW. Top row depicts the models at different timestamps and the bottom row, the ones on PSO reconstructions.

data? or do we recover the underlying structure in Stokes I, Q, and U? Other questions are specific for each of the models. For instance, for the static models it is important to specify whether we hallucinate dynamics. For the dynamic geometric and GRMHD models, we need to answer the following questions: do we recover coherent orbital motion and non-orbital motion? the morphology and dynamic of the polarization field? and is there a bias towards recovering coherent motion?

2.3.3 Results

This section presents the final reconstructions for all models in the validation ladder. Evaluation of the reconstructions primarily use cross-correlation between

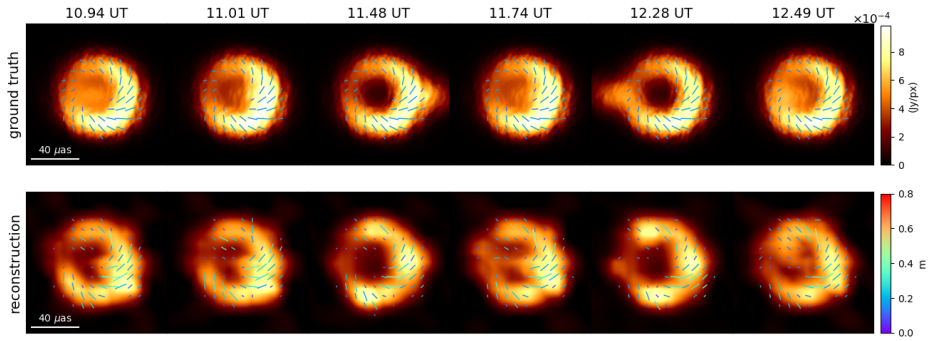

Figure 2.4: Geometric model `mring+hs-cross`. Top row depicts the models at different timestamps and the bottom row, the ones on PSO reconstructions.

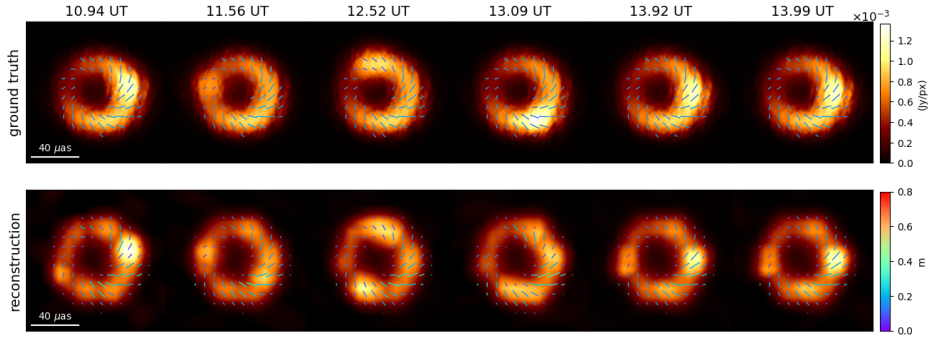

Figure 2.5: Geometric model `mring+hs-incoh`. Top row depicts the models at different timestamps and the bottom row, the ones on PSO reconstructions.

the ground truth and reconstruction; for geometric and GRMHD models, we additionally assess the recovery of position angle (PA) and pattern speed. Detailed evaluation metrics are provided in Dahale (2025). The validation ladder specifically addresses the questions outlined in Tab.2.5 and discussed further in Sec.2.3.4. Thresholds for successful reconstruction were deliberately set very high in Dahale (2025), anticipating the significant scientific impact of detecting resolved dynamics at event-horizon scales. A reconstruction is considered successful only if it passes all applied tests across all metrics. Consequently, even reconstructions that may appear visually convincing—often outperforming earlier Sgr A*results when inspecting the combined static and dynamic structure—can still fail validation, as the dynamic component may only reveal discrepancies after subtracting the median (static) image, where the residual variability appears less clear than in

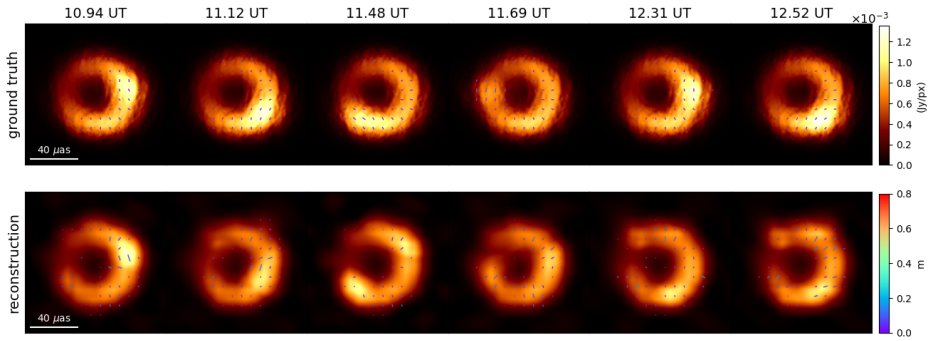

Figure 2.6: Geometric model `mring+hs-pol`. Top row depicts the models at different timestamps and the bottom row, the ones on PSO reconstructions.

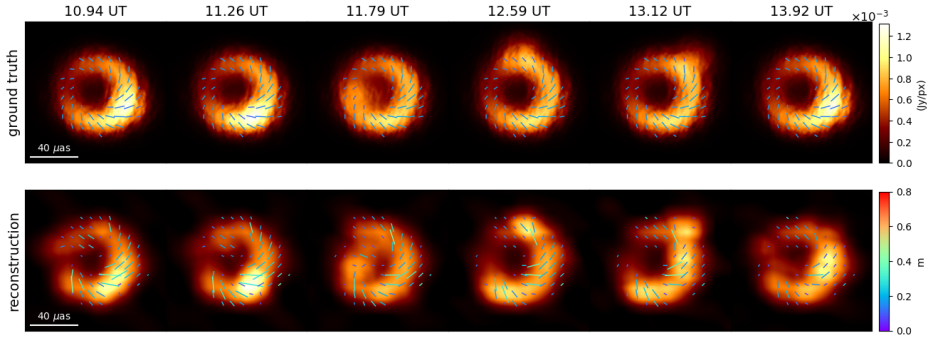

Figure 2.7: Geometric model `mring+hs-not-center`. Top row depicts the models at different timestamps and the bottom row, the ones on PSO reconstructions.

the ground truth.

2.3.3.1 Static models

We present the reconstructions for all static models in Fig. 2.1. The top row shows the ground truths; the bottom row shows the reconstructed average images within a $128 \times 128\,\mu$as field of view, with EVPAs indicated by ticks and fractional polarization (m) shown in the colorbar. Reconstructions are evaluated against ground truths using the nxcorr metric (Dahale 2025), with thresholds in parenthesis next to the values to determine pass/no pass status. Results show great quality cross-correlation, particularly in Stokes I and polarization angle χ.

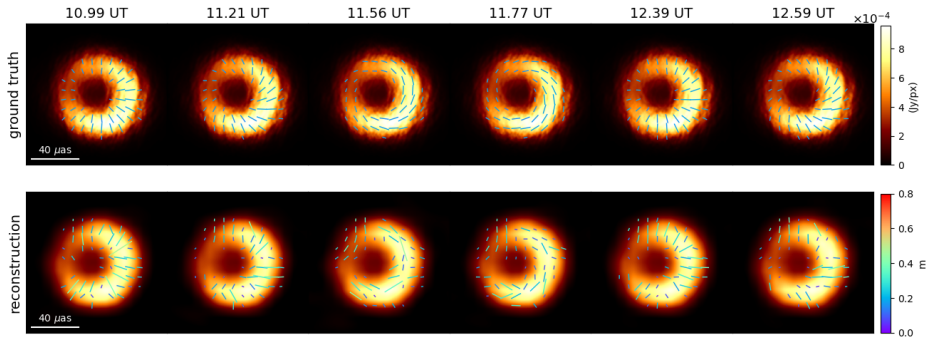

Figure 2.8: Geometric model `mring-varbeta2`. Top row depicts the models at different timestamps and the bottom row, the ones on PSO reconstructions.

All static reconstructions easily pass the nxcorr threshold in total intensity, with values close to 1. Visually, key features are well recovered, including the ring-like structures in the crescent and ring models, the brightness distributions, the circular and elliptical morphologies in the disk and edisk models, the position of the double source, and the central spot and diffuse emission in the point source. Notably, these reconstructions achieve significantly higher fidelity than previous RML reconstructions of Sgr A*(Event Horizon Telescope Collaboration et al. 2022c), especially for the point source model, which has proven to be challenging in other methods in this common effort. This improvement reflects both the superior data quality of April 11 and enhancements to the data processing pipeline (i.e. the significant improvements derived from taking the average from a dynamic reconstruction over static reconstructions with an inflated noise level), a point we discuss further in Sec. 2.4.4. While linear polarization reconstructions show good EVPA orientation, they perform slightly worse than Stokes I, likely due to minor inaccuracies in recovering the polarization fraction.

In summary, the static models are recovered very well and pass the validation ladder, demonstrating both the suitability of our pipeline for static imaging and that it does not introduce artificial dynamics when reconstructing static movies.

2.3.3.2 Dynamic geometric models

For the geometric models, the success in recovering intended features varies by case. Figures 2.2–2.8 display six exemplary frames from both the ground truth and reconstructed movies, showing total intensity (colormap) and fractional polarization (colored ticks). A summary of the quantitative evaluation is provided in Fig.2.9. We assess each model based on the cross-correlation between the dynamic

components of the ground truth and reconstruction, the position angle shift of the brightest component over time, and the pattern speed. It is important to note that Fig. 2.9 shows correlations between the dynamic components only (that is, the difference between each frame and the median image) not between the full movies. Since the dynamic component is roughly an order of magnitude fainter than the static structure (at a dynamic range typical for EHT data (Event Horizon Telescope Collaboration et al. 2019d, 2022c)), correlations computed over the full models can overshadow the fainter dynamic features. However, dynamic-only correlations also do not fully capture reconstruction success, as they focus on a small fraction of the overall structure. For instance, Fig.2.14 shows the correlation between the full models (static + dynamic), displaying a better performance than using only the dynamic component. In the following, we discuss each dynamic geometric model individually.

mring+hsCW For this model, the clockwise motion of the orbiting hotspot is visually well recovered, with 5 out of 6 frames in Fig.2.2 closely matching the ground truth. The overall correlation between the true model and reconstruction is good, exceeding the threshold for every frame (see Fig.2.14), and the static component is also accurately recovered. Moreover, the retrieved pattern speed is close to the ground truth. However, when analyzing the dynamic component, a common artifact emerges: a secondary hotspot appears 180° opposite the primary hotspot, occasionally confusing the recovered position angle (based on the brightest pixel). Although the hotspot motion and static component resembling an asymmetric ring structure are tracked reasonably well, the dynamic component fails to meet the cross-correlation threshold, with only 26% of frames passing. This shortfall is explained by an overestimation of the contrast between the dynamic and static components.

mring+hsCCW Fig.2.3 shows that for this model, we capture the static component and overall ring+hotspot structure well, with excellent correlation between the recovered and ground truth full models. The hotspot is temporarily tracked visually, consistent with 43% of frames passing the PA criterion; however, the clarity is limited, as only 15% of frames pass the cross-correlation threshold after subtracting the static component, isolating the fainter hotspot. Similar to the `mring+hsCW` model, the reconstruction is hindered by a secondary phantom hotspot and an inaccurate contrast between dynamic and static components. The recovered pattern speed differs notably from the ground truth, likely due to a failure in the automatic pattern speed extraction (described in Dahale (2025)), as suggested by the autocorrelation plot in Fig.2.9. This plot reveals a bi-modal

structure: one component tracking a clockwise and another a counter-clockwise hotspot, the latter matching the correct pattern speed. These two trajectories are highlighted by black lines in Fig. 2.9, right panel of the second row. The decreased accuracy for `mring+hsCCW` compared to `mring+hsCW` suggests a possible implicit bias favoring clockwise motion, potentially introduced by the rotation of uv-points through the visibility plane.

mring+hs-cross For this model, shown in Fig.2.4, we observe a good visual match between the ground truth and the reconstruction, supported by a successful recovery of the static component and full model in almost every frame (see Fig.2.14). The hotspot is correctly placed within the ring at locations distinct from the static ring emission during its crossing. However, an artifact appears: a secondary component follows a trajectory through the lower arc of the ring without crossing it, likely linked to the prior used in the reconstruction. As a result, the dynamic component is poorly recovered, surpassing the evaluation threshold in only 1% of frames. The pattern speed is not a meaningful metric for this model, as the hotspot exhibits primarily horizontal motion rather than orbital motion; thus, we do not discuss the recovered pattern speed further.

mring+hs-not-center In this model, the orbiting hotspot follows a trajectory offset from the center of the bright ring. As shown in Fig. 2.7, the hotspot is recovered in all six displayed frames, clearly so in four. Visual inspection confirms accurate hotspot recovery outside the static ring emission, confirmed by the 68% of frames passing the PA criterion, along with successful static component reconstruction. However, only 35% of frames pass the cross-correlation metric for the dynamic component. Moreover, the pattern speed for this model is quite close to the ground truth, within the errorbars and therefore supporting the reconstruction's quality.

mring+hs-incoh The incoherent hotspot model, shown in Fig.2.5, is recovered fairly successfully, with the hotspot position accurately traced in all displayed frames, supported by 78% of frames passing the PA criterion in Fig.2.9. The overall cross-correlation is exceptionally good, indicating successful reconstruction of both the static component and the dynamic ring structure. However, the cross-correlation of the dynamic component alone is lower, with 25% of frames passing. While the position angle is consistently recovered, the reduced performance again stems from inaccuracies in recovering the contrast between the dynamic and static components. Similar to the `mring+hs-cross` example, the pattern speed is not

a meaningful evaluation metric for this model due to the incoherent nature of the motion; the observed correlation indicating clockwise motion arises purely by chance.

mring+hs-pol The outcome for this model is similar to `mring+hsCW` in terms of the dynamic component, with 68% of frames passing the PA criterion, and the pattern speed better recovered. As shown in Fig. 2.6, most frames correctly capture the hotspot position alongside the static ring structure. Additionally, 48% of frames pass the nxcorr_χ metric for the dynamic component, although the same limitations as model `mring+hsCW` persist: the appearance of a secondary phantom hotspot and incorrect contrast between dynamic and static components. This model also tests the ability to recover changes in the hotspot's polarization. In this respect, the reconstruction struggles, with only 10% of frames passing the polarization fraction (P) threshold; unsurprising given the challenges already present in the recovery of the hotspot's total intensity.

mring-varbeta2 The `mring-varbeta2` model is static in total intensity, but features a time-rotating EVPA pattern. To evaluate its performance, we do not apply the position angle or pattern speed metrics; instead, we examine changes in integrated polarization along different cylindrical orientations, characterized by β_2 (see Event Horizon Telescope Collaboration et al. 2021), shown in Fig.2.9, middle column, for this model. Figures2.9 and 2.8 demonstrate that the rotating EVPA pattern is recovered successfully in 66% of the frames, supported by strong correlation in χ for the dynamic component with 73% of the frames passing. However, only 18% of frames surpass the polarization fraction (P) threshold, again reflecting the challenges in recovering the polarization fraction.

In general, the dynamic geometric models struggle to pass the validation ladder. While successfully fitting the data and recovering the nxcorr for the full reconstruction, they fail to properly pass the nxcorr threshold for only the dynamic component and partly succeed in recovering the position angle and pattern speed.

2.3.3.3 GRMHD models

The last step of the validation ladder are the more complex GRMHD models, presented in Figures 2.10, 2.11, 2.12 and 2.13, following the same format as geometric models. As before, a summary of all evaluation plots for the dynamic component alone is separately presented in Fig. 2.15, and for the full model cross-correlation in Fig. 2.14.

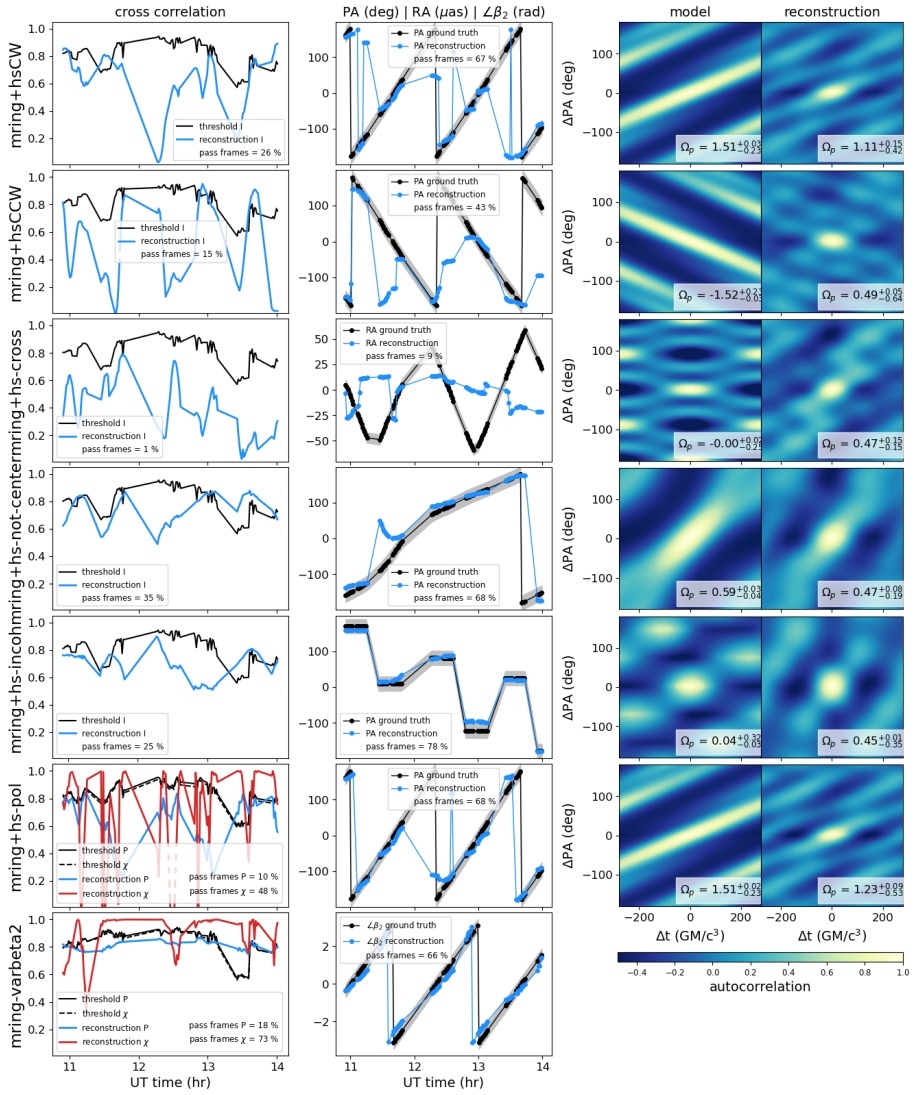

Figure 2.9: Summary of evaluation plots of the geometric models. Rows indicate the different models. First column corresponds to a comparison of the cross correlation, second column the position angle and third column the pattern speed.

GRMHD1 For the first GRMHD model (Fig. 2.10), the asymmetric shadow with a brightness spot toward the top is successfully recovered in every frame,

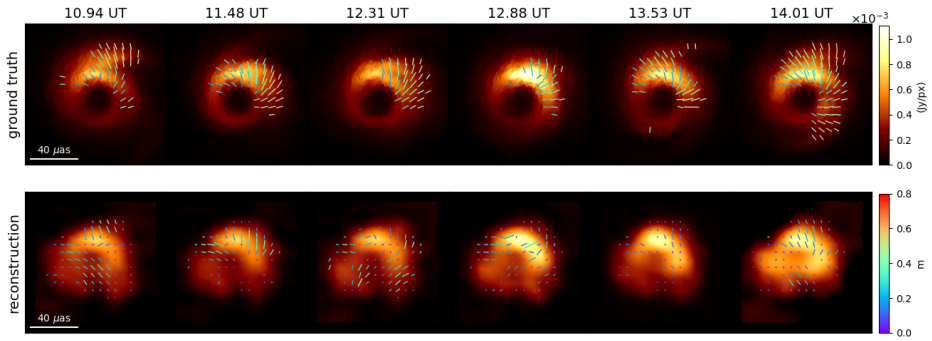

Figure 2.10: GRMHD model `grmhd1`. Top row depicts the models at different timestamps and the bottom row, the ones on PSO reconstructions.

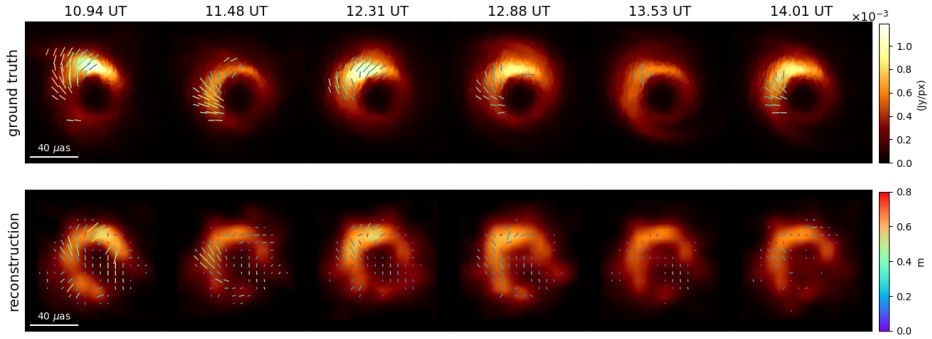

Figure 2.11: GRMHD model `grmhd2`. Top row depicts the models at different timestamps and the bottom row, the ones on PSO reconstructions.

reflected by correlation values consistently above the threshold. However, finer structures are not well captured: the central depression appears less clearly, and the brighter regions are better recovered than the fainter, more diffuse emission. Short-lived spiral arms in the accretion flow, visible in the ground truth (e.g., first and last frames), are not reconstructed. For the dynamic component, the pipeline performs robustly, with 86% of frames surpassing in Stokes I cross-correlation threshold, 67% in χ, perfect PA recovery, and 97% passing in $\angle\beta_2$. On the downside, the polarization cross-correlation never exceeds the threshold, with only 15% of the frames passing and although the recovered pattern speed has the correct negative sign, it falls outside the ground truth error range.

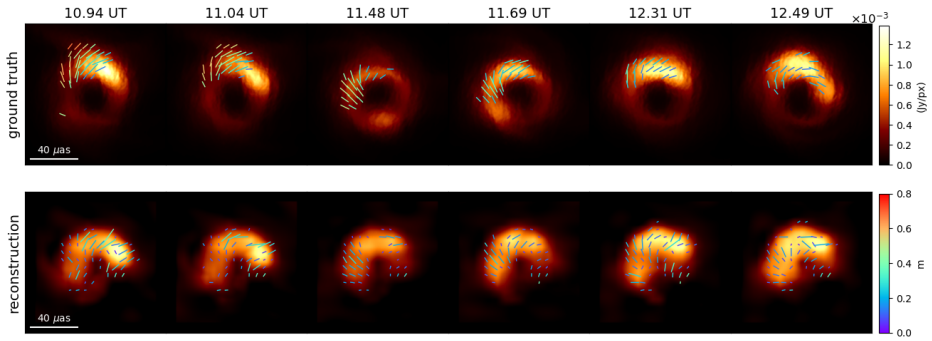

Figure 2.12: GRMHD model `grmhd2+hs2`. Top row depicts the models at different timestamps and the bottom row, the ones on PSO reconstructions.

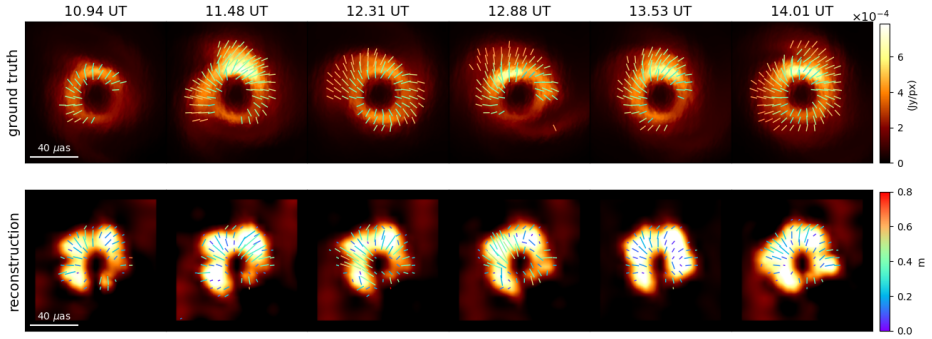

Figure 2.13: GRMHD model `grmhd8`. Top row depicts the models at different timestamps and the bottom row, the ones on PSO reconstructions.

GRMHD2 The GRMHD2 model reconstruction is shown in Fig.2.11. The performance is similarly strong to the previous case, with the asymmetric ring structure and correct position angle (top-left) recovered in every frame. The central depression is clearly visible, though finer features such as the diffuse accretion flow remain elusive. Cross-correlation in Stokes$I$ surpasses the threshold in 86% of frames, and χ passes in 55%. The PA is well recovered, with a solid 84% of passing frames, and $\angle\beta_2$ passes in an impressive 93% of frames. The pattern speed is better recovered than in the previous case, showing the correct sign and a closer value to the ground truth, though still outside the error bars. Polarization cross-correlation, however, is very limited and only passes in 8% of the frames.

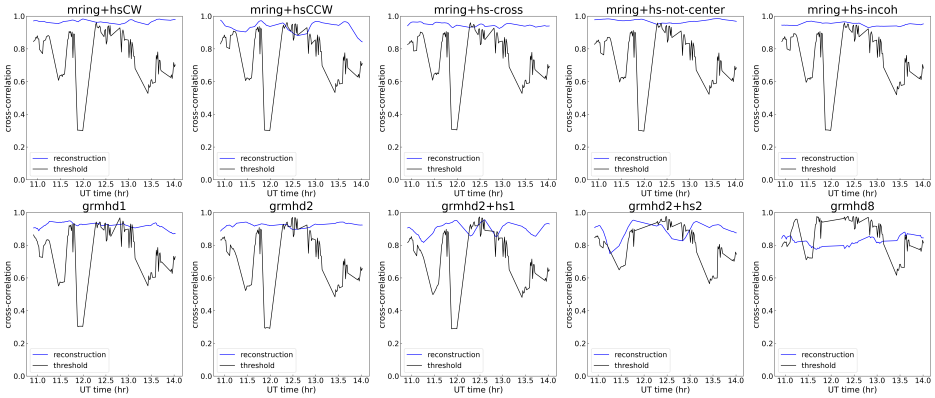

Figure 2.14: Cross-correlation for the geometric (top row) and GRMHD models (bottom row).

GRMHD2+hs2 This model is identical to GRMHD2 but includes an additional clockwise orbiting hotspot, increasing its complexity. Consequently, the pipeline struggles to maintain the earlier level of success. The reconstruction of the black hole shadow remains acceptable, although overall correlation has declined. The Stokes I cross-correlation surpasses the threshold in 73% of frames and in 65% for χ. The PA is recovered in 66% of the time, and $\angle\beta_2$ passes in 73% of frames. The pattern speed fails. Although polarization cross-correlation is better for this model, it reaches only 27% of passing frames, still failing to robustly recover the polarization features.

GRMHD8 The last GRMHD model is the most complex and variable, making it the hardest to recover. The ring structure and central depression are less well reconstructed. In this case, 44% of frames pass the Stokes I cross-correlation threshold and 55% the threshold for χ. The PA is however well recovered with 98% of the frames passing, and an impressive 90% of frames passing for $\angle\beta_2$. Polarization cross-correlation remains low, with only 14% of frames passing. However, the pattern speed is the best recovered among all GRMHD models, matching the correct sign, and passing the criteria, closely approximating the true value.

GRMHD models also struggle to pass the validation ladder. They fit the data properly and mostly pass the nxcorr criteria, except the polarization. They also show good results in recovering the position angle and a fair effort in $\angle\beta_2$, although they mostly fail in recovering the correct pattern speed. For clarity, a

full summary of the passing results for all different models has been compiled in Table 2.4.

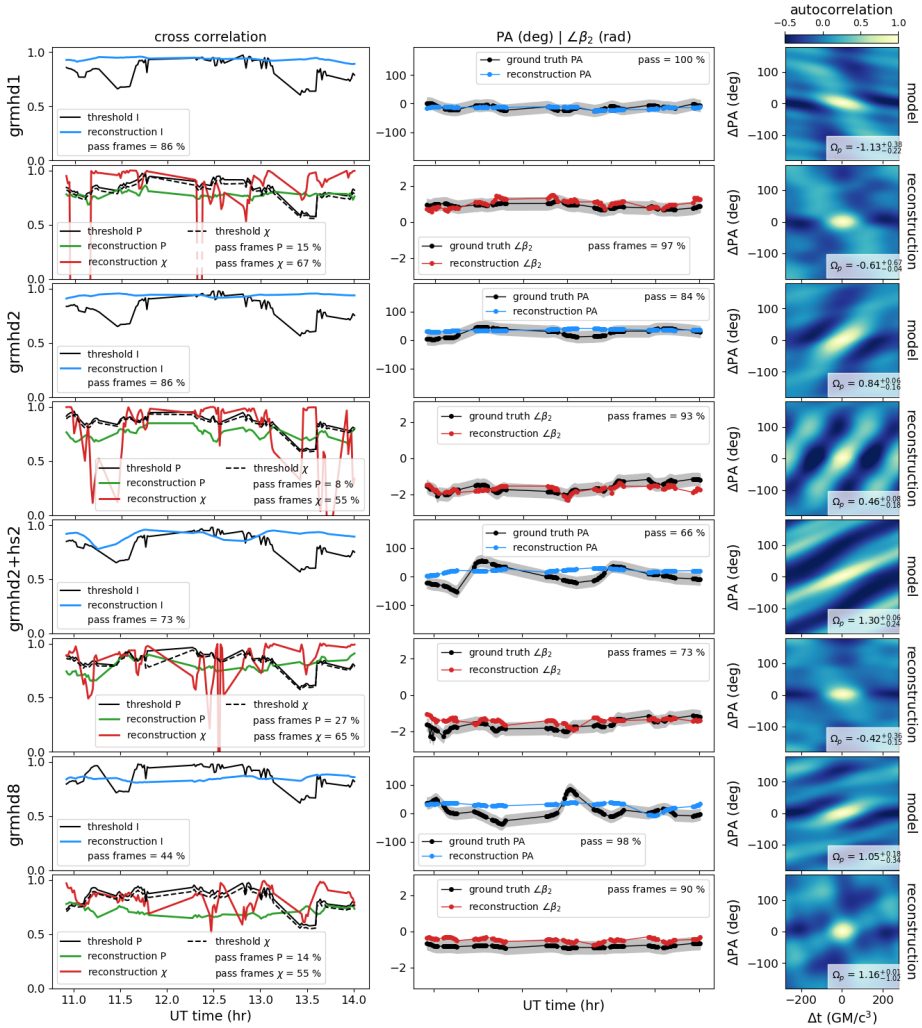

Figure 2.15: Summary of evaluation plots of the GRMHD models. Rows indicate the different models. First column corresponds to a comparison of the cross correlation, second column the position angle and third column the pattern speed.

2.3.4 Discussion and limitations

Based on the results, further discussed in Dahale (2025), we find that while our dynamic strategy shows partial success, it does not always fully meet the evaluation criteria. To systematically assess our performance, we organize the discussion of our results around the following questions.

For static models:

- **Do we fit the data?** Yes.
- **Do we hallucinate dynamics?** No; no artificial dynamics are introduced in static models.
- **Do we recover the underlying structure in Stokes I, Q, and U?** Overall yes. Total intensity reconstructions are exceptionally good, surpassing the quality of previous Sgr A* studies, particularly for the challenging point source. Polarization is generally well recovered, although minor issues with polarization fraction remain.

These results indicate that the dynamic pipeline does not introduce artificial dynamics to the reconstruction, and is able to extrapolate to non-ring models correctly (i.e. the assumption of a ring-like structure is not imprinted in the reconstruction too strongly). The performance in total intensity is remarkable. For dynamic geometric models we ask the questions:

- **Do we fit the data?** Yes. In fact, we find many different fitting structures that explain the data; see Sec. 2.4.3 for details.
- **Do we recover coherent orbital motion?** Partly. The static component is correctly recovered in almost every displayed frame, and the orbital motion is visually identifiable. However, after subtracting the static component, the dynamic features (roughly an order of magnitude fainter) reveal several recurring artifacts: secondary phantom images, contrast misfits between dynamic and static components, and partial absorption of dynamic features into the static ring emission. As a result, the dynamic component alone surpasses the threshold in only about half of the frames, and the recovered pattern speed appears noisy, although generally correct.
- **Do we recover coherent non-orbital motion?** Partly. The full model, dominated by the static background, is recovered correctly, and the non-orbital motion is identifiable by eye. However, the extracted dynamic component again suffers from similar artifacts. Notably, the hotspot is recovered

	model	χ^2_{logcamp}	χ^2_{cphase}	χ^2_{mbreve}
1	`crescent`	0.98	0.61	1.01
2	`disk`	0.95	0.72	1.00
3	`double`	1.08	0.78	1.00
4	`edisk`	1.15	0.59	1.00
5	`point`	1.12	0.42	1.01
6	`ring`	1.03	0.48	1.01
7	`mring+hsCW`	0.95	0.66	1.07
8	`mring+hsCCW`	0.95	0.59	1.14
9	`mring+hs-cross`	1.06	0.62	1.11
10	`mring+hs-incoh`	0.83	0.57	1.00
11	`mring+hs-not-center`	0.92	0.59	1.05
12	`mring+hs-pol`	0.89	0.56	1.00
13	`mring-varbeta2`	1.00	0.69	1.11
14	`grmhd1`	0.70	0.47	1.51
15	`grmhd2`	1.15	0.57	1.23
16	`grmhd2+hs2`	0.83	0.69	1.31
17	`grmhd8`	0.79	0.66	2.52

Table 2.2: Summary of average χ^2 values for all model reconstructions. Second, third and fourth columns are the χ^2 of the closure phases, log closure amplitudes and m-breve, respectively.

with these limitations whether it appears within the ring or outside the static emission for both the crossing and off-centered hotspot models.

- **Do we have a bias towards recovering coherent motion?** No. The position angle of the hotspot in the `mring+hs-incoh` model is recovered well, reflecting the intended incoherent jumping rather than coherent motion.
- **Can we recover dynamic polarization?** Only partly. The polarization angle of the static component (i.e., the ring) is recovered correctly, and the rotating EVPA pattern is captured well. The EVPA orientation of an orbiting hotspot is also recovered with some limitations. However, polarization fraction recovery remains problematic across all examples, exacerbated by contrast issues between dynamic and static components. Overall, fully recovering a dynamically evolving polarization structure remains challenging.

The analysis of the potential of `MO-PSO` to recover dynamics at the event horizon scales is further extended to GRMHD models, which have a much more complex and variable dynamics. For GRMHD models:

- **Do we fit the data?** Yes.
- **Do we recover the underlying Stokes I structure?** Partly. The full model (static + dynamic component) is recovered well in most frames. The central depression and overall position angle are accurately captured. However, finer, diffuse emission from the accretion flow, rapid motions near event-horizon scales, and small-scale dynamic features are not well reconstructed, as expected for such a sparse uv-coverage.
- **Do we recover the underlying Stokes P structure?** Partly. Reconstructions are relatively successful in recovering the EVPA pattern, an area where RML algorithms have previously struggled for Sgr A* (Event Horizon Telescope Collaboration et al. 2024b). However, the dynamic evolution of the polarization is not reliably recovered.
- **Can we recover the correct orbital motion?** Partly, with strong limitations. The dynamic variability of the GRMHD simulations hinders accurate recovery of orbital motion, particularly in the `grmhd2+hs2` example. Nonetheless, the sign of the pattern speed, though not its magnitude, is correctly recovered in most GRMHD cases.

Surprisingly, recovering the more complicated GRMHD models was more successful than the geometric. In fact, three of them have passing frames in Stokes I cross-correlation over 70% and the same ones recover the PA quite well, together with over 60% of passing frames in $\angle\beta_2$. Also, all of the models have over 50% passing frames in χ cross-correlation. In particular, the `grmhd1` and `grmhd2` model, with 86% of passing frames in cross-correlation Stokes I, 68% and 54% in χ and 85% and 89% in $\angle\beta_2$, constitute the best reconstructions in our strategy among geometric and GRMHD models. Regrettably, this victory does not translate into polarization cross-correlation, which is in all GRMHD models below 6%, undoubtedly failing to recover this challenging and rapidly changing feature.

In Table 2.5, we summarize our conclusions. Overall, our strategy is relatively successful, correctly recovering the general structure and polarization orientation in all examples, clearly improving upon previous RML results. However, when extracting the fainter dynamic component, clear limitations and recurring artifacts remain. While PA and pattern speed are generally well recovered, cross-correlation in both Stokes I and polarization for the dynamic component could be substantially improved. Given the anticipated impact of time-dynamic reconstructions of accretion flows at event-horizon scales, we set especially stringent passing thresholds and do not accept partly successful reconstructions.

2.4 Consistency checks

To test our pipeline's capabilities, we performed additional analyses on factors such as time regularization and the starting point. We also conducted a multimodality analysis using `MOEA/D` to assess the consistency of multiple solutions arising from sparse uv-coverage. The latter one has implications over the scope of a simple validation.

2.4.1 Impact of time memory

Time memory imposes temporal correlations between frames via a Gaussian:

$$e^{-\frac{|t^l - t^m|^2}{2\tau^2}},$$

where the time units is in frame-length, that is $|t^l - t^m| = 1$, and τ is the Gaussian width controlling the frame-to-frame correlation. For example, we chose $\tau = 1$, meaning the standard deviation of the Gaussian is one length of uniformly-distributed frame (i.e. 3.18 minutes for $\sim$ 3h of observations and 49 frames). This implies a time correlation of 60% between adjacent frames.

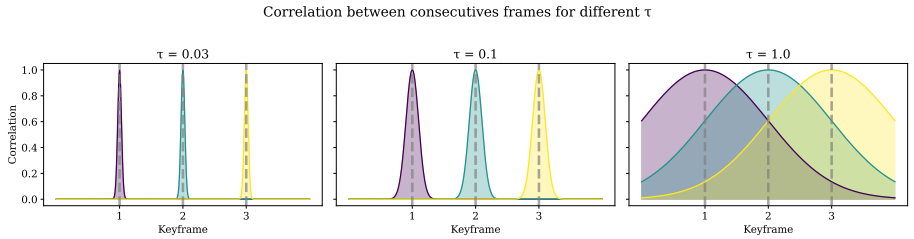

Figure 2.16: Squematic representation of the τ parameter and its impact on the correlation between consecutive frames.

For sources with complex dynamics, the choice of τ significantly affects movie reconstructions. Figure 2.16 shows how keyframes (x-axis) share information with neighbors through Gaussian curves. Increasing τ broadens the temporal overlap, strengthening correlations. A small τ leads to snapshot-like imaging and underrepresents temporal dynamics, while a large τ forces strong correlations, yielding effectively static reconstructions. In Table 2.3 we show different values for and the respective time correlation between adjcent frames.

τ	0.47	0.6	0.85	1	1.3
Correlation (%)	10	25	50	60	75

Table 2.3: Time correlation between adjacent frames (left column) and Gaussian width values τ.

The hyperparameter controlling the impact of this correlation with respect of the rest of functionals is the weight α_{ngMEM} associated with R_{ngMEM} (Mus et al. 2024a):

$$f_7 := \alpha_{ngMEM} R_{\text{ngMEM}}(p). \tag{2.3}$$

Unlike τ, which remains fixed during optimization, the weights are adaptively tuned for each dataset. Figure 2.17 illustrates the effect of α_{ngMEM}. The left column shows the ground-truth `mring+hsCW` model; subsequent columns show reconstructions for increasing values of α_{ngMEM}. Here, we fixed the data term weights to one and varied only α_{ngMEM}, setting all other weights to zero.

Top panels in Fig. 2.17 show visibility variance, bottom panels fitting quality per baseline, and middle panels recovered frames at different times. The trend is clear: higher α_{ngMEM} suppresses variability, while very small values produce overly dynamic reconstructions. This consistency check confirms that the optimization behaved as expected. Notably, excellent visibility fits are achieved across all variability levels, a point we discuss further in Sec. 2.4.3.

2.4.2 Initialization

The pipeline requires manual initialization, necessitating tests to assess its impact. As discussed, the two well-motivated options are a minimally correlated or a maximally correlated movie. Here, we test both using the representative `mring+hsCW` model. Figure 2.18 shows the results. Reconstructions are similar for both starting points, demonstrating that starting from a minimally correlated movie still recovers the intrinsic variability. This confirms the effectiveness of the time regularizer and the presence of genuine variability in the data.

We also evaluate the role of wavelets, specifically whether constraining variability to observed spatial scales and visibilities limits the range of possible source structures. Figure 2.19 compares reconstructions of the `mring+hsCW` example with and without wavelets. In both cases, the asymmetric ring and the hotspot's motion are correctly recovered, with previously noted limitations in dynamic-to-static

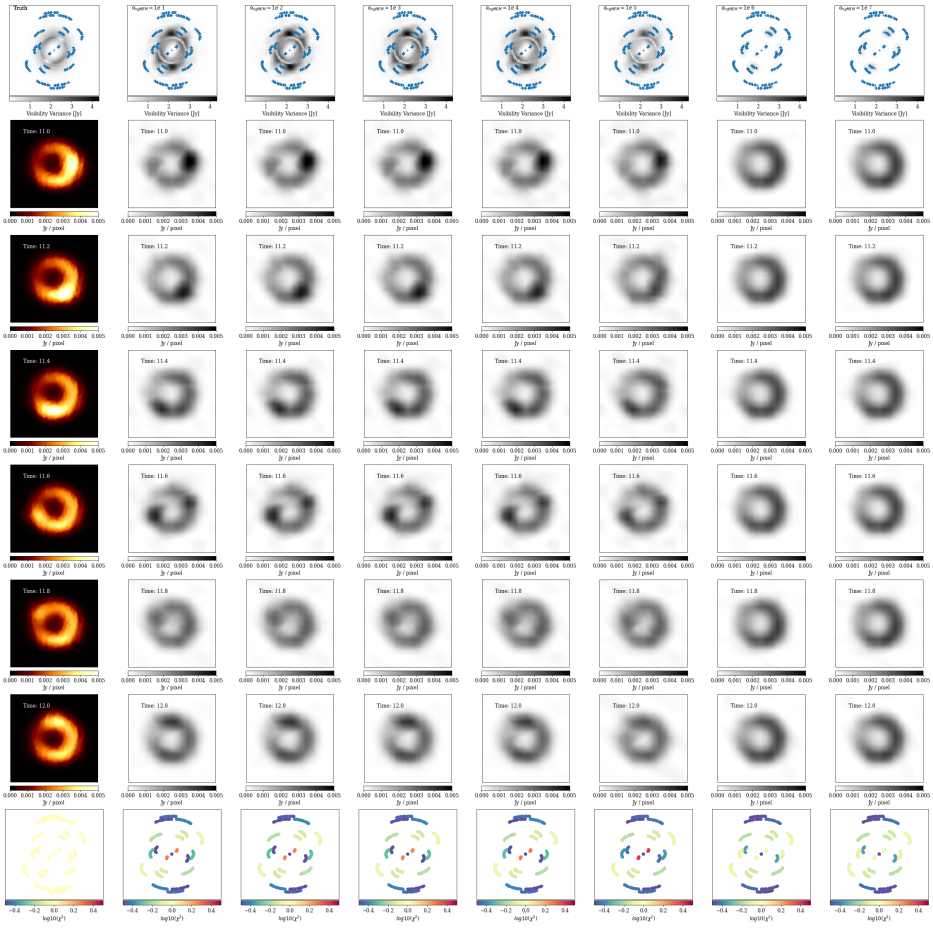

Figure 2.17: Effect of α_{ngMEM} parameter. Left column shows the ground-truth `mring+hsCW` model at a particular time stamp. Subsequent columns show reconstructions for increasing α_{ngMEM} (displayed in the legend of first row plots). Color scale for the reconstructions are in grey scale for better visualization. Top row corresponds to visibility variance plots of each reconstruction, while bottom row shows per-baseline χ^2-fits

contrast and the presence of a secondary phantom. The recovered dynamics are similar, but the reconstruction is noticeably cleaner when using wavelets.

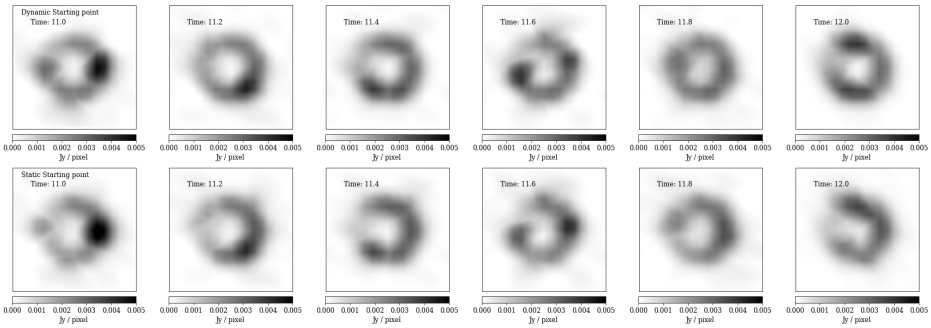

Figure 2.18: Comparison between different starting points for the pipeline. Top row shows the reconstruction of the mring+hsCW model at different time stamps using a dynamic starting point, while bottom row does with a static starting point.

2.4.3 MOEA/D multimodality analysis

The main advantage of `MOEA/D` is its ability to explore the multimodal posterior, i.e., the range of physically reasonable solutions that fit the data due to the sparse uv-coverage. `MOEA/D` does not explore the full infinite-dimensional solution space but focuses on solutions that fit the data and score well in total variation, sparsity, entropy, total flux conservation, and minimal negative flux. This allows for deeper insights into Sgr A*'s variability compared to algorithms that only find local minima. However, not all feasible solutions represent the true emission, making it crucial to discern feasible reconstructions carefully. In this section, we analyze the morphologies and time correlations recovered from the data and identify which reconstructions are plausible. Figure 2.20 shows the different solution clusters derived for the `mring+hsCW` model. The wavelet support constraint remains fixed during `MOEA/D` optimization; only regularizer weights are varied.

The left column shows the ground-truth model, while subsequent columns show representative cluster reconstructions. The top panels display visibility variability, the middle panels show frame snapshots, and the bottom panels depict per-baseline χ^2-fits. The data support a variety of morphologies and time-correlated structures, but not all resemble the true emission. Multimodality manifests itself mainly in the amount of dynamics, rather than in smoothness, substructure, or entropy.

Different clusters represent similar structures but vary in the dynamic component's strength relative to the static background. A recurring artifact is a secondary phantom hotspot (already reported in Sec. 2.3), mirrored at the ring's center, whose prominence varies between clusters, indicating morphological differ-

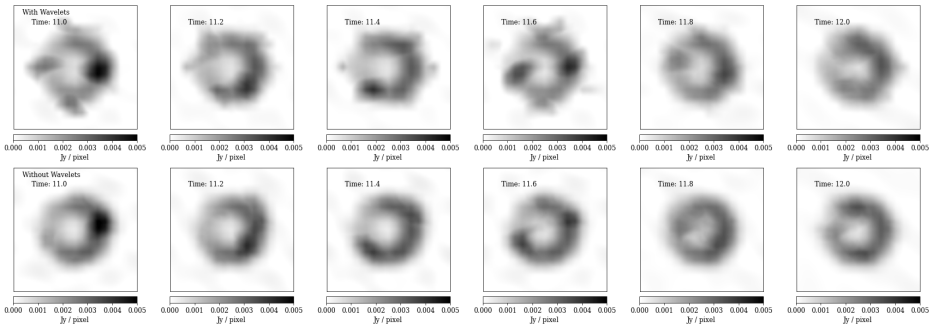

Figure 2.19: Effect of wavelets on the reconstructions of `mring+hsCW` model. Top row shows including wavelets at different time stamps and bottom row, without including them.

ences. It is important to note that plausibility does not guarantee correctness. For instance, both nearly static (e.g., cluster 0) and super-dynamic (e.g., cluster 10) reconstructions fit the data well but deviate significantly from the ground truth.

The fitting quality further differentiates clusters. In static solutions (clusters 0–5), variability is recovered mainly where visibilities are available, limited by the wavelet constraint. Well-fitting reconstructions (e.g., cluster 7) require modeling variability between visibility points. Across all clusters, the best fits occur for zero-baselines and longest baselines, which is expected: total flux is constrained mainly by ALMA-APEX baselines, and long baselines exhibit little intrinsic variability. Differences between clusters mainly arise in fitting intermediate baselines.

We conclude that multiple reasonable solutions exist that fit the Sgr A*data well, despite its limited quality. These solutions vary mainly in their degree of dynamics, including some that are too static or overly dynamic compared to the ground truth, but still fit the data well. A moderately dynamic movie provides the best approximation of the source behavior in this example, even though limitations of our pipeline (and traditional RML methods) prevent a fully robust reproduction of all dynamic features. Given the uniformly good data fits across all clusters, within RML methods it remains challenging to derive a purely data-driven constraint on the amount of variability. Importantly, this explicitly does not imply that Sgr A*'s data quality prohibits reliable reconstructions. Instead, it highlights that any selection criterion or alternative local search technique/algorithm needs to derive this heuristics (i.e. its architecture or hyperparameters) on as broad as possible synthetic data explorations, as done in this series of papers. Nevertheless, an analysis of the range of fittable dynamics presented here, enabled by global

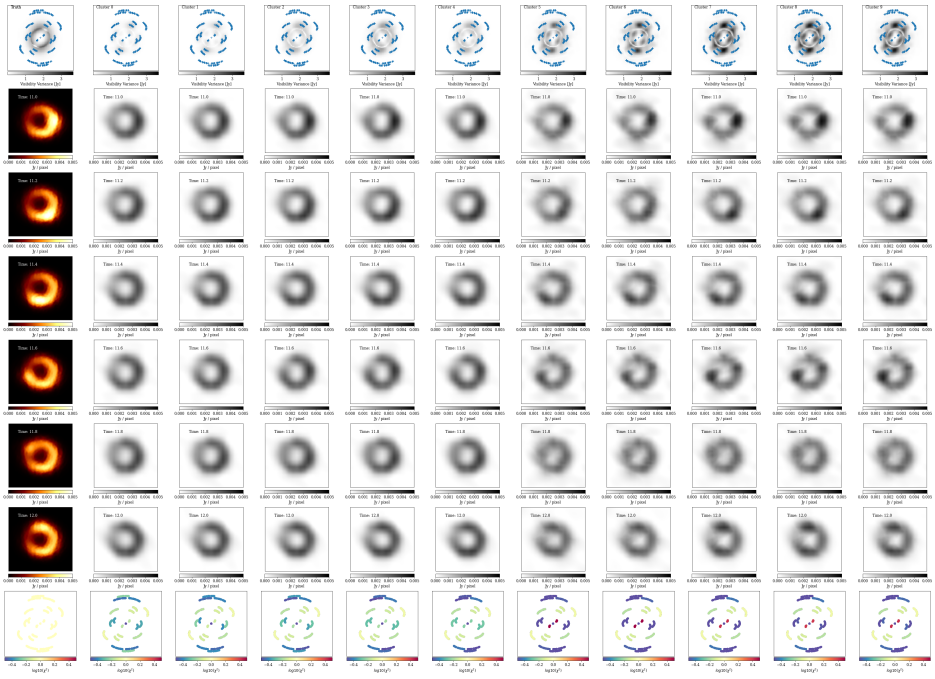

Figure 2.20: Different cluster solutions. Left column shows the ground-truth `mring+hsCW` model at a particular time stamp. Subsequent columns show representative reconstructions for different clusters (displayed in the legend of first row plots) at different time stamps. Color scale for the reconstructions are in grey scale for better visualization. Top row corresponds to visibility variance plots of each reconstruction, while bottom row shows per-baseline χ^2-fits.

optimization and multimodal exploration in this work, provides valuable insights.

2.4.4 Average vs. Static

The EHT has employed two methods to produce static images of dynamic sources, culminating in the first image of Sgr A*in full polarization (Event Horizon Telescope Collaboration et al. 2022a, 2024b). In Event Horizon Telescope Collaboration et al. (2022c), dynamics were marginalized by inflating the noise budget. In contrast, this work recovers a dynamic movie and derives a static image from the pixel-wise median of the recovered frames. As shown in Fig. 2.14, while the reconstruction of the dynamic component alone is limited (see Fig. 2.9 and 2.15), the full model dominated by the static emission is robustly recovered, even for challenging

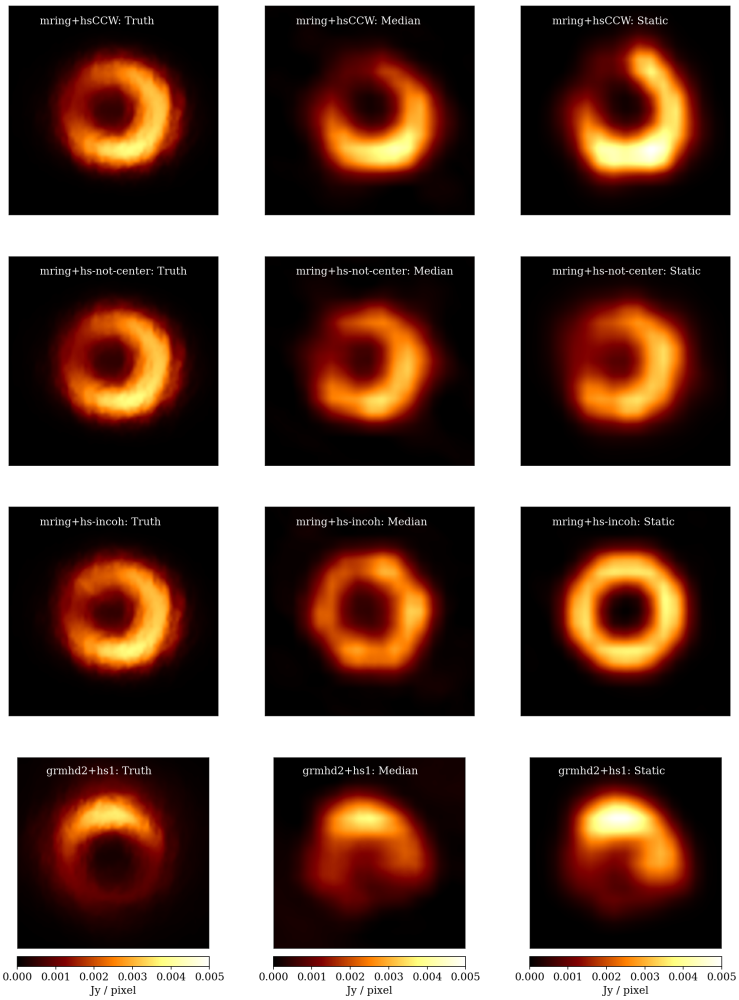

Figure 2.21: Comparison between ground truth (left column), movie-averaged (middle column) and static reconstructions (right column) for four representative models.

GRMHD datasets, an important achievement given the severe challenges of EHT data: extreme sparsity, low signal-to-noise, phase uncertainties, intrinsic variability and scattering.

We note significant improvements over earlier EHT efforts (Event Horizon

Models		χ^2_I	χ^2_P	$\eta_{\text{xcorr I}}$	$\eta_{\text{xcorr}\chi}$	$\eta_{\text{xcorr }P}$	σ_{vis}	PA	$\angle\beta_2$	Ω_p
static	`crescent`	✓	✓	✓	✓	✓	✓	-	-	-
	`disk`	✓	✗	✓	✓	✗	✓	-	-	-
	`double`	✓	✓	✓	✓	✓	✓	-	-	-
	`edisk`	✓	✓	✓	✓	✓	✓	-	-	-
	`point`	✓*	✗	✓	✓	✗	✓	-	-	-
	`ring`	✓*	✓	✓	✓	✓	✓	-	-	-
geometric	`mring+hsCW`	✓	✓	✗	-	-	-	✓	-	✗
	`mring+hsCCW`	✓	✓	✗	-	-	-	✗	-	✗
	`mring+hs-cross`	✓	✓	✗	-	-	-	✗	-	✗
	`mring+hs-incoh`	✓	✓	✗	-	-	-	✓	-	✓
	`mring+hs-not-center`	✓	✓	✗	-	-	-	✓	-	✓
	`mring+hs-pol`	✓	✓	-	✓	✗	-	✓	-	✓
	`mring-varbeta2`	✓	✓	-	✓	✗	-	-	✗	-
GRMHD	`grmhd1`	✓	✓	✓	✓	✗	-	✓	✓	✗
	`grmhd2`	✓	✓	✓	✓	✗	-	✓	✓	✗
	`grmhd2+hs2`	✓	✓	✓	✓	✗	-	✓	✓	✗
	`grmhd8`	✓	✗	✗	✓	✗	-	✓	✗	✓

Table 2.4: Summary of the tests passed (green) and failed (red) by the `MO-PSO` reconstructions of the ground truth videos. The asterisks indicate χ^2_I passes for closure phases but not for log closure amplitudes.

Telescope Collaboration et al. 2022c), particularly in geometric test reconstructions (most prominently for the point source) and polarimetric structure recovery in GRMHD simulations, where previous RML pipelines struggled (Event Horizon Telescope Collaboration et al. 2024b). Averaging over a recovered movie yields higher-quality static reconstructions than direct static imaging with an inflated noise budget, as demonstrated in Fig. 2.21, where we compare the ground truth (left column), movie-averaged (middle column), and static reconstructions (right column) for four representative cases.

2.5 Outlook

2.5.1 Better coverage

The extremely sparse uv-coverage of the current EHT April 11th 2017 observations necessitates complex inference procedures that are not always fully captured by the modeling approach of Eq. (MOP-S-W). However, future EHT observations with denser array configurations will improve the ability of our algorithms to reliably recover the ground truth movies of the target. As demonstrated in Mus et al. (2024b,a), `MO-PSO` and `MOEA/D` succeed in reconstructing accurate, full-polarimetric movies when applied to next-generation EHT arrays or observing campaigns with improved uv-coverage.

2.5.2 Future advances

The primary focus of this study is the development and validation of a dynamic movie-making pipeline in real-data scenarios using the 2017 April 11 EHT uv-coverage, constrained to the time window with more antennas and higher data quality. However, the advances made here also contribute to broader scientific capabilities and unique observables for the EHT in future array configurations. Parallel to this work, we have incorporated closure traces (Müller 2024), polarization observables robust to leakage and gain corruptions, RL delay offsets (Broderick et al. 2020), and multi-objective optimization strategies to simultaneously recover the scattering screen and intrinsic source structure (Mus et al. 2025). Future work will explore these new directions in greater detail. These developments are unique capabilities of `MO-PSO` and `MOEA/D` among all existing imaging algorithms.

Closure traces are closure quantities immune to most antenna-based calibration errors, notably the right–left gain ratio crucial for circular polarization recovery. Until now, large gain uncertainties and the lack of gain transfer across many sources have prevented the EHT from producing consistent, resolved circular polarization maps at event horizon scales (Event Horizon Telescope Collaboration et al. 2023, 2024b), even for static sources. Recent work by Müller (2024) extended `MOEA/D` and `MO-PSO` to recover polarimetric signatures directly from closure traces, demonstrating this potential for linear polarization for M87 using 2017 EHT data. Building on this, we have now extended in this study the multi-objective framework to include circular polarization, specifically by extending the HW-entropy, and have generalized the pipeline to handle source dynamics robustly as described above. By replacing the data fidelity terms (closure phases and amplitudes) with closure traces, these developments enable, for the first time, a robust multi-epoch study of Sgr A*'s circular polarization, including tracking the temporal evolution of Stokes V during flaring events. In upcoming studies, we aim to investigate the dynamics of interstellar scattering toward the Galactic Center and better constrain the parameters that determine the scattering screen by using the wide bandwith, in particular the lower-bands data of 2018 and subsequent observations.

Separately, Mus et al. (2025) demonstrated the simultaneous recovery of source structure and a moving scattering screen, solving a multi-objective optimization problem for a static source. Their work showed that it is possible to constrain the scattering screen's velocity at 230 GHz and recover ring structures even at 86 GHz. Combined with the robust dynamic pipeline described here (simply by just the scattering term to the multi-objective problem formulation), we now have the unique capability to extend this approach to dynamic sources, enabling the recovery of the evolving scattering screen and accurate velocity measurements. Such measurements are critical for refining flux variability timescales, improving

Question	Static	Geometric	GRMHD	MO-PSO summary	Limitations
Fit the data correctly	✓	✓	✓	• Does not hallucinate motion in static source data • Avoids coherent motion for uncorrelated hotspots • Recovers the polarization angle correctly • Retrieves the position angle in most cases	• The brightness of hotspots is sometimes incorrect • Secondary phantom features appear • Polarization fraction not well-recovered • Dynamic components can be noisy or inconsistent • The method still struggles with the kind of variability seen in GRMHD simulations
Recover the correct morphology and orientation of the total intensity image	✓	✓	✓		
Recover the morphology of the polarization vector field	✓	✓	✗		
Recover the dynamics of the polarization vector field	-	✗	✗		
Don't hallucinate dynamics	✓	-	-		
Recover the direction of coherent orbital motion	–	✗	✓		
Recover the magnitude of coherent orbital motion (pattern speed)	–	✗	✗		
Recover non-orbital motion with the correct direction and speed	-	✗	-		
Discriminate between coherent and incoherent motion	-	✗	-		

Table 2.5: Summary of evaluation questions on `MO-PSO` reconstructions. Cells are shaded: green = pass, red = fail, – = not applicable.

the interpretation of observed structures, and gaining insights into the physical properties of the Galactic Center's interstellar plasma. These advances will not only enhance VLBI imaging but also have broader applications, such as improving transient searches.

2.6 Conclusion

Standard RML techniques constitute one of the principal methods within the set of forward-imaging strategies for VLBI. However, they present significant limitations. RML methods are based on a weighted sum of data terms and regularizers, with classical approaches relying on a survey over hyperparameter space to identify a combination that yields satisfactory reconstructions. This process is computationally expensive, especially when applied to complex problems such as dynamic imaging of highly variable sources like Sgr A*.

Müller et al. (2023) modeled a natural extension to the RML framework, addressing many of these limitations. In particular, the use of PSO as a meta-heuristic allows for efficient exploration of the hyperparameter space, reducing unnecessary evaluations and computational power. Another advantage of the multi-objective optimization framework is its flexibility to incorporate additional regularizers, allowing applications such as dynamic reconstructions (Mus et al. 2024b), mitigation of scattering effects (Mus et al. 2025), and other enhancements. Nevertheless, the performance of these algorithms remains constrained by the ability of the chosen regularizers to effectively describe the underlying data. Consequently, complex datasets may be inadequately characterized by these methods compared to more advanced techniques such as `kine` (Foschi et al. 2025), which

makes use of deep neural networks. For this work, `MO-PSO` has been developed by incorporating circular polarization and wavelet-based reconstructions, building upon earlier efforts to successfully obtain the first dynamic reconstruction of Sgr A*. `MO-PSO` has already shown excellent performance in less sparse array configurations (Mus 2023), though this study constitutes the most challenging data domain one yet.

Overall, the results are promising. `MO-PSO`: does not hallucinate motion in static source data, avoids producing coherent motion for uncorrelated (jumping) hotspots, recovers the polarization angle correctly and retrieves the position angle accurately in most cases. Although the primary goal was to model the source dynamics, a significant and unexpected improvement was observed within the static reconstructions, especially when compared to previous results plagued by inflated noise in static sources.

Nevertheless, our pipeline still faces some serious limitations when recovering dynamics: the brightness of hotspots is sometimes incorrect, secondary phantom features appear in some of the reconstructions, dynamic components can be noisy or inconsistent and the method still struggles with the kind of complex variability seen in GRMHD simulations. A summary of the results and limitations can be found together with the success rate of our pipeline in Table 2.5. Because of these issues, `MO-PSO` does not fully pass the validation ladder, which is intentionally demanding due to the scientific impact to be derived from this black hole dynamics reconstruction. Despite this, our framework provides critical insights into how assumptions influence imaging results, particularly through the use of `MOEA/D` framework. `MO-PSO` remains the only algorithm that fully explores the multimodality of the posterior, uncovering a range of solutions aligned along a "dynamics axis" from static to super-dynamic reconstructions. This exploration has revealed different clusters of solutions, each fitting certain baselines better than others. One of the main challenges, however, is that the best fit to the data does not necessarily correspond to the best model, which complicates hyperparameter selection. This highlights the importance of testing algorithms on a wide range of synthetic datasets to ensure robustness, rather than relying on a few hand-picked data samples.

Notably, these findings do not imply that imaging the dynamics is impossible, but rather highlight the need for careful tuning of algorithmic flexibility and dynamic modeling capabilities. The tests provided in this work are therefore as necessary as fundamental, offering a unique perspective on both the posterior and the imaging process itself.

`MOEA/D`'s multimodal exploration capabilities have already proven valuable

in past M87 studies, and have now been extended to closure trace fitting and scattering domains, areas where this property is especially important. These remain unique capabilities of the method, with the potential of being particularly important for upcoming EHT observations of Sgr A*at 86 GHz and the first detections of circular polarization in EHT data.

Chapter 3

Helical magnetic field of 3C 273

After focusing on the center of AGNs, we continue exploring the jets launched from them. For that purpose, we focus on a particular source: 3C 273. The content of this chapter corresponds to the article accepted in the research journal Astronomy & Astrophysics (Toscano, Teresa et al. 2025).

3.1 Motivation of Faraday Rotation Analysis

3.1.1 Introduction

Let us remember first the role of magnetic fields in AGN jets. Magnetic fields are considered a dominant factor in the launching, acceleration, and collimation of relativistic jets in AGN (Blandford et al. 2019). Theoretical models suggest that jet formation is driven either by the extraction of energy from a rotating black hole (the Blandford-Znajek mechanism; Blandford & Znajek 1977a) or by magnetic forces acting on material in the accretion disk (the Blandford-Payne mechanism; Blandford & Payne 1982). Both processes require the presence of a structured magnetic field with poloidal (along the jet axis) and toroidal (wrapped around the jet) components. Simulations using general relativistic magnetohydrodynamics (GRMHD) and RMHD (e.g., Fuentes et al. 2018) have shown that the accretion flow around the black hole naturally develops a "spine-sheath" configuration, which may act as a magnetized boundary layer for the jet (Asada et al. 2008; Gómez et al. 2008, 2012).

Moreover, the EHTC performed a detailed theoretical study of a jet-producing AGN system based on GRMHD simulations for M 87 (Event Horizon Telescope Collaboration et al. 2019e, 2021), highlighting the role of Faraday rotation effect in the interpretation of the polarimetric observations of AGN.

Despite the success of numerical simulations in supporting these models, observational evidence for the detailed structure of the magnetic field, particularly its toroidal component, remains scarce (Zamaninasab et al. 2013; Molina et al. 2014; Pasetto et al. 2021; Kovalev et al. 2025a). Observations of linearly polarized synchrotron radiation provide insight into the magnetic field orientation projected on the plane of the sky. The highest resolution linear polarization maps are obtained from VLBI observations (e.g., Boccardi et al. 2017; Hada 2019; Wielgus et al. 2022; Jorstad et al. 2023), which probe the innermost regions of AGN jets. However, on their own, these polarization maps cannot fully constrain on their own the three-dimensional (3D) structure of the magnetic field.

To infer the magnetic field component along the line of sight (perpendicular to the plane of the sky), we take Faraday rotation into account. This effect consists on a rotation (dependent on the wavelength) of the polarization angle of the emission going through a magnetized medium. That is to say, the electric vector position angle (EVPA) is rotated by the (line-of-sight) magnetic field. Thus, the strength and direction of this magnetic field can be inferred through the Rotation Measure (RM), quantifying this rotation and providing information on the magnetized environment of the jet.

Theoretically, the RM is directly proportional to the line-of-sight magnetic field strength ($B_{||}$) and the electron density (n_e) in the medium, integrated along the path length (dy) (Burn 1966):

$$RM = 8.1 \times 10^5 \int n_e B_{||} \mathrm{d}y \tag{3.1}$$

where RM is measured in radians per square meter (rad/m^2), $B_{||}$ is in Gauss, n_e is in cm^{-3}, and dy is in parsecs (pc). Thus, by mapping the RM across a jet, we can investigate the magnetic field structure using different features such as gradients. For example, a smooth transverse gradient in a jet, given that RM is sensitive to the magnetic field's direction, would indicate a continuous change in the magnetic field's direction, which would evidence the existence of a helical magnetic field (Blandford 1988, 1993; Asada et al. 2002; Gómez et al. 2012, 2016; Pasetto et al. 2021).

In the simplest case, assuming a uniform magnetic field external to the jet (Hovatta et al. 2012), the observed EVPA $\chi_{\rm obs}$ is related to the intrinsic EVPA χ_0 and the square of the observing wavelength (λ^2) through the RM as:

$$\chi_{obs} = \chi_0 + RM\lambda^2 \tag{3.2}$$

The quasar 3C 273, at redshift $z = 0.158$ (Schmidt 1963), is an ideal candidate for RM studies due to its brightness and high polarization, also showing in many cases a well-resolved jet structure (e.g., Davis et al. 1985; Conway et al. 1993; Jester et al. 2005; Perley & Meisenheimer 2017). Over the years, it has been the subject of numerous VLBI monitoring campaigns aimed at understanding its jet morphology and magnetic field structure (e.g., Krichbaum et al. 1990; Lobanov & Zensus 2001; Savolainen et al. 2006; Kovalev et al. 2016; Bruni et al. 2017; Lister et al. 2019, 2021).

The first detection of a transverse RM gradient in 3C 273 was reported by Asada et al. (2002), suggesting the presence of a toroidal magnetic field. Later studies have confirmed this finding (Zavala & Taylor 2005; Asada et al. 2005; Attridge et al. 2005), with similar RM gradients observed as well in other AGNs (e.g., Gómez et al. 2012; Gabuzda et al. 2017; Kravchenko et al. 2017), further supporting the notion that jets are threaded by helical magnetic fields (e.g., Gómez et al. 2016).

In this chapter, we present new multi-frequency VLBI observations of 3C 273, focusing on the study of RM maps to better understand the geometry of the magnetic field structure in this source. We compare our results with previous works, offering new insights into the jet's magnetic field structure and evolution. Throughout this work, we assume a cosmology with $H_0 = 71$ km s^{-1} Mpc^{-1}, $\Omega_m = 0.27$, and $\Omega_\Lambda = 0.73$ (Komatsu et al. 2009), where 1 milliarcsecond corresponds to 2.71 pc in projected distance.

3.1.2 Observation and data analysis

The observations presented in this work were conducted on 2014, November 21, using the Very Long Baseline Array (VLBA) as part of an astrometric multi-frequency program (with reference BG216). This program targeted a sample of BL Lacs, flat spectrum radio quasars, and radio galaxies. Due to the astrometric nature of the program, the observing strategy involved alternating scans between the target sources and nearby calibrators at different frequencies. As a result, the scans on the target source were relatively short -typically less than 30 seconds - an approach standard in astrometric experiments to maintain high positional accuracy while minimizing systematic errors introduced by atmospheric or instrumental effects. This strategy, combined with interleaving scans at multiple frequencies, provided comprehensive *uv*-coverage for the sources.

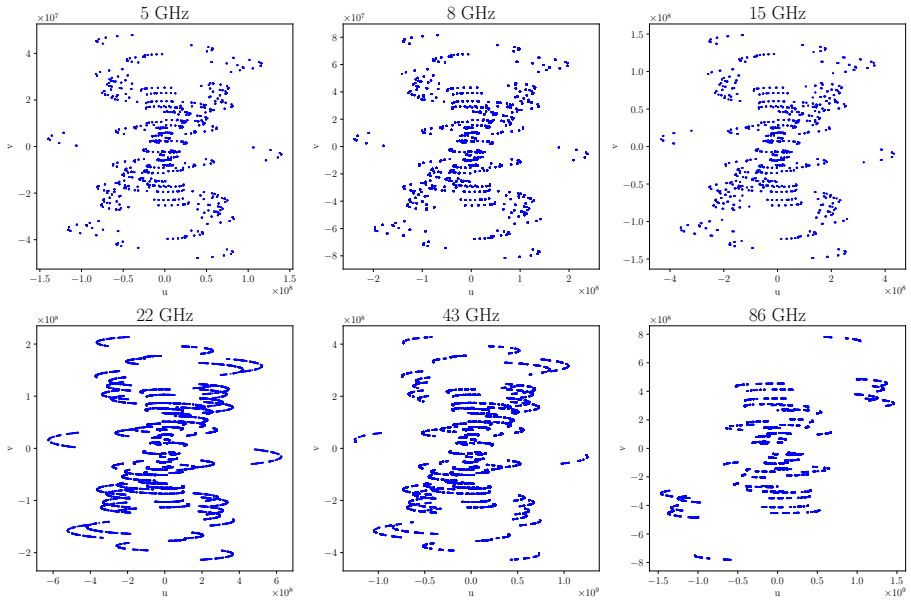

Figure 3.1: Fourier coverages of 3C 273 from VLBA observations at different frequencies.

All 10 VLBA antennas were present during the observation, which spanned six frequencies: 4.98, 8.42, 15.25, 21.89, 43.79 and 87.55 GHz.The data were recorded in 8 IFs of 32 MHz, amounting to 256 MHz total bandwidth per frequency. The on-source time ranged from 10 minutes at the lower three frequencies, to 4h 46m at 22GHz, and 47m at the highest two frequencies. The integration time at 22 GHz is significantly longer because the proposal was originally intended for astrometry, and 22 GHz was used as the reference frequency for regular phase reference and frequency-phase-transfer referencing. A summary of the Fourier coverages of each frequency can be found in Fig. 3.1.

3.1.3 Data reduction

The calibration and processing of the data were performed using the National Radio Astronomy Observatory (NRAO) Astronomical Image Processing System (AIPS; Greisen 2003). Standard procedures for polarimetric VLBI observations were followed for phase and amplitude calibration, as described in the AIPS

Cookbook*. We applied a priori calibration to the correlated visibility amplitudes using system temperature measurements and gain curves specific to each station. Phase calibration was carried out by performing a fringe-fitting procedure on the data, after correcting for the parallactic angle. Additionally, we corrected for phase bandpass, delay, and rate offsets, which resulted in strong fringe detections across all baselines. The calibrator 4C 39.25 was used as a fringe finder and bandpass calibrator for all frequencies except 86 GHz, for which 3C 273 was used instead.

Subsequent data editing was performed interactively using Difmap software (Shepherd et al. 1994; Shepherd 2011) to remove outliers and poor quality data, which could introduce noise or artifacts into the imaging process. The final images were produced through iterative CLEAN deconvolution, ensuring that the imaging process accurately reconstructed the brightness distribution of the source while minimizing noise.

3.2 A transverse gradient across the jet

3.2.1 Polarization and Rotation Measure Calculation

The instrumental polarization calibration (commonly referred to as D-term calibration) was performed using the task LPCAL in AIPS on 3C 273 itself, following the correction for cross-hand delays using the RLDLY task. Once the data are fully calibrated both in intensity and polarization, to calculate the rotation measure it is necessary to first calibrate the absolute electric vector position angle at each frequency by using single-dish measurements or close-in-time observations from monitoring programs on our target source, 3C 273.

For 5 and 8 GHz, we used single-dish data from the QUIVER (Monitoring the Stokes Q, U, I and V Emission of AGN jets in Radio) project, obtained with the Effelsberg radio telescope (Myserlis et al. 2018; Angelakis et al. 2019) in the frame of the F-GAMMA monitoring program. These observations, conducted at 4.85 and 8.35 GHz, were taken 10 days after our VLBA session and yielded EVPA values of $-28 \pm 2^\circ$ and $-36 \pm 2^\circ$, respectively. For 15 and 43 GHz, we obtained the EVPA correction using public data from the MOJAVE (Lister et al. 2009) and BEAM-ME (Jorstad et al. 2017) monitoring programs. We applied the appropriate rotation by comparing our observed EVPAs with these values. For 22 GHz, no single-dish measurements were available, hence to find the appropriate rotation used for the RM map we first corrected 15 and 43 GHz polarization images, we calculated the average EVPA of each map and then, assuming the linear relation mentioned in Sec. 3.1.1, we interpolated the average for the 22

*http://www.aips.nrao.edu/CookHTML/CookBook.html

GHz map in order to apply the corresponding rotation. In this way, we provide a reasonable approximation in the absence of direct data.

The RM maps were generated using data from three frequencies at a time, ensuring consistent *uv*-coverage (same for all three frequencies), pixel size, and image resolution across the different frequencies. For an appropriate comparison between frequencies, higher-frequency images were convolved with the restoring beam of the lowest frequency. Only regions with polarized intensity with a signal-to-noise ratio greater than 4σ (where sigma is the root mean squared (rms) value from Difmap) were used in the analysis. If no polarization was detected simultaneously at all three frequencies, the corresponding RM pixel was blanked in the map.

Image alignment across different frequencies was necessary to compensate for the frequency-dependent positional offset of the VLBI core caused by synchrotron self-absorption (Blandford & Königl 1979). We aligned the images using two-dimensional cross-correlation, following the method described by Walker et al. (2000) and Croke & Gabuzda (2008). After cross-correlation, the cumulative shifts for each frequency relative to the reference (highest frequency) were determined and corrected for, finding that they followed a inverse proportionality to the frequency, consistently the expected trend of a conical Blandford & Königl jet model (Blandford & Königl 1979). Finally, due to the inherent π ambiguity in the EVPAs, π rotations were manually applied to ensure the best fit to the λ^2 law in the RM analysis.

The VLBA antennas are not optimized for observations at 86 GHz, resulting in poor sensitivity at this frequency, both in total intensity and polarized flux. Because of the short observing time and limited sensitivity, the lack of significant polarization as well as the absence of simultaneous single-dish measurements available for calibrating the absolute EVPA, the 86 GHz image was not included in the Faraday rotation analysis.

3.2.2 Results

In this section, we present VLBA polarimetric images of 3C 273 at 5, 8, 15, 22, 43, and 86 GHz (Figure 3.2). The total intensity images are shown with contour lines above the 5σ level, while the EVPAs are overlaid as white ticks. The total polarized intensity is displayed in color, with only pixels above 4σ included in the polarization map; any pixels below this threshold are blanked.

We provide two RM maps derived from observations at 5-8-15 GHz and 15-22-43 GHz, which allow us to investigate the magnetic field structure across different

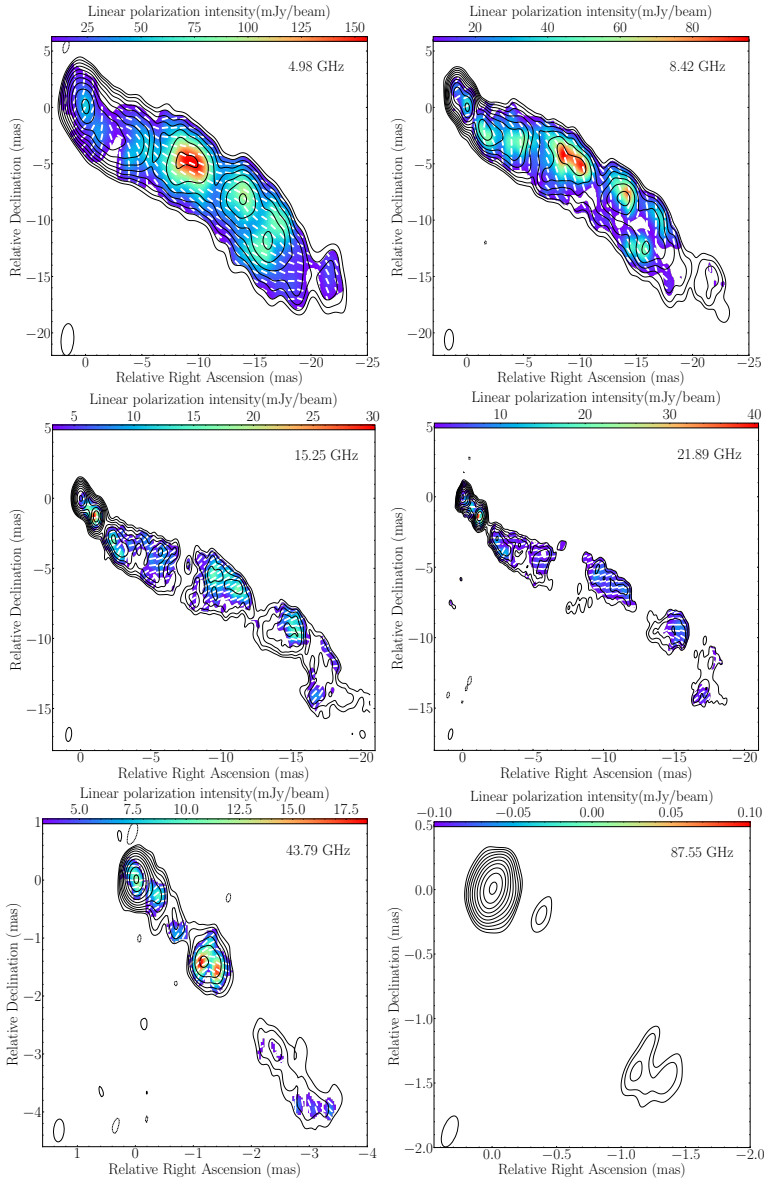

Figure 3.2: VLBA total and linearly polarization images at different frequencies. Contours show total intensity above a threshold of 5σ level, color scale represents the linearly polarized intensity above 4σ level, and white ticks indicate the observed electric vector position angle. The peak value of total flux density is 2.83, 2.67, 1.55, 2.08, 3.89, 2.42 Jy/beam for 5, 8, 15, 22, 43 and 86 GHz, respectively. The corresponding rms is 12.55, 4.01, 1.96, 1.23, 2.64, 5.49 mJy/beam.

regions of the jet (Figure 3.3). Finally, we present images showing transverse sections across the jet at several locations to analyze the asymmetry of the jet in different aspects: the total intensity, the linear polarization intensity and the degree of polarization at 5 GHz (Figure 3.6), and the RM distribution in both RM maps (Figure 3.7).

3.2.3 Maps of Linear Polarization

The total intensity and polarization structure in Figure 3.2 of 3C 273 at different frequencies are consistent with previous observations of 3C 273 (Asada et al. 2002; Zavala & Taylor 2005; Hovatta et al. 2012). Note that at 22 GHz, the image is dynamic range limited, making iit comparable in its noise floor to other bands while having longer integration time. As discussed in subsection 3.2.4 (see also Figure 3.3), the EVPAs are significantly influenced by Faraday rotation, and once corrected, the magnetic field appears to be predominantly toroidal.

The core is located at the northeastern, upstream end of the jet, where linear polarization is significantly reduced, primarily due to opacity and beam depolarization effects. At 5 and 8 GHz, a bright, highly polarized component is visible around 10 mas from the core. This feature fades at higher frequencies, although the overall jet structure remains consistent with archival images from the MOJAVE and BEAM-ME programs. As the core becomes progressively optically thin at 15 and 22 GHz, a new component emerges around 1 mas from the core. Close-in-time MOJAVE observations at 15 GHz and BEAM-ME observations at 43 GHz indicate that this component is moving outward. A comparison with Hada et al. (2016), which used 43 GHz data from February 2014, shows the presence of this component at 1 mas, consisting of two subcomponents referred to as P2 and P3. In our polarization images taken nine months later, these P2 and P3 components appear to evolve and move further downstream from the core.

We also present one of the few images of 3C 273 at 86 GHz, which is consistent with previous observations by Attridge et al. (2005), Hada et al. (2016), Hovatta & Lindfors (2019), and more recently by Okino et al. (2022), which incorporates ALMA data for the first time. Although the sensitivity at this high frequency is limited, the total intensity image plotted in contours reveals the core and the brightness structure (component)around 1 mas, consistent with lower-frequency images. Unfortunately, no significant polarization is detected at this frequency.

3.2.4 Rotation Measure Maps

In this section, we present Rotation Measure maps in Figure 3.3 derived from two frequency sets: 5-8-15 GHz and 15-22-43 GHz, along with their corresponding

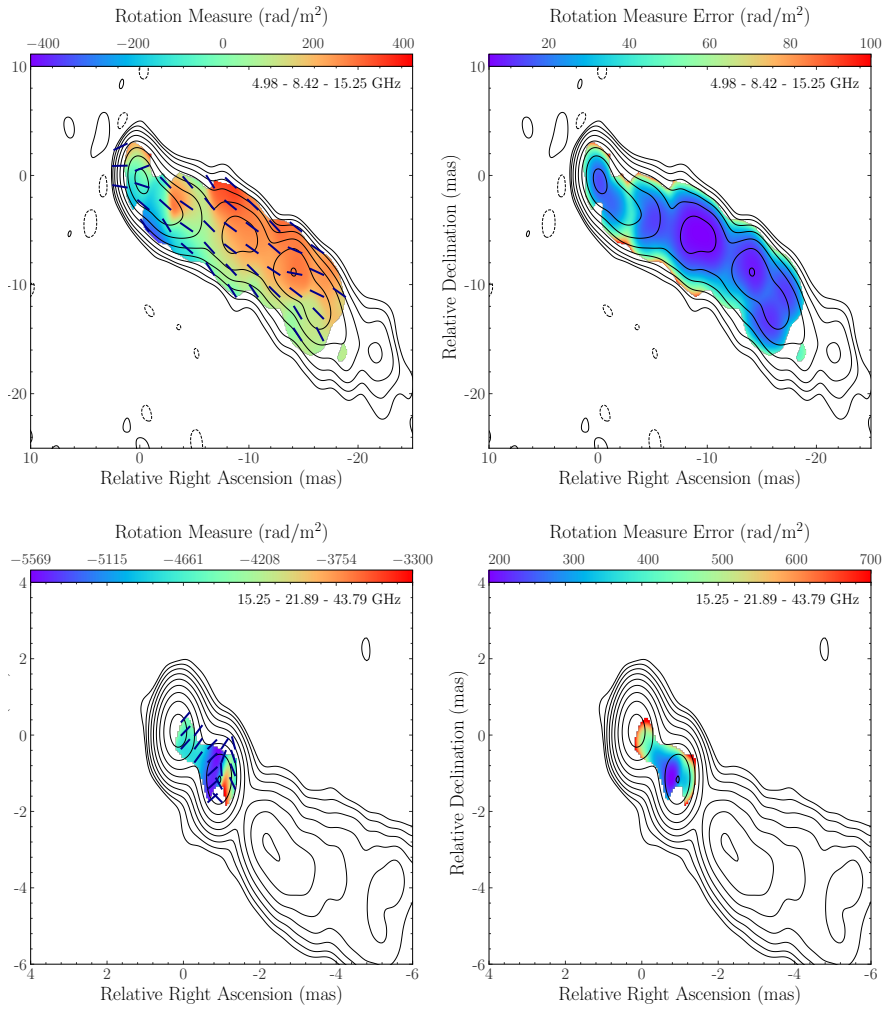

Figure 3.3: Rotation measure maps of 3C 273 using 5-8-15 GHz (left column, top) and 15-22-43 GHz (left column, bottom) and its respective errors (right column). Corrected (intrinsic) EVPAs are plotted as dark blue ticks.

error maps. Previous RM studies (Zavala & Taylor 2001; Wardle 2018; Hovatta & Lindfors 2019) typically utilized only two frequencies for a linear fit. By incorporating three frequencies in our analysis, we achieve a more robust and statistically significant estimate of RM. The goodness of the fit of the linear relation is presented in Fig. 3.4 and 3.5, where in the latter we have used the reduced χ^2 as a metric, as used in Lisakov et al. (2021), blanking pixels that had $\chi^2 > 5.99$ (with 3 data points and 2 degrees of freedom indicates a 95% confidence level). The maps, shown in Figure 3.3, are overlaid with total intensity contours and the RM-corrected EVPAs. The RM error maps have been constructed using the square root of the variance of the parameter estimates from the linear fitting.

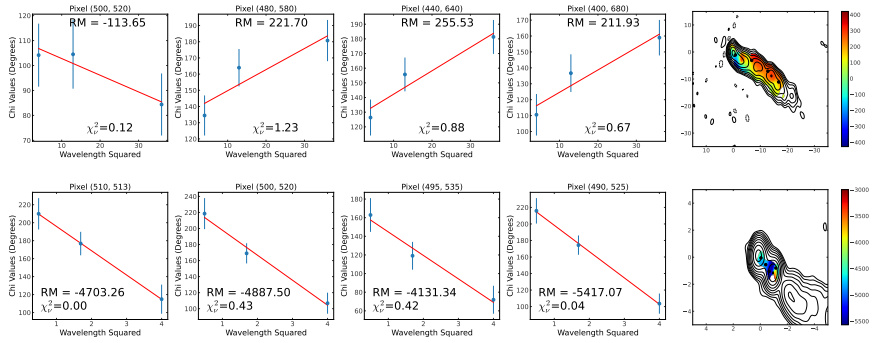

Figure 3.4: Linear fit of 4 pixels in the RM maps, from left to right.

For the first RM map, derived from 5-8-15 GHz observations, the values range from approximately -400 rad m^{-2} to 400 rad m^{-2}, which are consistent in order of magnitude with respect to those reported in previous studies at similar frequencies (Asada et al. 2002, 2008; Hovatta et al. 2012; Lisakov et al. 2021). A clear transverse RM gradient is evident, presenting also a sign change across the jet. That is to say, the different sign at both ends of the gradient are attributed to differences in the line-of-sight magnetic field direction. Thus, it reflects a systematic variation in the magnetized plasma's properties across the jet, consistent with the geometry and structure expected for a persistent helical magnetic field.

As a byproduct of obtaining the RM maps from a linear approximation, we estimate the intrinsic EVPA of the source (i.e. after correcting for Faraday rotation), which corresponds to the y-intercept of the linear regression. Plotted as dark blue ticks, they follow the jet direction, signaling that the Faraday rotation effect is significant (see Figure 3.2 for comparison) and indicating a predominant toroidal component of the magnetic field structure.

In contrast, the second RM map, based on 15-22-43 GHz observations, is limited to the innermost 2 mas of the jet. At these higher frequencies, the core region is closer to the base of the jet, where the line of sight passes through a denser, more strongly magnetized plasma. Consequently, RM values increase significantly (around one order of magnitude), with absolute values exceeding 5×10^3 rad m^{-2}. Such high RM values are common at higher frequencies, with values exceeding 2×10^4 rad m^{-2} reported at 3 and 7 mm (Attridge et al. 2005; Hada et al. 2016), and even reaching 5×10^5 rad m^{-2} in some cases (Hovatta & Lindfors 2019), suggesting a dense Faraday screen or stronger magnetic fields (Savolainen et al. 2008). The larger negative values of the RM seen in the higher frequencies RM are consistent with the lower frequencies RM map, showing also negative RM values for this region. The clear RM gradient seen in the lower frequencies RM is not present in the 15-22-43 GHz map.

Furthermore, as also observed in the lower-frequency RM map, the intrinsic EVPAs in the 15–22–43 GHz RM map appear almost perpendicular to the jet direction, suggesting a dominant poloidal magnetic field near the jet base, as expected in the launching region. Around 1.5 mas from the core, however, the EVPAs transition and become more aligned with the jet, consistent with the trend seen in the lower-frequency RM map. This behavior is in agreement with expectations for a helical magnetic field configuration, where the poloidal component dominates near the launch point, and the toroidal component becomes more significant downstream, contributing to the collimation and stability of the jet.

In order to ensure the linear relation of the rotation measure maps, we show the linear fit for 4 different points in both RM maps in Fig. 3.4 and the same maps displaying the chi squared values to attest to the roboustneses of the fitting in Fig. 3.5.

3.2.5 Asymmetry Across the Jet and the existence of a helical magnetic field

To analyze the transverse jet asymmetry, we trace a ridge line (curve that traces the total intensity along the jet axis) following the method of Fuentes et al. (2023). We apply six evenly spaced transverse sections along this ridge line to examine variations in total intensity, linear polarization and degree of polarization along the length of the jet. Figure 3.6 shows the jet sections (units of the colorbars are displayed in the y-axis of the right column plots). In addition, we also display a second study for rotation measure maps in Figure 3.7, using the same six sections mentioned above for the 5-8-15 GHz RM map, and only one section in the 15-22-43 GHz RM map, coincident with the one closest to the core in the lower frequency

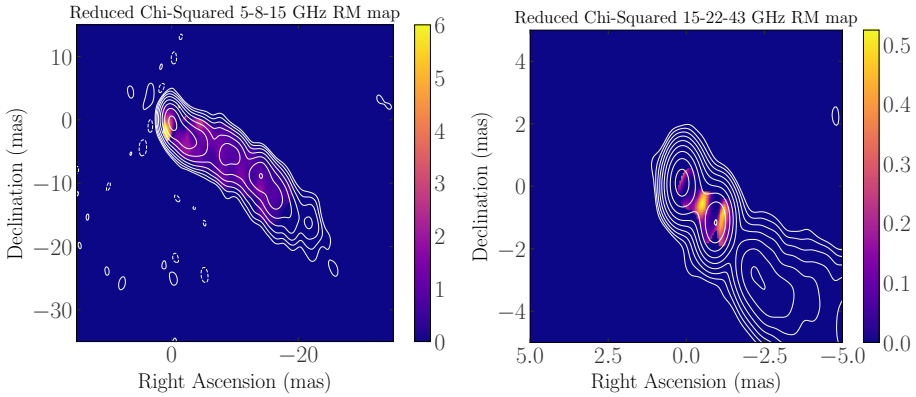

Figure 3.5: Goodness of fit using reduced chi squared values of both RM maps.

RM map.

In Figure 3.6, the intensity image in the first row reveals a clear drop in emission from the first section near the core to the subsequent sections downstream, reflecting the expected decrease in brightness as we move away from the core region. In most of the sections, the northern part of the jet appears consistently brighter than the southern part, suggesting a slight asymmetry in the intensity distribution. This asymmetry, aligns with predictions from relativistic magnetohydrodynamic simulations of jets threaded by a helical magnetic field (Fuentes et al. 2018, 2021).

The linear polarization map at 5 GHz displayed in the second row panels displays that overall, the jet shows more linearly polarized emission close to the spine, decreasing towards the borders. This behavior is especially relevant in the third section, where a highly polarized component is found at 10 mas away from the core, creating a spike reaching almost 140 mJy/beam.

In the degree of polarization map, we observe a stratification across the jet width, with systematically higher values towards the jet edges, as expected for the case in which the jet is threaded by a helical magnetic field (e.g., Gómez et al. 2008). Only the third section in the degree of polarization shows higher values near the jet axis, most likely due to the presence of a strong shock leading to enhanced polarization, as seen in Figure 3.2.

Moving on to the asymmetry of RM maps in Figure 3.7, the first map (5-8-15 GHz, top row) shows a consistent transverse gradient in all sections, extending up to around 18 mas or a projected distance of 45 pc. The gradient is steeper near

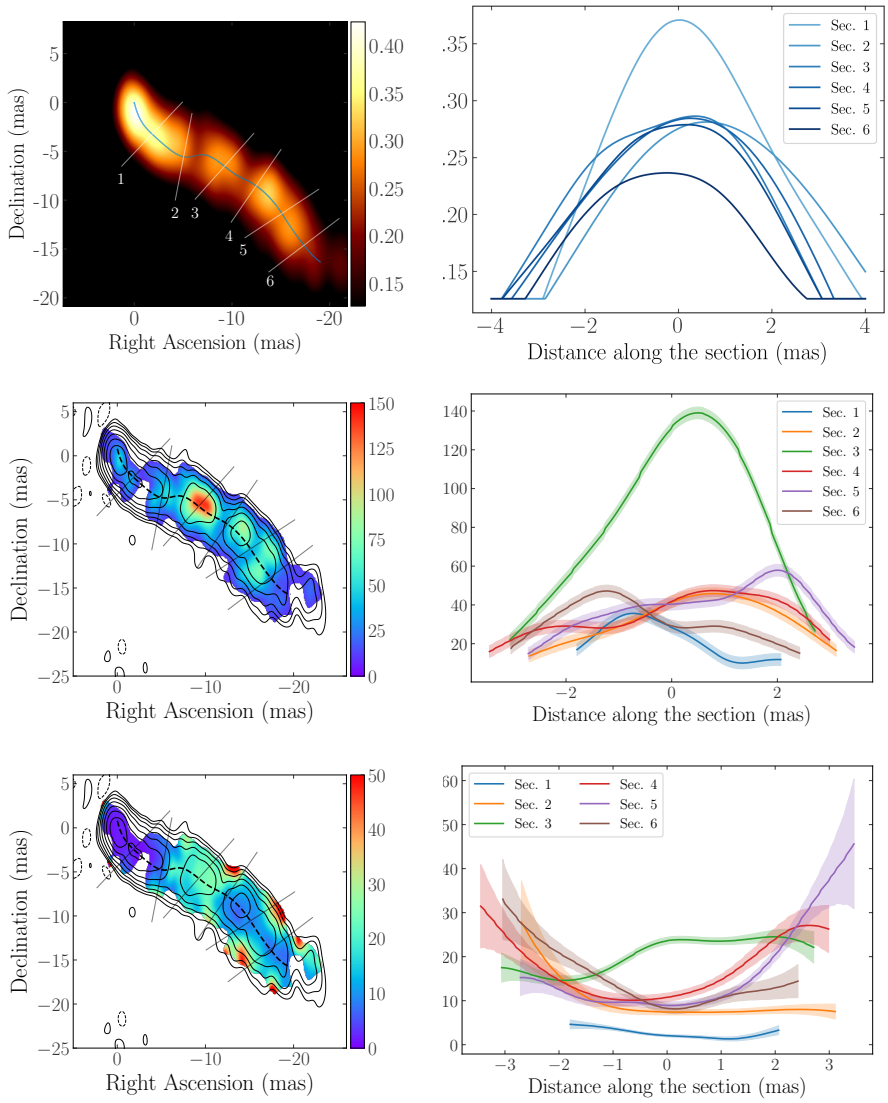

Figure 3.6: Transversal sections for total intensity image at 5 GHz (top row), linear polarization at 5 GHz (central row) and degree of polarization (bottom row). Units displayed in the left column. Order of the sections along the jet are numbered in the total intensity image.

the core, where the stronger magnetic fields result in higher RM values. As we move further downstream, the asymmetry in RM persists, with higher positive values on the northern side and negative values on the southern side. The gradient weakens gradually as we move down the jet but remains detectable. These results agree with previous studies that report stronger RM magnitudes in the nuclear regions of active jets (Asada et al. 2002; Hovatta et al. 2012). The persistent RM gradient suggests a systematic change in the magnetic field along the line of sight.For the second RM map at higher frequencies, the core region shows that the asymmetry is quite less obvious transversely, although there seems to change alongside the jet. The lack of further detection in this region prevents us from making a more thorough analysis.

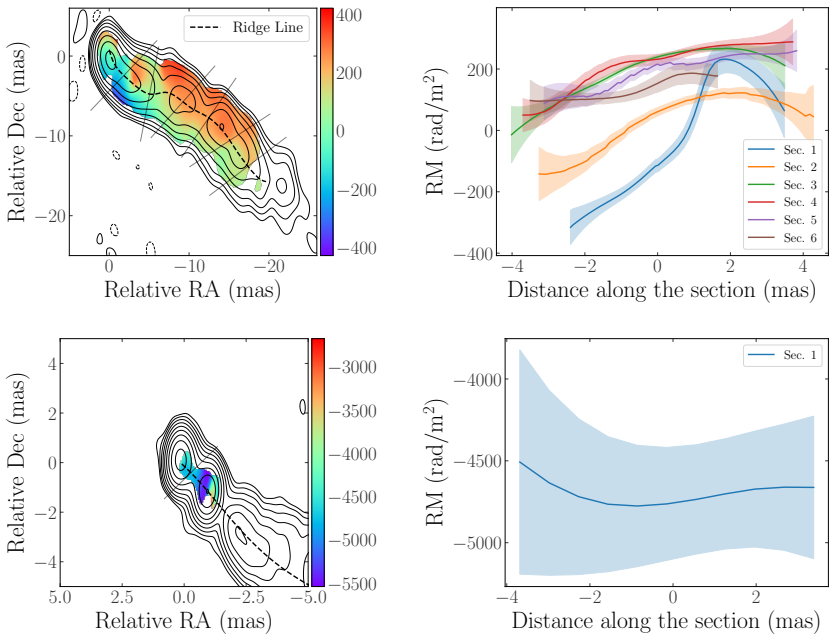

Figure 3.7: Transversal sections for RM map using 5-8-15 GHz (top row) and 15-22-43 GHz (bottom row). Order and values of the sections are displayed from left to right, as shown in Figure 3.6

3.3 Discussion and conclusion

Our observations reveal a clear transverse RM gradient across the jet of 3C 273 (see Figure 3.3) using 5, 8, and 15 GHz, confirming that this feature persists

both in time and along the jet. To contextualize our results, we compare them with previous RM measurements of 3C 273, highlighting both consistencies and differences to map the jet evolution.

Asada et al. (2002, 2008) first reported an RM gradient using observations from 1995 and 2002 at 4.6–8.6 GHz. They measured exclusively positive RM values ranging from approximately 130 to 480 rad m^{-2}. Zavala & Taylor (2005) observed higher RM values using data from 2000 at 12–22 GHz, with RM values ranging from about –50 to 350 rad m^{-2}, predominantly positive. Wardle (2018) compiled these RM measurements and added those by Chen (2005), based on 1999–2000 observations, which were positive and within a range of 200 to 800 rad m^{-2}.

A significant finding by Hovatta et al. (2012) was the detection of a sign change across the transverse RM gradient in 3C 273, using data from 2006 at four frequencies between 8 and 15 GHz. They suggested that this change was due to a different part of the jet being illuminated compared to earlier observations, similar to what was observed in 3C 120 (Gómez et al. 2011). Unlike Zavala & Taylor (2005), who observed mostly constant, predominantly positive RM values, Hovatta et al. (2012) detected rapid RM variations within a three-month time span. The maximum gradient they observed ranged from about –600 to 500 rad m^{-2} at approximately 3–7 mas from the core. This sign change was corroborated in a subsequent study by (Lisakov et al. 2021), using data from 2009 at frequencies of 8.1–15.4 GHz. Their RM values, ranging from –500 to 400 rad m^{-2}, were consistent with those of Hovatta et al. (2012).

A possible explanation for the shift from exclusively positive RM values in earlier observations to a gradient with both negative and positive values in more recent measurements could be the variability in the jet's magnetic field configuration and/or the magnetized medium producing the Faraday rotation. Changes in the illuminated regions of the jet due to evolving emission patterns may cause different cross-sections to be observed, which in turn would be dominated with varying magnetic field orientations and polarization, thus maybe leading lead to the detection of both positive and negative RM values across the jet width.

Additionally, variations in the internal conditions of the jet, such as the electron density or magnetic field strength could modify the effect of Faraday rotation. Also, interactions with the surrounding medium or even changes in the viewing angle due to the jet's curvature may also affect the observed RM values, whether modifying the external Faraday screen or altering the line-of-sight magnetic field. On another hand, new and more refined observational techniques or increased sensitivity could further reveal finer RM structures Therefore, the observed shift likely results from a combination of intrinsic changes in the jet's

properties, environmental interactions, and changes in observational capabilities.

With our 2014 observations at six different frequencies, we examined both the structure and evolution of the polarization of 3C 273, contributing to a more comprehensive understanding of its RM variations. As described in subsection 3.2.4, our RM values range from –400 to 400 rad m^{-2}, consistently demonstrating that the transverse gradient and the sign change are still present.

Contrasting our results with those closest in time, from five years earlier (Lisakov et al. 2021), we observe minor fluctuations in the RM values, although it is complicated to establish an accurate comparison given that in this previous study the RM maps used only two sets of frequencies (4.5-8.4 GHz and 8.1-15.4 GHz) in the analysis.

Both negative and positive values seem to remain within the same area of the jet, not showing a significant variation. We observe that negative RM values have since then slightly decreased in number even if their position has not noticeably changed, staying in the southern side of the jet up to $\sim$ 10 mas. The positive values, on the other hand, have interestingly increased in number, occupying a broader region of the jet and a bigger fraction of the jet width.

The slight increase in the number of positive RM values and their positioning suggest a few possibilities: first, an evolving asymmetry in the density of the magnetized plasma surrounding the jet. This might indicate that either the electron density or the magnetic field strength has increased on the upper side of the jet over time. Second, the change could signal a structural variation in the jet, such as precession, slight bends or changes in viewing angle, altering how the magnetic field is perceived. This last option may be less probable due to the observed stability of the source structure over the years.

The origin of the RM gradient in 3C 273 remains a topic of investigation. Several models have been proposed to explain this phenomenon, broadly categorized into external and internal Faraday rotation scenarios. Asada et al. (2002) suggested that the RM gradient arises from a helical magnetic field external to the jet, serving as an external Faraday screen. Zavala & Taylor (2005) also argued for an external origin, likely a sheath surrounding the jet. They stated that if the high RM values were due to a uniform magnetic field in the sheath, severe depolarization would be expected, which was not observed. Later studies proposed that RM variations are due to changes in the external, slow-moving sheath, explaining RM changes on a timescale of several years (Asada et al. 2008).

On the other hand, other suggested scenarios include as well internal Faraday

rotation Hovatta et al. (2012) based on observed rapid RM changes. Similarly to Asada et al. (2008), Lisakov et al. (2021) proposed that the Faraday-rotating medium is an extensive sheath enveloping the jet, possibly consisting of slow-moving plasma that accounts for the observed RM stability and gradual variations over time. Our results are fully consistent with this model, suggesting that the screen has not changed significantly, especially between 2009 and 2014, and therefore supporting the idea of a relatively stable external Faraday screen. In addition, Lisakov et al. (2021) predicted that if the jet direction changes farther to the south, mostly negative values will be observed, and since we observe that the positive values have increased, it seems that this is not the case. According to our observations, the jet direction is going towards the north, and might go back to have only positive values were it to continue that trend.

The observed EVPAs (see Figure 3.2) are changing from parallel to almost perpendicular to the jet general direction as the frequency changes, while after correcting for the Faraday rotation effect (see Figure 3.3), they show to be mostly parallel to the jet (at lower frequencies). Not only this manifests the important effect of the Faraday rotation, but also indicates that the intrinsic magnetic field is predominantly perpendicular to the jet direction. That is, it has a strong toroidal component.

The presence of a predominantly toroidal magnetic field may contribute to stabilizing the jet flow, as evidenced by the relatively constant structure of this jet over the years, and play a crucial role in collimating the jet and maintaining its stability over large distances from the central engine. The innermost region, though, shows that close to the core the rotation measure values are quite high and negative, and also the EVPAs appear to be rotated almost 90 degrees. This change in direction could be explained by optical thickness, which prevents us from fully visualize the magnetic field structure in the core region.

Polarization images from our observations show a component at around 10 mas that displays an increase in polarization degree with increasing wavelength, probably due to a shock occurring in this region. Additionally, we observe a gradient in the degree of polarization across the jet, with polarization values increasing towards the jet edges (Figure 3.6, third row).

In such a configuration, the magnetic field lines wrap around the jet axis, causing the magnetic field vectors to have different orientations across the jet width. Towards the jet edges, the magnetic field becomes more ordered and aligned perpendicular to the line of sight, resulting in higher observed degree of polarization. In contrast, at the jet center, the magnetic field may be more tangled or aligned along the line of sight, leading to lower polarization degrees.

Nevertheless, in the third section of the jet we observe that instead of a decrease, there is an increase of polarization degree. This is in agreement with the presence of a shock component, which would order or align the magnetic field in that region, therefore resulting in higher values.

Recent advancements made possible by highly sensitive radio telescopes, such as the Atacama Large Millimeter/submillimeter Array (ALMA) and global collaborations like the Event Horizon Telescope, have yielded significant new results at higher frequencies. These advancements provide high-resolution images that illuminate the collimation processes of the jet and its transition from a parabolic to a conical shape (Casadio et al. 2017; Okino et al. 2022).

For instance, following Okino et al. (2022), the semi-parabolic regime extends up to ~ 20 mas downstream from the core, within the acceleration and collimation zone (ACZ), roughly coinciding with the region where the transverse RM gradient is detected, and therefore pointing to the existence of a helical magnetic field in this region (e.g., Marscher et al. 2008; Gómez et al. 2016). Future work involving new multi-frequency polarization as well as rotation measure studies of 3C 273 will surely widen our understanding of the behavior and evolution of this source.

Taking into account all the evidence, our observations in 2014 reveal a well-defined, persistent transverse RM gradient in 3C 273, consistent with previous studies (Asada et al. 2002; Zavala & Taylor 2005; Asada et al. 2008; Hovatta et al. 2012; Hovatta & Lindfors 2019). In particular, we detect both positive and negative RM values across the jet, confirming the presence of a sign-change in the RM gradient five years after it was last observed. Compared to 2009, we find that the distribution of RM has evolved slightly: negative values remain localized in the southern side of the jet, while positive RM values have increased in both number and spatial extent.

This subtle evolution suggests that the Faraday-rotating medium is relatively stable, consistent with a slow-moving external sheath as proposed by Lisakov et al. (2021), albeit possibly undergoing mild changes. The orientation of the EVPAs, predominantly parallel to the jet after Faraday correction, implies a toroidally dominated intrinsic magnetic field, further supporting the presence of a large-scale helical magnetic field structure. Taken together, these findings reinforce the role of ordered magnetic fields in collimating and stabilizing AGN jets (e.g., Hovatta et al. 2012; Gómez et al. 2012).

In conclusion, our work provides new evidence that the RM structure of 3C 273 remains consistent with a sign-change within the transverse gradient, a stable Faraday screen, and a toroidally dominated magnetic field geometry in the jet.

These observations bridge the gap between the 2009 and earlier measurements and reinforce the hypothesis of a large-scale, ordered magnetic field maintained over multi-year timescales.

By conducting further observations with improved sensitivity and resolution, we will be able to better characterize the magnetic field structure and the roles of internal and external Faraday rotation in AGN jets, contributing to a more comprehensive picture of the jet's magnetic field configuration and evolution, as well as the mechanisms underlying jet formation and stability in active galactic nuclei.

Chapter 4

Space-VLBI high-resolution imaging of 3C 279

In the previous chapter, the focus was on a polarization analysis regarding the rotation measure of the source. However, the study of jets can also be approached differently through the reconstruction of high-resolution images. In this line, the content of this chapter is focused on the study of an aforementioned source: 3C 279, using observations at 22 GHz with the space-VLBI mission *RadioAstron*. The results of this work will be presented in an upcoming publication.

4.1 The blazar 3C 279: An overview

The blazar 3C 279 (1253−055) at redshift $z = 0.536$ (Marziani et al. 1996) is a bright, highly polarized and well-monitored source, one of the first objects to provide evidence of rapid structure variability (Knight et al. 1971) and apparent superluminal motions in compact active galactic nuclei (AGN) jets (Whitney et al. 1971; Cohen et al. 1971). Since then, the structure of the jet in 3C 279, comprised of a compact core and a jet extended from sub-parsec to kiloparsec scales, has been thoroughly studied across the whole accessible electromagnetic spectrum, showing high variability and frequent flares. The core of 3C 279 has a high brightness temperature at centimeter wavelengths (e.g., $\gtrsim 10^{12}$ K in Kovalev et al. 2005), as well as a high fractional linear polarization in the jet ($\gtrsim 10\%$, Pushkarev et al. 2023). In the extended jet, different components show a wide range of apparent speeds (from a few to $\sim$ 20c) and a bulk Lorentz factor in the range of $\Gamma \sim 10$–40 (Bloom et al. 2013; Jorstad et al. 2017; Weaver et al. 2022), suggesting the presence of features associated with propagating shocks or instabilities.

Studying the formation, acceleration or collimation of relativistic jets, together with their connection with the supermassive black hole (SMBH), continues to be one of the most extensive pursuits in modern astrophysics (see, e.g., Boccardi et al. 2017; Blandford et al. 2019, and references therein for recent reviews). Different theoretical models have been proposed to interpret this connection, mainly represented by two scenarios (not mutually exclusive), which suggest that either relativistic AGN jets are driven by the conversion of the rotational energy of the black hole (BH) to Poynting flux via magnetic field lines, which are attached to the BH ergosphere (Blandford & Znajek 1977a), or that these jets are instead driven by strong magnetic fields anchored onto the BHs accretion disk (Blandford & Payne 1982).

Very Long Baseline Interferometry (VLBI) is a powerful technique that provides great angular resolution, enabling us to resolve and analyze the fine structure of extragalactic jets on (sub-)parsec scales. By observing at higher frequencies or extending the baseline length of the array elements, VLBI enables the study of jet features located at $\sim 10^3$ Schwarzschild radii from the central engine for a number of AGN sources. In particular, polarimetric VLBI observations play a crucial role in studying extragalactic jets, providing essential insights into jet physics and the configuration of magnetic fields (e.g., Gómez et al. 2001, 2016; Gabuzda 2021; Gómez et al. 2022).

Different monitoring campaigns, like BEAM-ME (Jorstad et al. 2017) and MOJAVE (Homan et al. 2021; Lister et al. 2021) have successfully and extensively observed these objects at millimeter and centimeter wavelengths, respectively. In fact, the MOJAVE program, monitoring at 15 GHz, has reported maximum apparent speeds up to $\sim 20c$, consistent with a jet oriented at a small angle to the line of sight and moving with a Lorentz factor around $\Gamma \sim 13$ (Lister et al. 2019). Similarly, BEAM-ME at 43 GHz has observed component speeds ranging from $\sim 4c$ to $\sim 21c$ (Jorstad et al. 2017). Other findings using the Very Long Baseline Array (VLBA) have reported a dramatic change in the trajectory of a superluminal component (C4), as well as apparent projected speed and direction, moving with a Lorentz factor ~ 15 suggesting that the trajectory change is a collimation event occurring at around 1 kpc (deprojected) from the core (Homan et al. 2003).

The Event Horizon Telescope (EHT) composed of mm-wavelength radio telescopes distributed over the globe provided the first images of BH shadows with the sharp resolution of $\sim 20\,\mu$as (Event Horizon Telescope Collaboration et al. 2019a, 2022a).

The EHT has also imaged 3C 279, presenting the first 1.3 mm VLBI images

at the extreme angular resolution of 20 μas (Kim et al. 2020a). Their results reveal a multicomponent inner jet morphology with the northernmost component elongated nearly perpendicularly to the direction of the jet, separated from the other component by ~ 100 μas. This is interpreted as either a broad resolved jet base or a spatially bent jet, with low apparent ($T_{b,\,obs} \lesssim 10^{11}$ K) and intrinsic brightness temperatures ($T_{b,\,int} \leq 10^{10}$ K).

The *RadioAstron* space VLBI mission (Kardashev et al. 2013), specifically designed to study of ultra compact regions in space objects (Kovalev et al. 2020), operated between 2011 and 2019. Led by the Astro Space Center of Lebedev Physical Institute and the Lavochkin Association, this mission featured a 10 m radio telescope on board the *Spektr-R* satellite, equipped with dual polarization receivers operating at 0.32 GHz (P band), 1.6 GHz (L-band), 4.8 GHz (C-band), and 22 GHz (K-band). With an apogee close to 350,000 km, the observations with *RadioAstron* enable the imaging of blazar jets in both total and linearly polarized intensity with unprecedented resolution, that is, of the order of few tens of microarcseconds (e.g., Lobanov et al. 2015; Gómez et al. 2016; Giovannini et al. 2018; Vega-García et al. 2020; Bruni et al. 2021; Gómez et al. 2022; Savolainen et al. 2023).

The launching, collimation, and magnetic field properties of AGN jets have been studied as part of AGN Imaging Key Science Programmes (KSP), complemented by the AGN survey on the brightness temperature of their cores (Lobanov 2015; Gómez et al. 2016; Kovalev et al. 2016). The *RadioAstron* Polarization KSP has constantly collected data throughout the whole duration of the space VLBI mission, successfully probing the regions of the jet closest to the core, as well as their magnetic field, for a sample of the most energetic blazars. Results of the *RadioAstron* mission can be found for several sources such as BL Lac (Gómez et al. 2016), 3C 84 (Savolainen et al. 2023) or OJ 287 (Gómez et al. 2022; Cho et al. 2024, Traianou et al. 2025, submitted), among others. The blazar 3C 279 was among the sources included in the *RadioAstron* Polarization KSP, yielding the first robust detection and imaging of a filamentary structure of the jet (Fuentes et al. 2023).

Results from Fuentes et al. (2023) show, for the first time, the presence of filaments in the 3C 279 radio jet. These bright filaments are suggested to be compressed regions with enhanced gas and magnetic pressure, likely as a result of Kelvin-Helmholtz (KH) instabilities. Moreover, these filaments exhibit periodic structures and brightness variations attributed to Doppler boosting. This periodicity also matches features observed at 7 mm (Jorstad et al. 2017; Weaver et al. 2022) and likely originates from an elliptical surface mode in a kinetically dominated cold jet. In addition, the source polarization signature discussed in

their work indicates the presence of a toroidal magnetic field rotating clockwise along the flow with a pitch angle of $-45°$ and an estimated bulk Lorentz factor of ~ 13 (Jorstad et al. 2005a; Fuentes et al. 2023).

Table 4.1: List of observing radio telescopes.

Array	Station	Code	Diameter (m)
	Mopra	MP	22
LBA	Narrabri (ATCA)	AT	22 (×6)
	Ceduna	CD	30
	Tamna	KT	21
KVN	Ulsan	KU	21
	Yonsei	KY	21
	Tianma	T6	65
	Badary	BD	32
	Hartebeesthoek	HH	26
	Metsähovi	MH	14
EVN	Medicina	MC	32
	Effelsberg	EF	100
	Svetloe	SV	32
	Zelenchukskaya	ZC	32
SRT	Spektr-R	RA	10

Here, we present an investigation of 3C 279 at 22 GHz using *RadioAstron* observations of this source performed on January 15, 2018, to explore the jet structure, polarization and time evolution of the filamentary structure previously detected in the 2014 observations (Fuentes et al. 2023).

In the following sections, we present the total intensity and polarization images of 3C 279 at 22 GHz obtained with the space-VLBI mission *RadioAstron*, obtained with the data described in Sec. 3.1.2. Moreover, a supplementary study is introduced in different subsections showing the relation with gamma-rays (Sec. 4.2.1), tests on synthetic data (Sec. 4.2.2), brightness evolution from the public BEAM-ME 43 GHz VLBA data (Sec. 4.2.3), as well as a comparison with the previous *RadioAstron* data from 2014 (Sec. 4.2.4) and a brightness temperature analysis (Sec. 4.2.5).

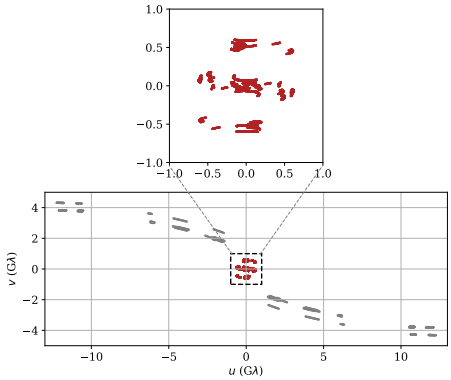

Figure 4.1: Fourier coverage of the fringe-fitted interferometric visibilities of 3C 279, observed by *RadioAstron* on 2018, January 15 at 22 GHz. The color range indicates the lower limit of the observed brightness temperature as per Lobanov (2015).

4.1.1 Observation and data analysis

The observations (project code: GG083B) were carried out on 2018 January 15 using 14 ground-based radio telescopes and the *RadioAstron* space radio telescope (see Table 4.1) at a frequency of 22.22 GHz (1.3 cm, K-band). The polarization calibration was carried out with the source 3C 279 (see Sec. 4.1.3). The observations were carried out in two sessions with two distinct antenna arrays, spanning from 00:49:50 UTC on January 15 to 00:30:45 UTC on January 16 2018, with a four-hour gap (from 10:00 to 14:00 UTC) during which no observations were made.

The data were recorded in both left (LCP) and right (RCP) circular polarization, using 4 intermediate frequencies (IFs) with a recorded bandwidth of 16 MHz each (i.e., a total bandwidth of 64 MHz) for all stations, except BD, SV, ZC, and *RadioAstron*, which operated with 2 IF bands (i.e., a total bandwidth of 32 MHz). On the ground, data were sampled using 2-bit sampling, while RadioAstron used 1-bit. This difference affects the overall sensitivity and data rates of the observations.The *uv*-coverage of the observations is displayed in Fig. 4.1.

4.1.2 Data Reduction

The raw data were correlated at the Max-Planck-Institute for Radio Astronomy using the *RadioAstron* dedicated version of the DiFX software correlator (Bruni et al. 2016). Initial data calibration and processing were performed using the

NRAO Astronomical Image Processing System (AIPS; Greisen 2003), employing the `ParselTongue` interface (Kettenis et al. 2006), calibrating first the ground array and then adding the space antenna.

The gap during the observation naturally led to splitting the data into two subsets for separate calibration. For each subset, the same calibration process was applied, correcting for the parallactic angle and opacity for the ground stations.

An a priori calibration of the correlated visibility amplitudes was performed based on the system temperatures and gain curves recorded at each station. Since six ground antennas (AT, BD, CD, SV, T6, ZC) did not provide system temperature information, we used the default (average) nominal values provided by each station and modulated them by the antenna's elevation at each scan. We then solved for residual single- and multi-band delays, phase offsets, and phase rates by fringe-fitting the data using AIPS's task FRING.

In the initial stage, we calibrated first only the ground array, and a global fringe fit with an exhaustive baseline search was performed on the ground array with a solution interval of 60 seconds. EF and T6 served as the reference antennas for the first and second data subsets, respectively.

Once the ground array was calibrated, we accounted for the lower sensitivity of the longest projected baselines by adopting different solution intervals (60s and 120s) and combining IFs and polarizations. Afterwards, to enhance fringe detection sensitivity on the longer *RadioAstron* space-ground baselines, we coherently phased the ground array, aligning the phases of the individual antennas to improve the signal-to-noise ratio and sensitivity of potential fringe detections (Gómez et al. 2016; Bruni et al. 2016; Fuentes et al. 2023).

With a signal-to-noise ratio cut-off of 4, reliable ground-space fringes were detected in the first subset at projected baseline distances of up to around 8 Earth diameters providing a maximum angular resolution of 26 μas with a beam of 188 $\times$ 26 μas and orientation $\sim$ 21 degrees from North to East, transverse to the jet direction. For the second subset, with the longest baselines, we detect fringes only at the AT-RA baseline with projected length up to almost 13 Earth diameters, meaning no closure phases could be used. Alas, with a signal-to-noise ratio below 4, these detections were not used for the imaging.

Finally, we solved for the antennas' bandpasses and corrected the delay differences between polarizations using the AIPS task RLDLY. Both subsets were at last unified into a single one using AIPS's task DBCON.

After the calibration was completed, the data were carefully edited using Difmap (Shepherd et al. 1994; Shepherd 2011) in order to flag outliers that could potentially introduce noise and/or create artifacts during imaging.

The instrumental polarization (D-terms) were iteratively obtained using the `eht-imaging` software library (Chael et al. 2016a, 2018a), in the same way as previous work by Fuentes et al. (2023), by using 3C 279 as a calibrator. Absolute calibration of the electric position vector angle (EVPA) was applied using single dish observations from the Effelsberg telescope, on the same day as our observations, of value 25.1 ± 1.8 degrees. The error in the EVPA calibration is estimated to be around 10 degrees.

4.1.3 Imaging strategy

Imaging was carried out using the `eht-imaging` software library (already introduced in Sec. 1.4.3.2), a regularized maximum likelihood (RML) method (Chael et al. 2016a, 2018a). While CLEAN algorithm (Högbom 1974; Shepherd et al. 1995) has been widely used in the past for VLBI image reconstruction (Gómez et al. 2022; Cho et al. 2024), RML methods can provide increased resolution over CLEAN, naturally incorporating both physical and prior constraints and showing better capabilities to super-resolve the source structure. Their superior resolution and fidelity make them ideal for sparse VLBI arrays. For instance, `eht-imaging` has been widely tested within the EHT collaboration at mm-wavelengths, and it also provides successful results for centimetre wavelengths and space VLBI experiments (Event Horizon Telescope Collaboration et al. 2019d; Kim et al. 2020a; Event Horizon Telescope Collaboration et al. 2022c; Fuentes et al. 2023; Cho et al. 2024).

In general terms, RML methods try to obtain an image (I) in total intensity by minimizing an objective function J defined as follows:

$$J(I) = \sum_{\text{data terms}} \alpha_D \chi^2_D(I, V) - \sum_{\text{reg. terms}} \beta_R S_R(I), \tag{4.1}$$

where D and R are a set of selected data products and regularization terms, respectively, and α_D and β_R are hyperparameters that weight the contribution of the image fitting to the data terms χ^2_D, and the image-domain regularization terms S_R, to the minimization of the previous equation.

This imaging approach can use closure data products (closure phases and log closure amplitudes) together with complex visibilities, providing an observable

that is not affected by station-based errors in the image, while CLEAN is only able to use closure quantities for self-calibration but not for imaging. The significant number of radio telescopes participating in the observation allowed the use of closure quantities which proved to mitigate atmospheric phase corruption and gain uncertainties.

The use of regularization terms also implies that certain features can be enhanced and imposed, such as smoothness between adjacent pixels or similarity to a prior image. Unlike fully Bayesian methods, RML techniques do not estimate the posterior distribution of the underlying image, but instead compute a single image that minimizes Eq.4.1.

For our particular dataset, before the imaging took place, we cut the edge channels, ending up with a bandwidth of 14.5 MHz for each IF. We also performed an initial phase-only self-calibration to a point source model for every point and coherently averaged the data in 120 second intervals using Difmap, a standard procedure to stabilize visibility phases in time while fully preserving the closure phase structure. We also checked that during the process of self-calibration the SNR of the data was sufficiently high in order to avoid generating spurious signal (Popkov et al. 2021; Savolainen et al. 2023).

Imaging the data requires several steps. First, in order to obtain a ground-only total intensity (Stokes I) image, we flagged all baselines to *RadioAstron* and imaged the data collected only by ground radio telescopes. Additional systematic uncertainty for each visibility, 1.5% of the visibility amplitude, was added in quadrature to the thermal noise to account for non-closing errors. The pipeline was initialised with a Difmap CLEAN model of the data (see Fig, 4.2), which provided better results than the typically used Gaussian prior. This CLEAN model was created using only the first subset of data averaged 120 seconds and several rounds of cleaning and self-calibration at every data point. This subset contained most of the short and middle-length baselines, allowing for a rough estimation of the source structure. This way, it provides a better starting point for the `eht-imaging` imaging pipeline and, therefore, it helps the algorithm converge, preventing it from getting caught in local minima.

As mentioned above, we had poor a priori amplitude calibration caused by missing system temperature measurements for some ground antennas. This led us to perform an initial round of imaging using only closure quantities (closure phases and log closure amplitudes) to constrain the image likelihood via the mean squared standardized residual (χ^2). In this step we used the following weights for data terms and regularizers: cphase: 100, logcamp: 100, flux:1e4, l1:10, simple:0, tv:1. This approach yielded values close to one (1.16 for complex visibilities, 1.00

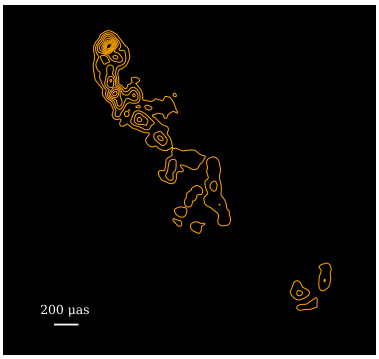

Figure 4.2: CLEAN model in contours of 3C 279 *RadioAstron* 2018 observations using Difmap and plotted using a Python script. Contours are plotted at levels of 0.1 to 0.9 times the peak brightness, in steps of 0.1.

for closure phases, and 0.78 for closure amplitudes), indicating a good fit to the data. The total flux density in the final image was fixed to 10.2 Jy, a value measured as the average of the KVN baselines, the shortest ones available in our observations.

Each imaging iteration took the image reconstructed in the previous step blurred to the nominal resolution of the ground array (that is, 223 μas). Then, we did self-calibration fitting only phases to the closure-only image, and repeated the imaging but incorporating full complex visibilities. Here, the weighting of the data terms and regularizers are: cphase: 100, logcamp: 100, vis:20, flux:1e4, l1:10, tv:1, simple:1.

We then repeated the process, this time using the ground-array image as both the prior and the initial model for the algorithm, after blurring it to match the nominal resolution of the full array restored data (including *RadioAstron* baselines.

That is, first imaging using only closure quantities (using cphase: 100, logcamp: 100, flux:1e4, l1:10, simple:0, tv:10), then applying self-calibration using only phases, and finally adding complex visibilities in the data term in several iterations, progressively increasing their weight in each of them (using cphase: 100, logcamp: 100, vis:50, flux:1e4, simple:10, tv:1 in the final iteration). We only included amplitude self-calibration in the final iteration step. To ensure the robustness of the reconstruction, we also performed a parameter survey using different combinations of the regularizers (see Fig. 4.3), finding a similar structure in all reconstructions.

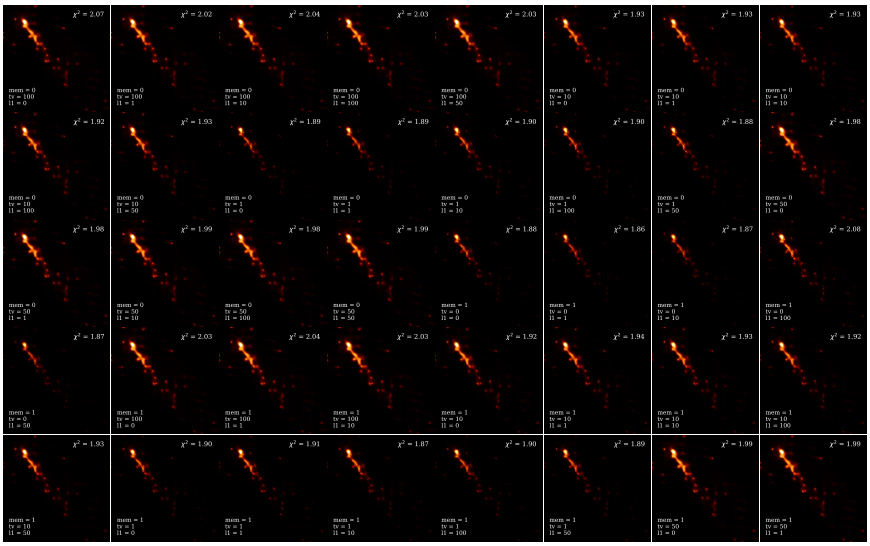

Figure 4.3: Parameter survey of 3C 279 *RadioAstron* 2018 displaying similar morphology. Visibilities χ^2 values are at the top right of each image, and the regularizer combination at the bottom left.

Once the total intensity image was produced, we simultaneously estimated the D-terms iteratively for each station using the `eht-imaging` library, similar to other published works (Event Horizon Telescope Collaboration et al. 2021, 2024c; Fuentes et al. 2023). blazar

4.2 Searching for filamentary evolution

In this section, we present the last total intensity and polarization images of 3C 279 at 22 GHz obtained with the space-VLBI mission RadioAstron, using a single epoch from 2018, January 15. Moreover, a supplementary study is introduced in different subsections showing tests on synthetic data, BEAM-ME archival data brightness evolution, as well as a comparison with the previous RadioAstron data from 2014 and a brightness temperature analysis.

In Fig. 4.4, the total intensity and linearly polarized images of 3C 279 from 2018 January 15 are displayed, showing a field of view of about 2 x 2 mas, a beam of $26 \times 188\,\mu as$ and a total flux density of 10.2 Jy (see Sec. 4.1.3). The radio morphology of this source is known to contain a bright compact core and

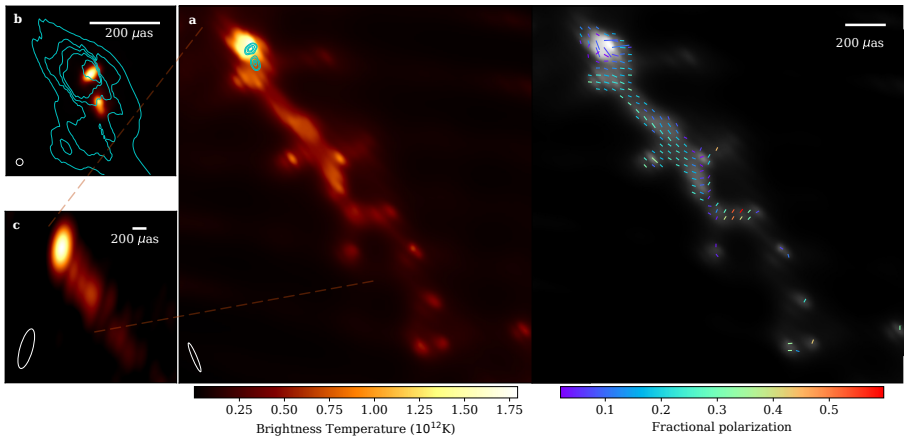

Figure 4.4: Jet structure of 3C 279 revealed by *RadioAstron*. a:Total intensity (left) and linearly polarized (right) *RadioAstron* image at 22 GHz obtained on 2018 January 15 on. Both images show brightness temperature in color scale, though the image on the right also shows the recovered electric vector position angles overlaid as ticks. Their length and color are proportional to the level of linearly polarized intensity and fractional polarization, respectively. b: The EHT image at 230 GHz obtained in April 2017 at 1:1 scale and aligned to our *RadioAstron* image -in contours- using their respective pixel with maximum brightness. Contours are equally spaced in 7 levels within the data range. c The 43 GHz close-in-time image from BEAM-ME program from Feurbary 2018. White ellipses at the bottom-left corners show the convolving beams. Bottom colour bars refer only to information displayed on a.

a thin jet (de Pater & Perley 1983), like we also observe. The core is located at the northeast of the image, as the brightest region, followed by the jet's extended emission in an approximately narrow, straight line that ends with some diffuse emission. This morphology is consistent with previous observations and public data (Lister et al. 2018; Kim et al. 2020a; Fuentes et al. 2023).

The core region displays a bend towards the South of almost 90 degrees connecting with the rest of the straight emission, similar to the structure found in 2014. At around 1 mas from the core, the extended jet shows a gentle curve towards the southwest, coincident with the region where the filament was observed in 2014 but slightly further away from the core (see also Fig. 4.9). No filamentary structure has been detected for our 2018 epoch, though. However, the similarities in structure hint towards the existence of a possibly more complex structure

that is not showing in this particular epoch, maybe due to the sparsity of the uv coverage and the decrease in brightness of the source (see Sec. 4.2.2 for more detail).

Fig. 4.4 also allows us to study the polarized structure of the source. The EVPA direction (plotted as overlayed ticks that vary in length and color, which are proportional to the level of linearly polarized intensity and fractional polarization, respectively) appears to be mostly following the direction of the jet, suggesting that the magnetic field in the jet has a predominant toroidal component in the plane of the sky (relativistic effects are assumed not to strongly influence the perpendicular direction between electric and magnetic fields direction).

At the core, EVPAs show a less organized distribution. As for the rest of the emission, it mostly shows an EVPA orientation parallel to the jet direction, as in 2014 observations (Fuentes et al. 2023), therefore in agreement with a dominant toroidal magnetic field.

Fig. 4.4 also shows BEAM-ME (43 GHz) close-in-time and EHT (230 GHz) 2017 observations at the bottom left and top left of the figure, respectively. The data from the monitoring program MOJAVE at 15 GHz are also available but too far apart in time (4-5 months) to be considered for this rapidly changing source.

When comparing our observations to the BEAM-ME VLBA data at 43 GHz from close-in-time observations, we can see that not only the general total intensity structure and jet direction remains the same with respect to the one we found, but also the polarization. EVPAs from 43 GHz are found to be oriented along the jet direction on pc scales, indicating a magnetic field mainly perpendicular to the relativistic jet (Jorstad et al. 2005a).

From the EHT image taken 9 months prior to our observations (Kim et al. 2020a), we can see how the double structure found in the core fits consistently within the one we found (plotted in contours in the top left panel). The core shift between both frequencies is ignored for the alignment.

4.2.1 Gamma-ray flaring activity in 2018

As a very active and variable blazar, 3C 279 is also a powerful gamma-ray source and the first one showing strong and rapid variability at GeV energies (Hartman et al. 1992). It is also the first flat-spectrum radio quasars (FSRQ) detected above 100 GeV (MAGIC Collaboration et al. 2008).

After several high-energy flares in 2013 and 2015, in 2018, 3C 279 became very

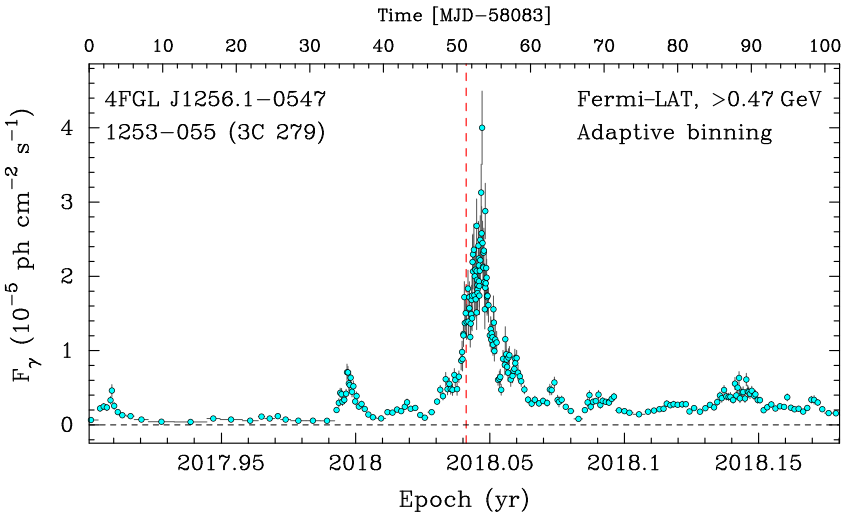

Figure 4.5: Gamma-ray light curve of 3C 279 (positionally associated with 4FGL J1256.1-0547) constructed from Fermi-LAT data using adaptive binning (Lott et al. 2012) with a constant relative uncertainty on flux of ∼15% in each bin. The vertical red dashed line indicates the epoch of *RadioAstron* observations on 15 January 2018, which coincides with the rising phase of a prominent short-duration (6.8 days) flare reaching a peak of $4.0 \cdot 10^{-5}$ ph cm^{-2} s^{-1} ($2.4 \cdot 10^{-8}$ erg cm^{-2} s^{-1}) on January 18, 2018

.

active again, with fluxes exceeding the previous 2015 values. Several studies have been carried out on the January 2018 gamma-ray flare, either focusing on the high-energy correlation between multi-wave bands with hour binned light curves (Shah et al. 2019; Prince 2020; Goyal et al. 2022), particle acceleration or on magnetic reconnection mechanism (Wang et al. 2022; Tolamatti et al. 2022).

The flare reached its peak on Jan 18, 2018 (Shukla & Mannheim 2020), three days after the RA observation. The peak of this flare went up to $4.0 \cdot 10^{-5}$ ph cm^{-2} s^{-1}, which corresponds to 0.0152 MeV/cm^2/s ($2.4 \cdot 10^{-8}$ erg cm^{-2} s^{-1}). The flare duration inferred as the FWHM of the fitted Gaussian is $\sim$ 6 days. This event can be compared to two previous major flares of 3C 279: the June 2015 flare, which peaked at $(3.91 \pm 0.25) \cdot 10^{-5}$ph cm^{-2} s^{-1} (Paliya 2015) with sub-day variability, and the December 2013 flare (Paliya et al. 2016), characterized by extremely fast and intense sub-flares lasting only a few hours, with a very hard gamma-ray spectrum. While the 2018 flare reached a photon flux comparable to the 2015 event, its smoother and longer evolution stands in contrast to the shorter

and more rapidly variable behavior seen in the 2013 and 2015 flares.

Our observations are quite close in time with respect to the gamma-ray flare detected in January 2018. In fact, according to the Fermi database, our observations took place while the flare was in the rising (Fig. 4.5). Based on multifrequency analysis presented in Mohana et al. (2023), 3C 279 radio light curve seems quite flat around the moment of our observations (both at 22 GHz and 43 GHz, as can be seen in Fig. 4.8), and does not perceive an increment in flux density until the end of 2020. Thus, the high values reported for the January 2018 gamma-ray flare do not show a visible impact or correlation with our observations, similarly to the flares in 2013 and 2015, which also show no correlation with the radio band.

4.2.2 Synthetic data

Previous observations from Fuentes et al. (2023) were able to detect a filamentary structure. Therefore, it is natural to ask whether the reason for the lack of detection of these filaments in our observations lies behind the natural evolution of the source or elsewhere, such as the sparsity of the uv-coverage. In order to answer this question, we apply a similar methodology as in Fuentes et al. (2023) and carry out tests using the same synthetic data model.

The synthetic data in Fig. 4.6 represent a couple of intertwined filaments forming a rotated-eight shape in a field of view of 1.3 × 1.3 mas. By using `eht-imaging` we can simulate observations of the ground truth image under the same conditions of a certain observation. That is to say, using the same baselines, thermal noise, phase corruption, and gain uncertainties from the stations. In this case, we perform this test with data from two different uv-coverages: our epoch from 15 January 2018 at 22GHz and BEAM-ME epoch from 17 February 2018 at 43 GHz, each displayed in a different row.

For all datasets, the same approach has been used in the imaging reconstruction, using either only closure quantities (closure phases and log closure amplitudes) or a combination of a first image with only closures, then doing self-calibration and adding complex visibilities.

In Fig. 4.6, in the first row, we show the results with our *RadioAstron* data. When we use only closure quantities, the reconstruction takes the shape of a roughly straight line in the right direction but shows no sign of filaments. When adding visibilities, the reconstruction marginally improves, but it is still not possible to discern any loops. It is, however, possible to detect the two brightest features at both ends of the loops, though not the one where the filaments intersect.

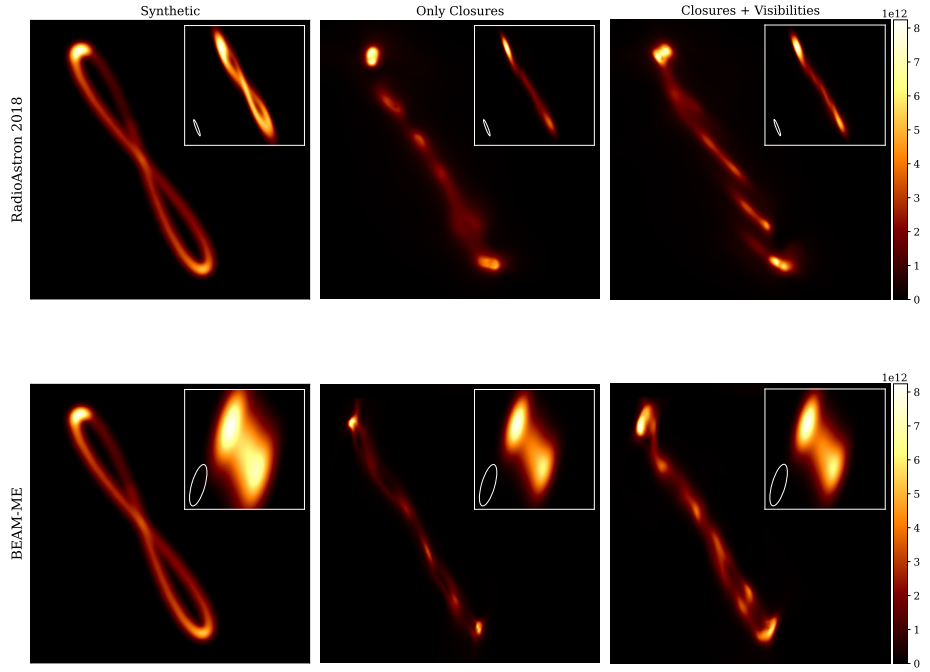

Figure 4.6: Synthetic data test using different data terms to probe filament detection using the RadioAstron uv-coverage of 2018 (first row) and BEAM-ME February 2018 (second row). Units of the colorbar indicate brightness temperature in Kelvin. Field of view is 1.3 × 1.3 mas. The nominal beam for each dataset is plotted in white at the bottom left of the synthetic images.

Thus, even if filaments were present in the source at the time of our observations, their existence could not be reliably confirmed.

For the second row, where the BEAM-ME synthetic test is displayed, we also tried to see if with the coverage of this monitoring program, it would be possible to recover the filamentary structure. Again, as can be observed in Fig. 4.6 (lower panel), it is not possible to recover any filaments, but an approximately straight line of emission, also showing an uneven brightness distribution. The reconstruction does not really improve when adding the visibilities, as happened in the previous case, but does manage to obtain the bright features at the loop edges.

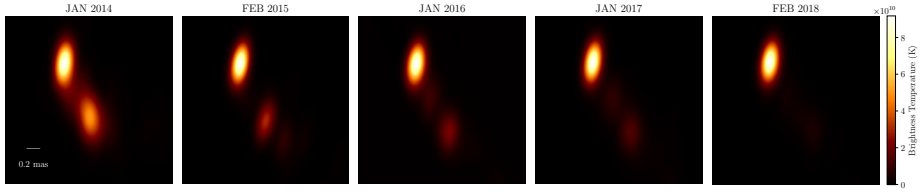

Figure 4.7: BEAM-ME yearly evolution from archival data between 2014 and 2018 of 3C 279 using a field of view of 2 × 2 mas.

A successful recovery of the filamentary structure can be seen in the test performed in Fuentes et al. (2023), supporting their existence.

4.2.3 BEAM-ME evolution

We can contextualize our results by looking at public data from BEAM-ME at 43 GHz, and thus study the brightness evolution of 3C 279 jet and its dynamic nature. In Fig. 4.7, we show epochs yearly, spanning approximately four years from 2014 to 2018, in order to discern any change in the source that may confirm and help understand the lack of filament detection.

While in the BEAM-ME webpage there is already access to these images made by Difmap using the traditional CLEAN method, we used the already calibrated fits files and displayed them (not reconstructed) in Stokes I using `eht-imaging` library, the same one used to reconstruct the 2018 *RadioAstron* data. By doing so, we capture a comprehensive view of the temporal evolution of the blazar over four years, seeing that this period in particular highlights a "turning off" phase.

We note that from 2014 to 2018, the source progressively decreased its brightness; this fact is also clear if we look at the light curve shown in Fig. 4.8. This decline in brightness is not uncommon in blazars known for the variability of their light curves, often on timescales of years to decades (e.g., Teräsranta et al. 1992; Lister et al. 2018; Mohana et al. 2023; Eppel, F. et al. 2024). Such variability can be influenced by changes in the Doppler beaming factor or accretion rate onto the black hole.

Notably, the decrease in brightness of the source poses significant implications for our ability to observe and resolve any structural details in the jet, both in total intensity and polarization. This means that as the source dims towards 2018, features in the jet become harder to detect and any structure is substituted by a mostly straight faint line of emission, impending the study of the intricate

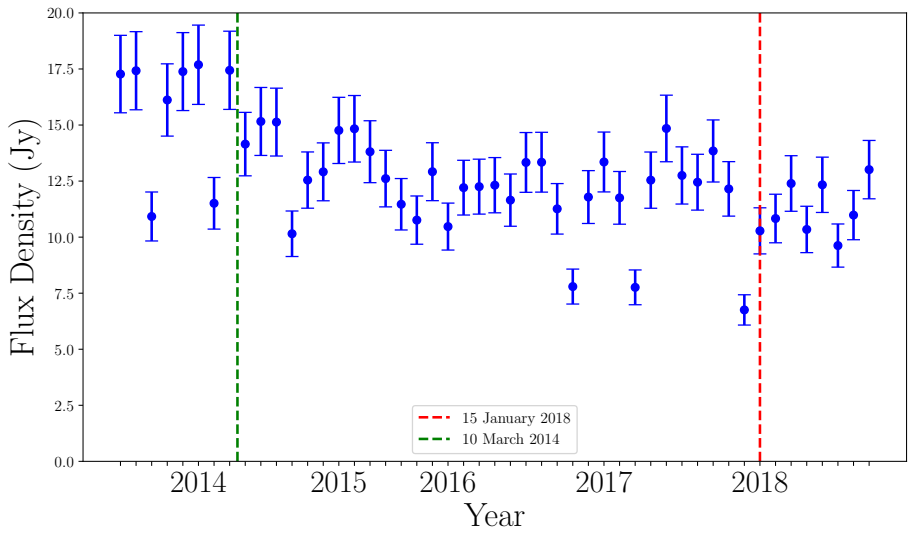

Figure 4.8: Lightcurve of 3C 279 at 43 GHz from BEAM-ME project constructed using the flux density of CLEAN images (within a field of view of 2×2 mas). We estimated uncertainties of 10% indicated with errorbars.

magnetic field configurations and plasma dynamics that drive the jet physics in 3C 279.

Moreover, we can directly compare BEAM-ME images from close-in-time epochs to the *RadioAstron* observations, i.e., from February 2014 and 2018 (see Fig. 4.10). It is possible to see a slight change in the orientation, with the 2018 epoch showing a small counterclockwise direction. This behaviour is also observed between the *RadioAstron* epochs (see Sec. 4.2.4).

4.2.4 Comparison with 2014 results

Let us now look at a direct comparison between the previous *RadioAstron* observation of 3C 279 at 22 GHz from 2014 observations (Fuentes et al. 2023) and our 2018 data. A summary of the main differences is shown in Table 4.2. Fig. 4.9 shows both images overlayed in a $\sim 1.7 \times 1.7$ mas field of view, where the 2014 epoch is plotted in contours and aligned using the brightest pixel of both images. This particular alignment is motivated by the incompatible fields of view from EHT (230 GHz) and RadioAstron image (22 GHz), which makes an alignment on optically thin components unfeasible. The coreshift between both frequencies has

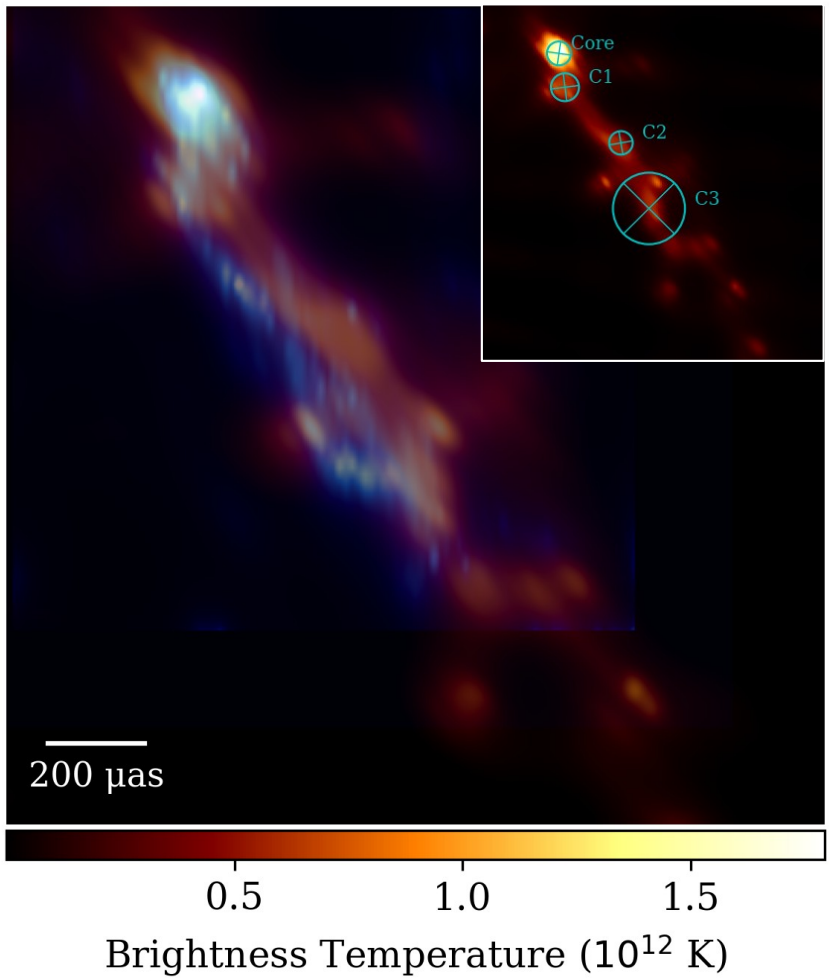

Figure 4.9: Main image: a direct comparison between the 2014 and 2018 images of 3C 279 at 22 GHz with *RadioAstron*. The 2018 epoch is plotted in warm color scale *afmhot* and aligned with the 2014 epoch (Fuentes et al. 2023), in blue, using the brightest pixel. Top right image shows overlapped the Gaussian components from the model fitting process. The fifth component (E) is not shown since it is a large component necessary to take into account the diffuse emission.

been disregarded, but can be estimated as $\sim 40\,\mu as$.

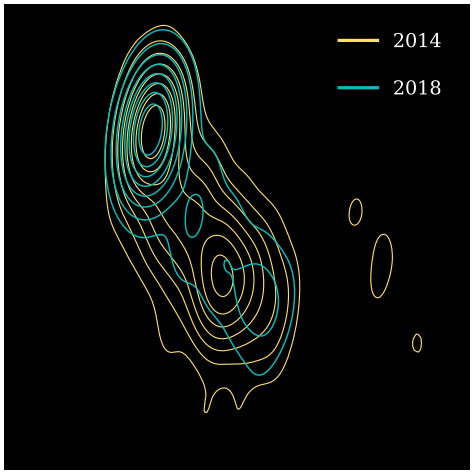

Figure 4.10: BEAM-ME image comparison between 2014 and 2018 epochs. Contours display 0.2 to 0.9 of the maximum brightness in intervals of 0.1.

The main difference observed in 2018 epoch is that the filamentary structure seen in Fuentes et al. (2023) (2014 epoch) does not appear to be present four years later, in 2018. The orientation of the jet direction has also changed between both epochs, being slightly rotated in a counterclockwise motion.

The total intensity of the source has greatly changed, as mentioned in the previous subsection, going from 27.16 Jy in 2014 to 10.2 Jy in 2018. In 2014 observations, bright emission regions could be observed due to Doppler boosting. However, these features do not appear so clearly in 2018 data.

The integrated degree of linear polarization of the source is found to be around 5% in 2018, unlike the 10% found in 2014, hinting at more ordered magnetic fields. Nevertheless, from the Fig. 4.4 it is possible to see that the EVPA direction (see Section 3.1.2) is in 2018 similar to 2014 observations, still mostly parallel the jet direction, supporting the existence of a strong toroidal component and in agreement with a helical magnetic field configuration. In some regions, however, such as next to the core or at the bend by the end of the jet we detect, this general direction seems to rotate and become almost perpendicular to it. Our findings concur with previous detections of toroidal magnetic fields using VLBI polarimetric studies (e.g., Cho et al. 2024), through polarization structures and transverse Faraday rotation measure gradients (Toscano, Teresa et al. 2025; Kovalev et al. 2025b).

Epoch	Flux (Jy)	Ground stations	Resolution (μas)	Filament detection	Fractional polarization
March 2014	27.2 ± 0.2	23	27	yes	$\sim$ 10± 0.2%
January 2018	10.2 ± 0.5	14	26	no	$\sim$ 5 ± 0.2 %

Table 4.2: Summary of the main differences between 2014 and 2018 observations of 3C 279 at 22 GHz with *RadioAstron*.

4.2.5 Brightness Temperature

The plasma acceleration and radiative evolution of the jet's innermost region can be studied through estimations of the brightness temperature (Readhead 1994; Marscher 1995; Kovalev et al. 2005; Fromm et al. 2013; Röder et al. 2025). It mainly provides an approximation of the source brightness, making it possible to characterize the energy partition between plasma and the magnetic field assuming self-absorbed synchrotron radiation (Readhead 1994; Homan et al. 2006; Kovalev et al. 2016; Homan et al. 2021).

The inverse Compton process limits the maximum intrinsic brightness temperature for incoherent synchrotron sources, corresponding to (0.3–1) $\times 10^{12}$K (Kellermann & Pauliny-Toth 1969). If a flare has taken place and the brightness temperature exceeds this limit, the source is expected to cool rapidly—on the order of a day—due to catastrophic inverse Compton losses. This estimate assumes a homogeneous, self-absorbed synchrotron source with no significant Doppler boosting, no ongoing particle acceleration, and efficient energy loss via inverse Compton scattering (e.g., Readhead 1994; Slysh 1992).

Complimentary to this, another upper threshold arises for sources near the equipartition, referred to as equipartition brightness temperature (T_{eq}, where the energy density of the magnetic field is approximately equal to the energy density of the relativistic particles), of value $\sim 5 \times 10^{10}$ K (Readhead 1994; Singal 2009).

On another hand, refractive scattering in the interstellar medium can introduce substructure that biases brightness temperature estimates at longer wavelengths (Johnson et al. 2016), but its impact decreases sharply with frequency. At 22 GHz this effect is negligible and therefore, not taken into account in the following analysis.

The brightness temperature parameter is commonly determined by modeling the structure of the emitting region, estimating the flux density and angular size of the model components. The observed brightness temperature in this work is

Component ID	S (Jy)	FWHM (mas)	r (mas)	PA (°)	$T_{\mathrm{b},obs}$ (K)
Core	6.40 ± 0.64	0.10 ± 0.01	0	0	(1.6± 0.2) $\times 10^{12}$
C1	1.04 ± 0.10	0.13 ± 0.01	0.13 ± 0.01	11.3 ± 1.2	(1.5± 0.2) $\times 10^{11}$
C2	0.29 ± 0.02	0.09 ± 0.01	0.57 ± 0.03	36.9 ± 3.3	(8.8± 0.9) $\times 10^{10}$
C3	1.58 ± 0.15	0.30 ± 0.01	0.86 ± 0.02	32.3 ± 3.3	(4.3± 0.4) $\times 10^{10}$
E	0.68 ± 0.07	1.64 ± 0.02	2.26 ± 0.01	36.6 ± 3.4	(6.2± 0.6) $\times 10^{8}$

Table 4.3: Model fitting results from the *RadioAstron* image. From left to right columns show: Component ID, flux density in Jy, size of the component in mas, radial distance from the core in mas, position angle of the component position with respect to the core in degrees (origin in North and positive counterclockwise direction) and observed brightness temperature (without Doppler and redshift correction) in Kelvin (K).

calculated by fitting circular Gaussian components with different flux densities and sizes (see Table 4.3 columns 1 to 5 and Fig. 4.9) using the `modelfit` function in Difmap (Pushkarev & Kovalev 2012; Gómez et al. 2022). The error for the flux density was estimated to be $\sim 10\%$, since it is mostly dominated by the a priori calibration. Errors for the rest of the quantities were also set to $\sim 10\%$ of their value since the statistical errors from the fitting itself are commonly misleadingly small and do not convey the systematic uncertainties from the measurements. The brightness temperature is given by (e.g., Gómez et al. 2022):

$$T_{\mathrm{b},obs} = 1.22 \times 10^{12} \left(\frac{S_\nu}{\mathrm{Jy}}\right) \left(\frac{\nu_{obs}}{\mathrm{GHz}}\right)^{-2} \left(\frac{\theta_{obs}}{\mathrm{mas}}\right)^{-2} [K]\,, \qquad (4.2)$$

where S_ν is the component flux density, θ_{obs} is the size of the model component, and ν_{obs} is the observing frequency.

Using Eq. 4.2, we estimated the brightness temperatures corresponding to the different components of the image model (see Table 4.3, column 6), finding five different components that amount to 10.0 Jy (out of the 10.2 Jy found in the image), which is a good approximation. In order to get a good fit, a large component E is required to capture some extended emission (as seen in Table 4.3), but it is not shown in Fig. 4.9.

Moreover, to calculate the intrinsic brightness temperature of the jet, we also need to take into account the cosmological correction and the Doppler boosting effect. The blazar 3C 279, with an estimated viewing angle of $\theta \sim 2°$ (Jorstad et al. 2017), is known to have a wide range of Doppler factor (δ) values [10-40] (Jorstad et al. 2005a; Bloom et al. 2013; Jorstad et al. 2017; Kim et al. 2020a).

The observed brightness temperature is related to the intrinsic one of the jet $T_{\mathrm{b},int}$ as follows:

$$T_{\mathrm{b},int} = T_{\mathrm{b},obs}\frac{1+z}{\delta}\,, \tag{4.3}$$

where z is the cosmological redshift of the source.

From the observed brightness temperature values found, assuming the most likely scenario that the radiative losses are from synchrotron radiation, we can see that the observed brightness temperature of the core has a value of 1.6×10^{12} K. Such high and even higher values are common in *RadioAstron* observations (e.g., Kovalev et al. 2016; Gómez et al. 2016; Bruni et al. 2017; Pilipenko et al. 2017; Kovalev et al. 2020; Röder et al. 2025).

However, the intrinsic brightness temperature value of the core, of $\sim 10^{11}$ K, calculated assuming a Doppler factor of 24 (Jorstad et al. 2005a; Kim et al. 2020a), can be reconciled with the Inverse Compton limit, considering the high Doppler factor observed in 3C 279. This value suggests that the core is close to equipartition, meaning that the energy densities of the relativistic particles and the magnetic field are nearly balanced. This is consistent with the lack of evident flaring events in radio frequencies around the time of our observations. The rest of the components show a decrease of brightness temperature as we move further away from the core, following the expected energy dissipation with distance via adiabatic and radiative losses.

Given that the 22GHz RadioAstron image shows a substructure in the core that is not possible to see at 43 GHz, we can assume that the core seen at 43 GHz includes both the Core and the C1 component from Table 3. In this case, the spectral index can be roughly estimated yielding a value of 0.28. This result is consistent with optically thick synchrotron emission from a stratified AGN jet core, which typically falls between (0.2-0.6).

The observed brightness temperature at the core (including cosmological and Doppler boosting corrections), where the frequency is also affected by Doppler factor so that $\nu_{int} = \nu_{obs}(1+z)/\delta$, can be related to the magnetic field strength of a synchrotron self-absorbed core (Section 5.3 of Condon & Ransom 2016). We can justify the core to be optically thick by establishing a rough spectral index (α) comparing the brightness of the 22 GHz *RadioAstron* core (6.40 Jy) to that of the BEAM-ME 43 GHz core (8.85 Jy, calculated also using modelfit), yielding a value of ~ 0.48. This result is consistent with optically thick synchrotron emission from a stratified AGN jet core, which typically falls between (0.2-0.6). Therefore, we can apply the magnetic field the relation:

$$B = 1.4 \times 10^{21} \left(\frac{\nu_{\rm obs}}{\rm GHz}\right) \left(\frac{T_{\rm b,}obs}{\rm K}\right)^{-2} \frac{\delta}{(1+z)} \, [\rm G] \, , \tag{4.4}$$

yielding a magnetic field strength of $\sim$ 0.2 G near the core. This value is consistent with those found in Röder et al. (2025), based on Y. Y. Kovalev et al. in prep.

4.3 Conclusion

In this chapter we have analysed the *RadioAstron* observations of 3C 279 on 2018 January 15 at 22 GHz, the last possible of this source with this space VLBI mission. The array sensitivity, together with RML methods (`eht-imaging`), have enabled us to obtain super-resolved images of the 3C 279 jet with high angular resolution (26 μas). The images reveal the lack of detection of a filament-like structure found in a similar previous study with *RadioAstron*, using data from a 2014 epoch (Fuentes et al. 2023).

Further analysis using synthetic data with both our array properties and those of BEAM-ME close-in-time, supports the fact that the lack of filament detection is not necessarily related to their non-existence, but most likely due to an insufficient uv coverage. Moreover, observations from BEAM-ME public data reveal that over the 4-year-period 2014-2018, the source exhibits a gradual decline in brightness, affecting our ability to resolve its jet structure in both total intensity and polarization. We also explore the gamma-ray emission relation with our observations, finding that they coincide with the rising of a gamma-ray flare surpassing the last one in brightness from 2015. Nevertheless, we find that this phenomenon does not seem to impact or correlate with our results.

Finally, a study of the brightness temperature using model fitting with Gaussian components yields a core with an observed brightness temperature of the order of 10^{12} K, in agreement with previous *RadioAstron* observations, and an estimated magnetic field strength of $\sim$ 0.2 G in the core region. The values found for the jet's brightness temperature suggest it to be close to equipartition, as can be expected for a source in a low activity period.

Chapter 5

Conclusions

The conclusions of this thesis can be summarized as follows. The first study of this thesis tackles the challenge of getting the first movies of black holes. As a consequence, we presented the `MO-PSO` algorithm validation on Sgr A*synthetic dynamic models. We showed that while standard RML techniques remain central to forward-imaging strategies in VLBI, they face significant limitations, particularly in dynamic imaging of variable sources like Sgr A*. By extending the RML framework using `MOEA/D` and `MO-PSO` , we achieve more efficient hyperparameter exploration and enhanced flexibility, enabling applications such as dynamic reconstructions and scattering mitigation. `MO-PSO` shows promising results in some of the models evaluated: it avoids hallucinated motion, accurately recovers polarization and position angles, and improves static reconstructions with respect to previous studies. However, challenges remain, including recovering polarization values, brightness inaccuracies, phantom features, and noise in dynamic components, preventing it from passing the strict validation. Despite these limitations, `MO-PSO` uniquely explores the multimodal solution space, revealing diverse reconstruction clusters and emphasizing that a good reconstruction fitting the data does not necessarily imply a plausible physical model. These findings highlight the potential and adaptability of `MO-PSO` for static imaging, opening the door to future improvements regarding the recovery of complex source dynamics.

Next, we move away from the black hole itself to the magnetic fields involved in jet formation. For that purpose, we present a study using multi-frequency polarimetric observations of 3C 273 revealing a persistent transverse RM gradient across the jet, with both negative and positive RM values, confirming the continued presence of this feature over time. Comparison with past studies shows overall consistency, supporting a stable external Faraday screen—likely a magnetised

sheath surrounding the jet—as the dominant source of Faraday rotation. Together, the observed EVPA orientations, RM distribution, and transverse polarisation gradients all point to the presence of a helical magnetic field configuration with a strong toroidal component, which likely contributes to the jet collimation and stability. Variations in RM structure, such as the increase in positive RM values and their spatial location, may reflect evolving asymmetries in the surrounding plasma. These findings are in agreement with previous interpretations and reinforce the crucial role of large-scale, ordered magnetic fields in the dynamics of AGN jets, although new future high-resolution, multi-frequency polarimetric studies will be essential to better understand the relations between internal and external Faraday rotation and the jet's magnetic field evolution.

Lastly, we conclude our journey by studying the jet structure and evolution using high resolution images from *RadioAstron* observations of 3C 279 on 2018 January 15 at 22 GHz. We see that the array sensitivity using space-VLBI, together with RML methods (`eht-imaging`), have enabled us to obtain super-resolved images of the 3C 279 jet with high angular resolution (26 μas). The images reveal the lack of detection of a filament-like structure found in a similar previous study with RadioAstron, using data from a 2014 epoch (Fuentes et al. 2023). Further analysis using synthetic data with both our array properties and those of BEAM-ME close-in-time, supports the fact that the lack of filament detection is not necessarily related to their non-existence, but most likely due to an insufficient uv coverage. Moreover, observations from BEAM-ME archival data reveal that over the 4-year-period 2014-2018, the source gradually decreases its brightness, also affecting our ability to resolve the jet structure in both total intensity and polarization. The study of the jet's brightness temperature using model fitting with Gaussian components yields a core with an observed brightness temperature of the order of 10^{12} K, in agreement with previous *RadioAstron* observations, and an estimated magnetic field strength of ~ 0.2 G in the core region. The values found for the jet's intrinsic brightness temperatures suggest it to be close to equipartition, as can be expected for a source in a low activity period.

Thus, the results of this thesis evidence a collective effort into the power and limitations of current VLBI imaging techniques. By combining advanced imaging algorithms, polarimetric analysis, and space-VLBI observations, we take one more step forward the understanding of the complex structure and magnetic dynamics of relativistic jets and supermassive black holes.

In the future, building on the background provided by these studies, I would like to keep exploring AGN jets and their formation and physical processes using more advanced imaging methods based on neural networks. Moreover, I will become involved in new multimessenger studies, searching the origin of high-

energy neutrino emission, aiming to understand how energy is extracted from galactic nuclei and the mechanism responsible for the production of cosmic rays.

Chapter 6

Conclusiones

Las conclusiones de esta tesis se pueden resumir de la siguiente manera. El primer estudio de esta tesis trata de conseguir las primeras películas de agujeros negros. En consecuencia, se presenta la validación del algoritmo `MO-PSO` sobre modelos dinámicos sintéticos de Sgr A*, mostrando que si bien las técnicas RML estándar siguen siendo fundamentales en las estrategias de imagen directa en VLBI, estas presentan limitaciones importantes, especialmente para el análisis de fuentes variables como Sgr A*. Al ampliar la estructura RML mediante `MOEA/D` y `MO-PSO` , se logra una exploración más eficiente del espacio de hiperparámetros y una mayor flexibilidad, lo que permite realizar reconstrucciones dinámicas y tener en cuenta la mitigación de la dispersión. `MO-PSO` ofrece resultados prometedores en algunos de modelos evaluados: evita crear movimientos artificiales, recupera con precisión la polarización y los ángulos de posición, y mejora las reconstrucciones estáticas con respecto a estudios anteriores. Sin embargo, desafíos respecto a la recuperación de valores de polarización, imprecisiones en el brillo, estructuras duplicadas y ruido en los componentes dinámicos continúan apareciendo, lo que impide que supere los altos criterios de validación impuestos. A pesar de estas limitaciones, `MO-PSO` permite explorar de forma única el espacio multimodal de soluciones, revelando clústeres diversos de reconstrucción y mencionando en especial que una buena reconstrucción de los datos no implica necesariamente un modelo físico plausible. Estos resultados destacan el potencial y la adaptabilidad de `MO-PSO` para imágenes estáticas, abriendo el camino a futuras mejoras en la recuperación de rasgos dinámicos complejos de fuentes variables.

Por otro lado, nos movemos fuera del agujero negro para estudiar los campos magnéticos involucrados en la formación de jets. Para ello, usamos un estudio basado en observaciones polarimétricas y multifrecuencia de 3C 273, el cual revela

un gradiente transversal persistente en la medida de rotación a lo largo del chorro, con valores tanto negativos como positivos, confirmando que esta característica se mantiene en el tiempo. La comparación con estudios previos muestra una consistencia general de los resultados, apoyando la posible existencia de una pantalla de Faraday externa y estable—probablemente en forma de una envoltura magnetizada que rodea al chorro—como origen dominante de la rotación de Faraday. En su conjunto, las orientaciones observadas del EVPA, la distribución de RM y los gradientes de polarización transversales apuntan a la presencia de un campo magnético helicoidal con una fuerte componente toroidal, que probablemente contribuye a la colimación y estabilidad del chorro. Las variaciones observadas en la estructura de RM, como el aumento de valores positivos y su localización, podrían reflejar asimetrías propias de la evolución del plasma circundante. Estos resultados coinciden con interpretaciones anteriores y refuerzan el papel fundamental de los campos magnéticos ordenados a gran escala en la dinámica de los chorros de AGNs, aunque serán necesarios más estudios polarimétricos multifrecuencia de alta resolución para comprender mejor la relación entre la rotación de Faraday interna y externa y la evolución del campo magnético del chorro.

Finalmente, concluimos nuestro viaje estudiando la propia estructura y evolución del jet usando observaciones de *RadioAstron* de 3C 279 realizadas el 15 de enero de 2018 a 22 GHz. Estos resultados muestran que la sensibilidad de la red VLBI junto con el radio telescopio espacial, junto con el uso de métodos RML (`eht-imaging`), permite obtener imágenes de alta resolución del chorro de 3C 279, con una resolución angular de 26 μas. Sin embargo, las imágenes no muestran la estructura conformada de filamentos detectada en un estudio previo de 2014 también con *RadioAstron* (Fuentes et al. 2023). El análisis realizado con datos sintéticos, usando tanto las propiedades de nuestros datos como las de BEAM-ME en fechas cercanas, indica que la falta de detección de filamentos no se debe necesariamente a su ausencia física, sino probablemente al hecho de tener en nuestros datos un cubrimiento *uv* insuficiente. Además, datos provenientes de BEAM-ME muestran que entre 2014 y 2018 la fuente disminuyó gradualmente su brillo, afectando también a nuestra capacidad para resolver la estructura del chorro tanto en intensidad total como en polarización. El estudio de la temperatura de brillo del chorro mediante ajuste de modelos con componentes gaussianas muestra un núcleo con una temperatura de brillo del orden de 10^{12} K, en concordancia con observaciones previas de *RadioAstron*, y una estimación del campo magnético de ~ 0.2 G en la región del núcleo. Los valores encontrados para las temperaturas de brillo intrínsecas del chorro sugieren que se encuentra cerca del equilibrio entre energía de partículas y campo magnético (equipartición), como cabría esperar para una fuente durante un periodo de baja actividad.

Así, los resultados de esta tesis reflejan un esfuerzo conjunto e interdisciplinar explorando el potencial y las limitaciones de las técnicas actuales de reconstrucción de imagen en VLBI. Al combinar algoritmos avanzados de reconstrucción de imagen, análisis polarimétrico y observaciones con la misión espacial VLBI *RadioAstron*, damos un paso más en la comprensión de las complejas estructuras y dinámicas que gobiernan los chorros relativistas y los agujeros negros supermasivos.

En el futuro, basándome en la experiencia adquirida a través de los estudios presentados, me gustaría seguir explorando los chorros de los AGN, en particular su formación y evolución, utilizando métodos de imagen más avanzados basados en redes neuronales. Además, tengo intención de involucrarme en nuevos estudios multimensajeros, investigando el origen de la emisión de neutrinos de alta energía, con el objetivo de comprender cómo se extrae la energía de los núcleos galácticos y cuál es el mecanismo responsable de la producción de rayos cósmicos.

Bibliography

Agudo, I., Jorstad, S. G., Marscher, A. P., Larionov, V. M., & Gómez, J. L. 2011, 2011 Fermi Simposium, 1

Akiyama, K., Ikeda, S., Pleau, M., et al. 2017a, AJ, 153, 159

Akiyama, K., Ikeda, S., Pleau, M., et al. 2017b, AJ, 153, 159

Akiyama, K., Kuramochi, K., Ikeda, S., et al. 2017c, ApJ, 838, 1

Albentosa-Ruiz, E. & Marti-Vidal, I. 2023, A&A, 672, A67

Angel, J. R. P. & Stockman, H. S. 1980, ARA&A, 18, 321

Angelakis, E., Fuhrmann, L., Myserlis, I., et al. 2019, A&A, 626, A60

Antonucci, R. 1993, Annual Review of Astronomy and Astrophysics, 31, 473

Arras, P., Bester, H. L., Perley, R. A., et al. 2021, A&A, 646, A84

Asada, K., Inoue, M., Kameno, S., & Nagai, H. 2005, in Astronomical Society of the Pacific Conference Series, Vol. 340, Future Directions in High Resolution Astronomy, ed. J. Romney & M. Reid, 168

Asada, K., Inoue, M., Kameno, S., & Nagai, H. 2008, ApJ, 675, 79

Asada, K., Inoue, M., Uchida, Y., et al. 2002, PASJ, 54, L39

Asada, K. & Nakamura, M. 2012, ApJ, 745, L28

Attridge, J. M., Wardle, J. F. C., Homan, D. C., & Phillips, R. B. 2005, in Astronomical Society of the Pacific Conference Series, Vol. 340, Future Directions in High Resolution Astronomy, ed. J. Romney & M. Reid, 171

Baade, W. & Minkowski, R. 1954, ApJ, 119, 206

Baaquie, B. E. & Willeboordse, F. H. 2015, Exploring the invisible universe: from black holes to superstrings (Hackensack, New Jersey: World Scientific)

Balbus, S. A. & Hawley, J. F. 1991, ApJ, 376, 214

Begelman, M. C., Blandford, R. D., & Rees, M. J. 1984, Rev. Mod. Phys., 56, 255

Blackburn, L., Chan, C.-k., Crew, G. B., et al. 2019, ApJ, 882, 23

Blackburn, L., Pesce, D. W., Johnson, M. D., et al. 2020, ApJ, 894, 31

Blake, G. M. 1972, Monthly Notices of the Royal Astronomical Society, 156, 67

Blandford, R., Meier, D., & Readhead, A. 2019, ARA&A, 57, 467

Blandford, R. D. 1988, in Perspectives in Fluid Mechanics, ed. D. Coles, Vol. 320 (Springer Nature), 14–30

Blandford, R. D. 1993, in Astrophysical Jets, ed. D. Burgarella, M. Livio, & C. P. O'Dea (Cambridge University Press), 15–33

Blandford, R. D. & Konigl, A. 1979, ApJ, 232, 34

Blandford, R. D. & Königl, A. 1979, ApJ, 232, 34

Blandford, R. D. & Payne, D. G. 1982, Monthly Notices of the Royal Astronomical Society, 199, 883, _eprint: https://academic.oup.com/mnras/article-pdf/199/4/883/2880142/mnras199-0883.pdf

Blandford, R. D. & Payne, D. G. 1982, MNRAS, 199, 883

Blandford, R. D. & Znajek, R. L. 1977, Monthly Notices of the Royal Astronomical Society, 179, 433, _eprint: https://academic.oup.com/mnras/article-pdf/179/3/433/9333653/mnras179-0433.pdf

Blandford, R. D. & Znajek, R. L. 1977a, MNRAS, 179, 433

Blandford, R. D. & Znajek, R. L. 1977b, MNRAS, 179, 433

Bloom, S. D., Fromm, C. M., & Ros, E. 2013, AJ, 145, 12

Bloom, S. D., Fromm, C. M., & Ros, E. 2013, AJ, 145, 12

Boccardi, B., Krichbaum, T. P., Ros, E., & Zensus, J. A. 2017, A&A Rev., 25, 4

Bolton, J. G., Stanley, G. J., & Slee, O. B. 1949, Nature, 164, 101

Bonnans, J.-F., Gilbert, J. C., Lemaréchal, C., & Sagastizábal, C. A. 2006, Numerical Optimization: Theoretical and Practical Aspects, 2nd edn. (Berlin, Heidelberg: Springer Science & Business Media), 494

Bouman, K. L., Johnson, M. D., Dalca, A. V., et al. 2017, arXiv e-prints, arXiv:1711.01357

Bower, G. C., Falcke, H., Herrnstein, R. M., et al. 2004, Science, 304, 704

Bower, G. C., Markoff, S., Dexter, J., et al. 2015, ApJ, 802, 69

Briggs, D. S. 1995, PhD thesis, New Mexico Institute of Mining and Technology

Broderick, A. E., Pesce, D. W., Tiede, P., Pu, H.-Y., & Gold, R. 2020, ApJ, 898, 9

Bruni, G., Anderson, J. M., Alef, W., et al. 2016, Galaxies, 4, 55

Bruni, G., Gómez, J. L., Casadio, C., et al. 2017, A&A, 604, A111

Bruni, G., Gómez, J. L., Vega-García, L., et al. 2021, A&A, 654, A27

Burke, B. F. & Graham-Smith, F. 2010, An introduction to radio astronomy, 3rd edn. (Cambridge ; New York: Cambridge University Press)

Burn, B. J. 1966, MNRAS, 133, 67

Camenzind, M. 1986, A&A, 156, 137

Casadio, C., Krichbaum, T. P., Marscher, A. P., et al. 2017, Galaxies, 5, 67

Celotti, A., Miller, J. C., & Sciama, D. W. 1999, Classical and Quantum Gravity, 16, A3

Chael, A., Rowan, M., Narayan, R., Johnson, M., & Sironi, L. 2018a, MNRAS, 478, 5209

Chael, A. A., Johnson, M. D., Bouman, K. L., et al. 2018b, ApJ, 857, 23

Chael, A. A., Johnson, M. D., Narayan, R., et al. 2016a, ApJ, 829, 11

Chael, A. A., Johnson, M. D., Narayan, R., et al. 2016b, ApJ, 829, 11

Chen, T. 2005, PhD thesis, Brandeis University, Massachusetts

Cho, Gómez, José L., Lico, Rocco, et al. 2024, A&A, 683, A248

Cohen, M. H., Cannon, W., Purcell, G. H., et al. 1971, ApJ, 170, 207

Condon, J. J. & Ransom, S. M. 2016, Essential Radio Astronomy (Princeton University Press)

Contopoulos, I., Gabuzda, D., & Kylafis, N. 2015, The Formation and Disruption of Black Hole Jets (Springer International Publishing)

Conway, R. G., Garrington, S. T., Perley, R. A., & Biretta, J. A. 1993, A&A, 267, 347

Cornwell, T. J. & Evans, K. F. 1985, A&A, 143, 77

Croke, S. M. & Gabuzda, D. C. 2008, MNRAS, 386, 619

Curtis, H. D. 1918, Publications of Lick Observatory, 13, 9

Dahale, R. 2025, in preparation

Davis, R. J., Muxlow, T. W. B., & Conway, R. G. 1985, Nature, 318, 343

de Pater, I. & Perley, R. A. 1983, ApJ, 273, 64

Do, T., Hees, A., Ghez, A., et al. 2019, Science, 365, 664

Doeleman, S., Blackburn, L., Dexter, J., et al. 2019, in Bulletin of the American Astronomical Society, Vol. 51, 256

Doeleman, S. S., Weintroub, J., Rogers, A. E. E., et al. 2008, Nature, 455, 78

Eppel, F., Kadler, M., Heßdörfer, J., et al. 2024, A&A, 684, A11

Event Horizon Telescope Collaboration et al. 2019a, ApJ, 875, L1

Event Horizon Telescope Collaboration et al. 2019b, ApJ, 875, L2

Event Horizon Telescope Collaboration et al. 2019c, ApJ, 875, L3

Event Horizon Telescope Collaboration et al. 2019d, ApJ, 875, L4

Event Horizon Telescope Collaboration et al. 2019e, ApJ, 875, L5

Event Horizon Telescope Collaboration et al. 2019f, ApJ, 875, L6

Event Horizon Telescope Collaboration et al. 2021, ApJL, 910, 48

Event Horizon Telescope Collaboration et al. 2022a, ApJ, 930, L12

Event Horizon Telescope Collaboration et al. 2022b, ApJ, 930, L13

Event Horizon Telescope Collaboration et al. 2022c, ApJ, 930, L14

Event Horizon Telescope Collaboration et al. 2022d, ApJ, 930, L15

Event Horizon Telescope Collaboration et al. 2022e, ApJ, 930, L16

Event Horizon Telescope Collaboration et al. 2022f, ApJ, 930, L17

Event Horizon Telescope Collaboration et al. 2023, ApJ, 957, L20

Event Horizon Telescope Collaboration et al. 2024a, ApJLetters, 964, L25

Event Horizon Telescope Collaboration et al. 2024b, ApJ, 964, L25

Event Horizon Telescope Collaboration et al. 2024c, The Astrophysical Journal Letters, 964, L25

Event Horizon Telescope Collaboration et al. 2024d, ApJ, 964, L26

Event Horizon Telescope Collaboration et al. 2024e, A&A, 681, A79

Event Horizon Telescope Collaboration et al. 2025, in preparation

Falcke, H., Goss, W. M., Matsuo, H., et al. 1998, ApJ, 499, 731

Fanaroff, B. L. & Riley, J. M. 1974, MNRAS, 167, 31P

Farah, J., Galison, P., Akiyama, K., et al. 2022, ApJLetters, 930, 1

Fernández, A. F. 2023, Phd thesis, Universidad de Granada

Ferrari, A. 1998, Annual Review of Astronomy and Astrophysics, 36, 539

Ferreira, J. 1997, A&A, 319, 340

Foschi, M. 2025, in preparation

Foschi, M., Gómez, J. L., Fuentes, A., et al. 2025, A&A, 696, A17

Fromm, C. M., Ros, E., Perucho, M., et al. 2013, A&A, 557, A105

Fuentes, Torregrosa, I., Martí, J. M., Gómez, J. L., & Perucho, M. 2021, A&A, 650, A61

Fuentes, A., Foschi, M., Dahale, R., et al. 2025, In preparation

Fuentes, A., Gómez, J. L., Martí, J. M., & Perucho, M. 2018, ApJ, 860, 121

Fuentes, A., Gómez, J. L., Martí, J. M., et al. 2023, Nature Astronomy, 7, 1359

Gabuzda, D. C. 2021, Galaxies, 9, 58

Gabuzda, D. C., Roche, N., Kirwan, A., et al. 2017, MNRAS, 472, 1792

Gardner, F. F. & Whiteoak, J. B. 1966, Annu. Rev. Astro. Astrophys., 4, 245

Genzel, R., Eisenhauer, F., & Gillessen, S. 2010, Rev. Mod. Phys., 82, 3121

Ghez, A. M., Duchêne, G., Matthews, K., et al. 2003, ApJ, 586, L127

Ghez, A. M., Salim, S., Weinberg, N. N., et al. 2008, ApJ, 689, 1044

Ghisellini, G. 2013, Lecture Notes in Physics, Vol. 873, Radiative Processes in High Energy Astrophysics (Springer)

Gillessen, S., Eisenhauer, F., Trippe, S., et al. 2009, ApJ, 692, 1075

Giovannini, G., Savolainen, T., Orienti, M., et al. 2018, Nature Astronomy, 2, 472

Goddi, C., Crew, G., Impellizzeri, V., et al. 2019, The Messenger, 177, 25

Gomez, J. L., Alberdi, A., & Marcaide, J. M. 1993, A&A, 274, 55

Gómez, J. L., Casadio, C., Roca-Sogorb, M., et al. 2012, in International Journal of Modern Physics Conference Series, Vol. 8, International Journal of Modern Physics Conference Series, 265–270

Gómez, J. L., Lobanov, A. P., Bruni, G., et al. 2016, ApJ, 817, 96

Gómez, J. L., Marscher, A. P., Alberdi, A., Jorstad, S. G., & Agudo, I. 2001, ApJ, 561, L161

Gómez, J.-L., Marscher, A. P., Alberdi, A., Jorstad, S. G., & García-Miró, C. 2000, Science, 289, 2317

Gómez, J. L., Marscher, A. P., Jorstad, S. G., Agudo, I., & Roca-Sogorb, M. 2008, ApJ, 681, L69

Gomez, J. L., Marti, J. M. A., Marscher, A. P., Ibanez, J. M. A., & Marcaide, J. M. 1995, ApJ, 449, L19

Goyal, A., Soida, M., Stawarz, Ł., et al. 2022, ApJ, 927, 214

GRAVITY Collaboration, Abuter, R., Amorim, A., et al. 2018, A&A, 615, L15

GRAVITY Collaboration, Abuter, R., Amorim, A., et al. 2019, A&A, 625, L10

Greisen, E. W. 2003, in Astrophysics and Space Science Library, Vol. 285, Information Handling in Astronomy - Historical Vistas, ed. A. Heck, 109

Gubbay, J., Legg, A. J., Robertson, D. S., et al. 1969, Nature, 224, 1094

Gurvits, L. I., Paragi, Z., Amils, R. I., et al. 2022, Acta Astronautica, 196, 314

Gómez, J. L., Lobanov, A. P., Bruni, G., et al. 2016, ApJ, 817, 96

Gómez, J. L., Martí, J. M., Marscher, A. P., Ibáñez, J. M., & Alberdi, A. 1997, ApJ, 482, L33

Gómez, J. L., Roca-Sogorb, M., Agudo, I., Marscher, A. P., & Jorstad, S. G. 2011, ApJ, 733, 11

Gómez, J. L., Traianou, E., Krichbaum, T. P., et al. 2022, The Astrophysical Journal, 924, 122

Hada, K. 2019, Galaxies, 8, 1

Hada, K., Kino, M., Doi, A., et al. 2016, ApJ, 817, 131

Hardee, P. 2008, Journal of Physics: Conference Series, 131, 012052

Hardee, P. E. 2000, ApJ, 533, 176

Hardee, P. E. 2007, The Astrophysical Journal, 664, 26

Hartman, R. C., Bertsch, D. L., Fichtel, C. E., et al. 1992, ApJ, 385, L1

Heckman, T. M. 1980, A&A, 87, 152

Hirabayashi, H., Hirosawa, H., Kobayashi, H., et al. 1998, Science, 281, 1825

Högbom, J. A. 1974, A&AS, 15, 417

Holdaway, M. A. & Wardle, J. F. C. 1988, in Bulletin of the American Astronomical Society, Vol. 20, 1065

Homan, D. C., Cohen, M. H., Hovatta, T., et al. 2021, The Astrophysical Journal, 923, 67

Homan, D. C., Kovalev, Y. Y., Lister, M. L., et al. 2006, The Astrophysical Journal, 642, L115

Homan, D. C., Lister, M. L., Kellermann, K. I., et al. 2003, ApJ, 589, L9

Hovatta, T. & Lindfors, E. 2019, New A Rev., 87, 101541

Hovatta, T., Lister, M. L., Aller, M. F., et al. 2012, AJ, 144, 105

Issaoun, S., Wielgus, M., Jorstad, S., et al. 2022, ApJ, 934, 145

Jennison, R. C. 1958, Monthly Notices of the Royal Astronomical Society, 118, 276

Jester, S., Röser, H. J., Meisenheimer, K., & Perley, R. 2005, A&A, 431, 477

Johnson, M. D., Akiyama, K., Baturin, R., et al. 2024, in Space Telescopes and Instrumentation 2024: Optical, Infrared, and Millimeter Wave, ed. L. E. Coyle, S. Matsuura, & M. D. Perrin, Vol. 13092, International Society for Optics and Photonics (SPIE), 130922D

Johnson, M. D., Bouman, K. L., Blackburn, L., et al. 2017, ApJ, 850, 172

Johnson, M. D., Kovalev, Y. Y., Gwinn, C. R., et al. 2016, ApJ, 820, L10

Johnson, M. D., Lupsasca, A., Strominger, A., et al. 2020, Science Advances, 6, eaaz1310

Jorstad, S., Wielgus, M., Lico, R., et al. 2023, ApJ, 943, 170

Jorstad, S., Wielgus, M., Lico, R., et al. 2023, ApJ, 943, 170

Jorstad, S. G., Marscher, A. P., Lister, M. L., et al. 2005a, The Astronomical Journal, 130, 1418

Jorstad, S. G., Marscher, A. P., Lister, M. L., et al. 2005b, The Astronomical Journal, 130, 1418

Jorstad, S. G., Marscher, A. P., Morozova, D. A., et al. 2017, ApJ, 846, 98

Junklewitz, H., Bell, M. R., Selig, M., & Enßlin, T. A. 2016, A&A, 586, A76

Junklewitz, H., Bell, M. R., Selig, M., & Enßlin, T. A. 2016, A&A, 586, A76

Kardashev, N. S., Khartov, V. V., Abramov, V. V., et al. 2013, Astronomy Reports, 57, 153–194

Kellermann, K. I. & Pauliny-Toth, I. I. K. 1969, ApJ, 155, L71

Kellermann, K. I., Sramek, R., Schmidt, M., Shaffer, D. B., & Green, R. 1989, AJ, 98, 1195

Kettenis, M., van Langevelde, H. J., Reynolds, C., & Cotton, B. 2006, in Astronomical Society of the Pacific Conference Series, Vol. 351, Astronomical Data Analysis Software and Systems XV, ed. C. Gabriel, C. Arviset, D. Ponz, & S. Enrique, 497

Kim, Krichbaum, Thomas P., Broderick, Avery E., et al. 2020a, A&A, 640, A69

Kim, J.-Y., Krichbaum, T. P., Broderick, A. E., et al. 2020b, A&A, 640, A69

Knight, C. A., Robertson, D. S., Rogers, A. E. E., et al. 1971, Science, 172, 52

Knollmüller, J. 2025, in preparation

Koide, S., Shibata, K., & Kudoh, T. 1999, ApJ, 522, 727

Komatsu, E., Dunkley, J., Nolta, M. R., et al. 2009, The Astrophysical Journal Supplement Series, 180, 330

Komissarov, S. S. & Barkov, M. V. 2007, MNRAS, 382, 1029

Kovalev, Y. Y., Kardashev, N. S., Kellermann, K. I., et al. 2016, ApJ, 820, L9

Kovalev, Y. Y., Kardashev, N. S., Sokolovsky, K. V., et al. 2020, Advances in Space Research, 65, 705

Kovalev, Y. Y., Kellermann, K. I., Lister, M. L., et al. 2005, The Astronomical Journal, 130, 2473

Kovalev, Y. Y., Pushkarev, A. B., Gomez, J. L., et al. 2025a, arXiv e-prints, arXiv:2504.09287

Kovalev, Y. Y., Pushkarev, A. B., Gomez, J. L., et al. 2025b, arXiv e-prints, arXiv:2504.09287

Kraus, J. D. & Tiuri, M. E. 1966, Radio astronomy (New York; St Louis; San Francisco: McGraw-Hill), oCLC: 489741649

Kravchenko, E. V., Kovalev, Y. Y., & Sokolovsky, K. V. 2017, MNRAS, 467, 83

Krichbaum, T. P., Graham, D. A., Witzel, A., et al. 1998, A&A, 335, L106

Krichbaum, T. P., Witzel, A., Booth, R. S., et al. 1990, A&A, 237, 3

Krolik, J. H. 1999, Active galactic nuclei: from the central black hole to the galactic environment, Princeton series in astrophysics (Princeton, N.J: Princeton University Press)

Laplace, P. S. 1796, Exposition du système du monde (Duprat)

Li, H. & Zhang, Q. 2009, IEEE Transactions on Evolutionary Computation, 13, 284

Lisakov, M. M., Kravchenko, E. V., Pushkarev, A. B., et al. 2021, ApJ, 910, 35

Lister, M. L., Aller, H. D., Aller, M. F., et al. 2009, AJ, 137, 3718

Lister, M. L., Aller, M. F., Aller, H. D., et al. 2018, The Astrophysical Journal Supplement Series, 234, 12

Lister, M. L., Aller, M. F., Aller, H. D., et al. 2016, The Astronomical Journal, 151, 133

Lister, M. L., Homan, D. C., Hovatta, T., et al. 2019, ApJ, 874, 43

Lister, M. L., Homan, D. C., Kellermann, K. I., et al. 2021, ApJ, 923, 30

Lobanov. 2015, A&A, 574, A84

Lobanov, A. P., Gómez, J. L., Bruni, G., et al. 2015, A&A, 583, A100

Lobanov, A. P. & Zensus, J. A. 2001, Science, 294, 128

Lott, B., Escande, L., Larsson, S., & Ballet, J. 2012, A&A, 544, A6

Lu, R.-S., Asada, K., Krichbaum, T. P., et al. 2023, Nature, 616, 686

Lu, R.-S., Krichbaum, T. P., Roy, A. L., et al. 2018, ApJ, 859, 60

Lynden-Bell, D. 1969, Nature, 223, 690

Lyubarsky, Y. 2009, ApJ, 698, 1570

MAGIC Collaboration, Albert, J., Aliu, E., et al. 2008, Science, 320, 1752

Marscher, A. P. 1995, Proceedings of the National Academy of Sciences, 92, 11439

Marscher, A. P. & Gear, W. K. 1985, ApJ, 298, 114

Marscher, A. P., Jorstad, S. G., D'Arcangelo, F. D., et al. 2008, Nature, 452, 966

Marscher, A. P., Jorstad, S. G., Gómez, J.-L., et al. 2002, Nature, 417, 625

Marziani, P., Sulentic, J. W., Dultzin-Hacyan, D., Calvani, M., & Moles, M. 1996, ApJS, 104, 37

Matsumoto, J. & Masada, Y. 2013, ApJ, 772, 167

McKinney, J. C. 2006, MNRAS, 368, 1561

McMullin, J. P., Waters, B., Schiebel, D., Young, W., & Golap, K. 2007, in Astronomical Society of the Pacific Conference Series, Vol. 376, Astronomical Data Analysis Software and Systems XVI, ed. R. A. Shaw, F. Hill, & D. J. Bell, 127

Meier, D. L. 2012, Black hole astrophysics: the engine paradigm, Springer-Praxis books in astronomy and planetary sciences (Heidelberg [Germany] ; New York : Chichester, UK: Springer ; Published in association with Praxis Pub), oCLC: ocn751138743

Meier, D. L., Koide, S., & Uchida, Y. 2001, Science, 291, 84

Michell, J. 1784, Philosophical Transactions of the Royal Society of London Series I, 74, 35

Mizuno, Y., Gómez, J. L., Nishikawa, K.-I., et al. 2015, ApJ, 809, 38

Mizuno, Y., Hardee, P. E., & Nishikawa, K.-I. 2007, ApJ, 662, 835

Mizuno, Y., Hardee, P. E., & Nishikawa, K.-I. 2011, ApJ, 734, 19

Mizuno, Y., Lyubarsky, Y., Nishikawa, K.-I., & Hardee, P. E. 2012, ApJ, 757, 16

Mohana, K., Gupta, A. C., Marscher, A. P., et al. 2023, Monthly Notices of the Royal Astronomical Society, 527, 6970

Molina, S. N., Agudo, I., Gómez, J. L., et al. 2014, A&A, 566, A26

Moriyama, K., Akiyama, K., Cho, I., et al. 2022, SMILI v0.2.0

Müller, H. 2024, A&A, 689, A299

Müller, H. & Lobanov, A. P. 2022, A&A, 666, A137

Müller, H. & Lobanov, A. P. 2023, A&A, 673, A151

Müller, H., Massa, P., Mus, A., Kim, J.-S., & Perracchione, E. 2024, A&A, 684, A47

Müller, H., Mus, A., & Lobanov, A. 2023, A&A, 675, A60

Mus, A. 2023, PhD thesis, Universitat de València

Mus, A., Martí-Vidal, I., Wielgus, M., & Stroud, G. 2022, A&A, 666, A39

Mus, A. & Martí-Vidal, I. 2024, Monthly Notices of the Royal Astronomical Society, stae234

Mus, A., Müller, H., & Lobanov, A. 2024a, A&A, 688, A100

Mus, A., Müller, H., Martí-Vidal, I., & Lobanov, A. 2024b, A&A, 684, A55

Mus, A., Toscano, T., Müller, H., et al. 2025, arXiv e-prints, arXiv:2504.16257

Myserlis, I., Angelakis, E., Kraus, A., et al. 2018, A&A, 609, A68

Müller, H. 2025, in preparation

Narayan, R., Igumenshchev, I. V., & Abramowicz, M. A. 2003, Publications of the Astronomical Society of Japan, 55, L69

Narayan, R. & Nityananda, R. 1986, Annual Review of Astronomy and Astrophysics, 24, 127

Narayan, R. & Nityananda, R. 1986, ARA&A, 24, 127

Oei, M. S. S. L., Hardcastle, M. J., Timmerman, R., et al. 2024, Nature, 625, 457

Offringa, A. R. & Smirnov, O. 2017, MNRAS, 471, 301

Okino, H., Akiyama, K., Asada, K., et al. 2022, ApJ, 940, 65

Okino, H., Akiyama, K., Asada, K., et al. 2022, ApJ, 940, 65

Oppenheimer, J. R. & Snyder, H. 1939, Phys. Rev., 56, 455

Pacholczyk, A. G. 1970, Radio astrophysics: nonthermal processes in galactic and extragalactic sources, A Series of books in astronomy and astrophysics (San Francisco: W. H. Freeman)

Paliya, V. S. 2015, The Astrophysical Journal Letters, 808, L48

Paliya, V. S., Diltz, C., Böttcher, M., Stalin, C. S., & Buckley, D. 2016, ApJ, 817, 61

Palumbo, D. C. M. & Wong, G. N. 2022, ApJ, 929, 49

Pardalos, P. M., Žilinskas, A., & Žilinskas, J. 2017, Non-Convex Multi-Objective Optimization (Cham: Springer)

Pasetto, A., Carrasco-González, C., Gómez, J. L., et al. 2021, ApJ, 923, L5

Penrose, R. 1965, Phys. Rev. Lett., 14, 57

Perley, R. A. & Meisenheimer, K. 2017, A&A, 601, A35

Perucho, M., Kovalev, Y. Y., Lobanov, A. P., Hardee, P. E., & Agudo, I. 2012, ApJ, 749, 55

Perucho, M., Martí, J. M., Laing, R. A., & Hardee, P. E. 2014, MNRAS, 441, 1488

Petrov, L. 2011, AJ, 142, 1

Pilipenko, S. V., Kovalev, Y. Y., Andrianov, A. S., et al. 2017, Monthly Notices of the Royal Astronomical Society, 474, 3523

Popkov, A. V., Kovalev, Y. Y., Petrov, L. Y., & Kovalev, Y. A. 2021, AJ, 161, 88

Prince, R. 2020, ApJ, 890, 164

Pushkarev & Kovalev. 2012, A&A, 544, A34

Pushkarev, A. B., Aller, H. D., Aller, M. F., et al. 2023, Monthly Notices of the Royal Astronomical Society, 520, 6053

Rau, U. & Cornwell, T. J. 2011, A&A, 532, A71

Readhead, A. C. S. 1994, ApJ, 426, 51

Rees, M. J. 1966, Nature, 211, 468

Reid, M. J. & Brunthaler, A. 2020, ApJ, 892, 39

Röder, J., Wielgus, M., Lobanov, A. P., et al. 2025, A&A, 695, A233

Rybicki, G. B. & Lightman, A. P. 1979, Radiative processes in astrophysics (John Wiley & Sons)

Ryle, M. 1952, Proceedings of the Royal Society of London Series A, 211, 351

Ryle, M. & Hewish, A. 1960, Monthly Notices of the Royal Astronomical Society, 120, 220

Ryle, M. & Vonberg, D. D. 1946, Nature, 158, 339

Sandage, A. 1965, ApJ, 141, 1560

Savolainen, Giovannini, G., Kovalev, Y. Y., et al. 2023, A&A, 676, A114

Savolainen, T., Wiik, K., Valtaoja, E., & Tornikoski, M. 2006, A&A, 446, 71

Savolainen, T., Wiik, K., Valtaoja, E., & Tornikoski, M. 2008, in Astronomical Society of the Pacific Conference Series, Vol. 386, Extragalactic Jets: Theory and Observation from Radio to Gamma Ray, ed. T. A. Rector & D. S. De Young, 451

Schmidt, M. 1963, Nature, 197, 1040

Schmidt, M. 1963, Nature, 197, 1040

Schmidt, M. & Green, R. F. 1983, ApJ, 269, 352

Schwab, F. R. & Cotton, W. D. 1983, AJ, 88, 688

Schwarzschild, K. 1916, Sitzungsberichte der Königlich Preußischen Akademie der Wissenschaften (Berlin, 189

Schödel, R., Ott, T., Genzel, R., et al. 2002, Nature, 419, 694

Seyfert, C. K. 1943, ApJ, 97, 28

Shah, Z., Jithesh, V., Sahayanathan, S., Misra, R., & Iqbal, N. 2019, MNRAS, 484, 3168

Shepherd, M. 2011, Difmap: Synthesis Imaging of Visibility Data

Shepherd, M. C. 1997, in Astronomical Society of the Pacific Conference Series, Vol. 125, Astronomical Data Analysis Software and Systems VI, ed. G. Hunt & H. Payne, 77

Shepherd, M. C., Pearson, T. J., & Taylor, G. B. 1994, in Bulletin of the American Astronomical Society, Vol. 26, 987–989

Shepherd, M. C., Pearson, T. J., & Taylor, G. B. 1995, Bulletin of the Astronomical Society, 27, 903

Shukla, A. & Mannheim, K. 2020, Nature Communications, 11, 4176

Singal, A. K. 2009, The Astrophysical Journal, 703, L109

Slysh, V. I. 1992, ApJ, 391, 453

Strittmatter, P. A., Serkowski, K., Carswell, R., et al. 1972, ApJ, 175, L7

Tchekhovskoy, A., Narayan, R., & McKinney, J. C. 2011, Monthly Notices of the Royal Astronomical Society: Letters, 418, L79

Teräsranta, H., Tornikoski, M., Karlamaa, K., et al. 1992, in Proceedings of The Variability of Blazars, Turku, 6-10 January 1991 (United Kingdom: Cambridge University Press), 159–166

Thompson, A. R., Moran, J. M., & Swenson, Jr., G. W. 2017, Interferometry and Synthesis in Radio Astronomy, 3rd Edition (Springer)

Tiede, P. 2022, The Journal of Open Source Software, 7, 4457

Tolamatti, A., Ghosal, B., Singh, K., et al. 2022, Astroparticle Physics, 139, 102687

Toscano, Teresa, Molina, Sol N., Gómez, José L., et al. 2025, A&A, 698, A210

Urry, C. M. & Padovani, P. 1995, Publications of the Astronomical Society of the Pacific, 107, 803

Van Cittert, P. H. 1934, Physica, 1, 201

Vega-García, L., Lobanov, A. P., Perucho, M., et al. 2020, A&A, 641, A40

Vlahakis, N. & Königl, A. 2004, ApJ, 605, 656

Walker, R. C., Dhawan, V., Romney, J. D., Kellermann, K. I., & Vermeulen, R. C. 2000, ApJ, 530, 233

Wang, G., Fan, J., Xiao, H., & Cai, J. 2022, PASP, 134, 104101

Wardle, J. 2018, Galaxies, 6

Weaver, Z. R., Jorstad, S. G., Marscher, A. P., et al. 2022, The Astrophysical Journal Supplement Series, 260, 12

Whitney, A. R., Shapiro, I. I., Rogers, A. E. E., et al. 1971, Science, 173, 225

Wielgus, M., Akiyama, K., Blackburn, L., et al. 2020, ApJ, 901, 67

Wielgus, M., Marchili, N., Martí-Vidal, I., et al. 2022, ApJ, 930, L19

Wielgus, M., Marchili, N., Martí-Vidal, I., et al. 2022, ApJ, 930, L19

Zamaninasab, M., Savolainen, T., Clausen-Brown, E., et al. 2013, MNRAS, 436, 3341

Zavala, R. T. & Taylor, G. B. 2001, ApJ, 550, L147

Zavala, R. T. & Taylor, G. B. 2005, ApJ, 626, L73

Zernike, F. 1938, Physica, 5, 785

Zhang, Q. & Li, H. 2007, IEEE Transactions on Evolutionary Computation, 11, 712

Zhao, G.-Y., Gómez, J. L., Fuentes, A., et al. 2022, ApJ, 932, 72